

DIGITAL ACCESS TO SCHOLARSHIP AT HARVARD
DASH.HARVARD.EDU

HARVARD LIBRARY


Probing dynamics of a two-dimensional dipolar spin ensemble

Citation

Rezai, Kristine Farielle. 2022. Probing dynamics of a two-dimensional dipolar spin ensemble. Doctoral dissertation, Harvard University Graduate School of Arts and Sciences.

Link

https://nrs.harvard.edu/URN-3:HUL.INSTREPOS:37372278

Terms of use

This article was downloaded from Harvard University's DASH repository, and is made available under the terms and conditions applicable to Other Posted Material (LAA), as set forth at

https://harvardwiki.atlassian.net/wiki/external/NGY5NDE4ZjgzNTc5NDQzMGIzZWZhMGFlOWI2M2EwYTg

Accessibility

https://accessibility.huit.harvard.edu/digital-accessibility-policy

Share Your Story

The Harvard community has made this article openly available.
Please share how this access benefits you. Submit a story

HARVARD UNIVERSITY
Graduate School of Arts and Sciences



DISSERTATION ACCEPTANCE CERTIFICATE

The undersigned, appointed by the

Department of Physics

have examined a dissertation entitled

Probing dynamics of a two-dimensional dipolar spin ensemble

presented by Kristine Farielle Rezai

candidate for the degree of Doctor of Philosophy and hereby certify that it is worthy of acceptance.

Signature _____

Typed name: Professor Mikhail Lukin, Chair

Signature _____

Typed name: Professor Alexander Sushkov (Boston Univ.), Co-Chair

Signature _____

Typed name: Professor Hongkun Park

Date: May 5, 2022

Probing dynamics of a two-dimensional dipolar spin ensemble

A DISSERTATION PRESENTED
BY
KRISTINE FARIELLE REZAI
TO
THE DEPARTMENT OF PHYSICS

IN PARTIAL FULFILLMENT OF THE REQUIREMENTS
FOR THE DEGREE OF
DOCTOR OF PHILOSOPHY
IN THE SUBJECT OF
PHYSICS

HARVARD UNIVERSITY
CAMBRIDGE, MASSACHUSETTS
MAY 2022

©2022 – Kristine Farielle Rezai
all rights reserved.

Dissertation Advisor: Professor Alex Sushkov and Mikhail Lukin Kristine Farielle Rezai

Probing dynamics of a two-dimensional dipolar spin ensemble

Abstract

One of the central challenges of modern statistical physics is understanding the thermalization dynamics of quantum many-body systems at the microscopic level. In this thesis, we describe an experimental study of individual spin dynamics in a two-dimensional ensemble of electron spins on the surface of a diamond crystal. A near-surface NV center is used as a nanoscale magnetic sensor to probe individual spin correlation dynamics in a dipolar interacting spin ensemble. For each spin, the rate of relaxation of spin projection along the bias magnetic field is consistently much slower than the dipolar interaction strengths with its nearest neighbors and is strongly correlated with the timescale of the local magnetic field fluctuation. We present a quantitative model based on dynamic resonance counting arguments that explains these observations. Furthermore, we use resonant spin-lock driving to control the effective strength of the local magnetic fields and demonstrate the role of dynamical disorder in different regimes. In the regime of suppressed extrinsic disorder, we use dynamic mean field methods to explain our experimental observations. The work presented in this thesis paves the way towards a microscopic study of quantum thermalization in two-dimensional strongly interacting disordered spin ensembles.

Contents

Title Page i

Copyright ii

Abstract iii

Table of Contents iv

List of Figures vii

Acknowledgments and Dedication xvi

1 Introduction 1

1.1 Motivation 1

1.2 Overview of Thesis 3

1.3 The Nitrogen-Vacancy Center in Diamond 4

1.4 Surface Spins in Diamond 6

2 Characterization of the Local Magnetic Environment of the Surface Spins 14
2.1 Decoherence due to the Nuclear Spin Bath . . . 17
2.2 Extraction of Surface Spin On-site Disorder Strength W . . . 22
2.3 Extraction of Proton Nuclear Spin Signal Correlation Time τ . . . 22
2.4 Extracting the Surface Spin Density . . . 23

3 Surface Spin Relaxation 24
3.1 Resonance Counting Theory . . . 26
3.2 S_z Autocorrelation Scaling . . . 32
3.3 Spin-lock Driving Measurements ($T_{1\rho}$) . . . 32

4 Dynamic Mean Field Models 39
4.1 Dynamic Mean Field Models in the Singly Rotating Frame . . . 40
4.2 Doubly Rotated Mean Field Dipolar Hamiltonian . . . 45

5 Surface Spin Polarization 49
5.1 Dynamics of a Polarized Central Surface Spin . . . 52
5.2 Surface Spin Stability . . . 54

6 Conclusion and Outlook 56

Appendix A Materials and Setup 59
A.1 Diamond Sample . . . 59
A.2 Optical Setup . . . 60
A.3 Radiofrequency Setup . . . 60

Appendix B Nuclear Spin Bath Noise Spectrum 62

B.1 Wiener-Khinchin Theorem 63

B.2 Calculate $\langle B^2_{\parallel,rms} \rangle$ from Longitudinal Component of the Nuclear Magnetic Moment 65

B.3 Calculate $\langle B^2_{\perp,rms} \rangle$ from Transverse Component of the Nuclear Magnetic Moment 68

B.4 Noise Spectrum Equation 72

Appendix C Simulation Procedure 74

C.1 Effects of Finite Pulse Duration 79

Appendix D Decoherence due to the Nuclear Spin Bath 81

D.1 Ramsey 83

D.2 Echo 85

D.3 XY-4 87

D.4 XY-8 89

D.5 MREV-8 91

D.6 Final Fit functions 93

References 100

Listing of figures

1.1 The nitrogen vacancy center in diamond. Left: a single nitrogen vacancy center in diamond with an inset showing the defect in the diamond lattice. Right: the simplified NV center electronic level structure 4

1.2 NV XY-64 measurement, with total sequence time centered around expected proton peak, performed in an external magnetic field of 735 G. Fit (blue curve) to Eq. 1 in [43], extracting a proton B_{rms} corresponding to an NV center depth of $d_{NV} = (2.92 \pm 0.24)$ nm. 5

1.3 Introduction to the NV center - surface spin system. (a) The experimental platform consists of a single, shallow NV center strongly coupled to one surface electron spin S_j. Other electron spins and proton nuclear spins reside on the surface of the diamond. An external magnet splits the electron and nuclear spin states and allows independent manipulation of NV center and surface spins at their corresponding magnetic resonance frequencies. Inset: NV center and surface spin level structure. NV center transition is addressed at angular frequency ω_{NV} while surface spin transition is addressed at ω_S. (b) Experimental approach to using the NV center to probe the surface spin system. 7

1.4 NV center Hahn echo (blue) and double electron-electron resonance (DEER) (red) measurements. The oscillations present in the DEER data indicate that the magnetic dipole interactions of this NV center with the surface spin ensemble are dominated by a central surface spin with the coupling strength $k_{max} = (4.90 \pm 0.57)\,\mu s^{-1}$ (red line fit). Inset: the DEER pulse sequence. 8

1.5 (a) DEER data taken at 8 different magnetic field angles (external magnetic field ≈ 45 G). Bottom right plot is T_2 data (external magnetic field ≈ 1343 G). Blue line corresponds to the best global fit for a system of 3 surface spins. (b) Extracted probability map of the 3 surface spins, with each color corresponding to the inverse of the reduced χ^2 value for a surface spin in that position, while the other 2 surface spins have best-fit positions. 11

1.6 (a) The correlation spectroscopy pulse sequence. In our experiments the NV center interpulse spacing is set such that the NV center is primarily sensitive to the central surface spin S_z autocorrelation. Manipulating the surface spins during the gray shaded region allows us to measure different central surface spin correlation functions. (b) Quantum logic gate representation of the correlation spectroscopy pulse sequence. The two CNOT gates are applied, such that the final state of the NV center is contingent on whether the z-projection of the central surface spin changed during the time between the gates. 12

2.1 Characterization of the local magnetic environment of a central surface spin. Solid lines are fits using the model in eqs. (3.1,3.2). (a) Surface spin detuned Ramsey measurement of $\langle S_j^x(t)S_j^x(0)\rangle$ transverse central spin autocorrelation. The Ramsey decay time is $T_2^* = (0.32 \pm 0.02)\,\mu$s. Solid lines are fits using the model in eqs. (2.1,2.2). The oscillations in the Ramsey data are due to the 9.2 MHz detuning from the surface spin Larmor frequency. (b) Surface spin Hahn echo measurements of $\langle S_j^x(t)S_j^x(0)\rangle$ transverse central spin autocorrelation. The Hahn echo decay time is $T_2 = (1.41 \pm 0.11)$ μs. (c) Surface spin XY-4 measurement, with oscillations due to proton nuclear spin precession. (d) Surface spin MREV-8 measurement performed within a spin echo with oscillations due to proton nuclear spin precession. 15

2.2 Nuclear spin bath noise power spectrum V(ω), with peaks at zero frequency and proton Larmor frequency ω_L. 17

2.3 Comparison of surface spin echo, XY-4, and MREV-8 measurements, showing the extension of coherence time with MREV-8 and the decoupling of the central spin from homonuclear dipolar interactions with other surface spins. 20

2.4 Spin echo decay results for 1 central spin plus 6 bath spins, measuring the central spin autocorrelation for different bath spin positions. The extracted decay rates versus maximum interaction strength was linearly fit to find $(1/T_2) = bJ_{max}$ where $b = (0.501 \pm 0.003)$. The y error bars correspond to the uncertainty in the fit to each simulation result. 21

2.5 (a) Simulation results with averaged experimental data (white dots). (b) χ^2 vs average separation, where an average separation between surface spins of 8.4 ± 1.3 nm is extracted. 23

3.1 Measurement of central surface spin $\langle S_j^z(t) S_j^z(0) \rangle$ autocorrelation. (a) S^z autocorrelation measurement pulse sequence where the time between the initial and final pulse blocks is swept. A π pulse is applied to the surface spins during the free precession interval half of the time. The time between NV pulses is tuned to the dipolar interaction timescale between the NV center and the central surface spin, as calibrated using DEER and a correlation spectroscopy NV tau sweep. (b) S^z autocorrelation measurement for the central surface spin system characterized in chapter 2, with $J_1 = (0.71 \pm 0.05)\,\mu s^{-1}$, $W = (4.40 \pm 0.38)\,\mu s^{-1}$, and $\tau = (14.6 \pm 4.2)\,\mu s$. Blue line fit to $\exp\left(-(t/T_z)^{2/3}\right)$ (c) The full characterization of relaxation timescales for one of the central surface spin systems, including the Ramsey, XY-4, MREV-8, and S^z autocorrelation measurements. 25

3.2 A schematic of the spin hopping process in our model, showing a central surface spin S_j and another surface spin S_i. Each spin state is shifted by time-dependent on-site detuning δ (blue line), due to the local dynamical disorder created by nuclear spin bath noise and Ising dipolar interaction terms. The spins can flip-flop if their detunings differ by less than the strength J of the dipolar interaction between them (grey band). 27

3.3 Plots of (a) $P_1(t)$ and (b) $P_2(t)$ with $r_0 = 2$ nm, $\beta = 1$, $\tau = 15\ \mu$s, $W = 3.77\ \mu\text{s}^{-1}$, and $J_0 = 326.7\ \text{nm}^3/\mu\text{s}$. $P_2(t)$ has a stronger dependence on time than $P_1(t)$ for times t> τ. 30

3.4 Measurements of central surface spin $\langle S_j^x(t)S_j^x(0)\rangle$ autocorrelation. Each color represents a different central surface spin system. (a) S^x autocorrelation measurements for 7 different central surface spin systems. Each measurement is fit by a stretched exponential, from which we extract the relaxation time T_z. (b) S_z autocorrelation measurements with the decay time re-scaled by the product $\tau_e W_e$ of the effective disorder correlation time and disorder width, independently measured for each surface spin system. We observe a collapse of the 7 data sets to a universal stretched-exponential decay curve, in agreement with our dynamical disorder model. 31

3.5 S_z autocorrelation decay time plotted as a function of different system parameters including (a) $\tau_e W_e$, (b) W, (c) τ, and (d) T_2. The colors correspond to the data sets represented in fig. 3.4. The black line in (a) is a linear fit. 32

3.6 Evolution of central surface spin under spin-lock driving. Measurements of $\langle S_j^y(t)S_j^y(0)\rangle$ autocorrelation under spin-lock driving for different drive strengths. Stronger driving results in better decoupling from the nuclear spin bath magnetic noise and longer $T_{1\rho}$ relaxation time. For drive strength $\Omega \gtrsim 50\,\mu\text{s}^{-1}$, relaxation rate is independent of Ω. Lines show stretched exponential decay fits. Inset: radio frequency NV and surface spin pulses; green laser polarization and readout pulses applied before and after this sequence of RF pulses. 33

3.7 Spin-lock driving relaxation rate as a function of drive strength for 4 different surface spin systems, along with the corresponding decay rates for Hahn echo ($1/T_2$) and S^z autocorrelation ($1/T_z$) experiments, shown by the gray bands. The point at $\Omega = 0$ corresponds to the decay of the Ramsey coherence ($1/T_2{}^*$). The measurements performed with drive strength below $50\,\mu s^{-1}$ are consistent with direct relaxation due to the nuclear spin bath noise with spectrum $V(\omega)$ (black line). Relaxation rates for drive strengths $\Omega \gtrsim 50\,\mu s^{-1}$ are independent of Ω and consistently much slower than the dipolar interaction scale $1/T_2$. 36

3.8 Comparison between different autocorrelation decay timescales for 4 different surface spin systems. Red circles, labeled $T_{1\rho}/2$, show the decay time under spin-lock at strong driving. As the dynamical on-site disorder strength W increases, the T_z autocorrelation decay time increases compared with the autocorrelation decay at strong driving with suppressed disorder ($T_{1\rho}/2$). Both of these decays are much slower (by a factor of ≈ 30) than the dipolar interaction scale, given by T_2. 37

4.1 Dynamic mean field results in the doubly rotating frame with 4 directly simulated spins. (a) Plot of relaxation timescale T_2 of transverse spin autocorrelation versus the maximum dipolar interaction strength of the central spin with another spin J_{max}. A linear relationship between J_{max} and $1/T_2$ is extracted. (b) Plot of longitudinal relaxation timescale $T_{1\rho}$ versus maximum dipolar interaction strength J_{max} when decay is fit to a stretched exponential with a floating power as well as a power of $2/3$, as predicted from the resonance counting model. 47

4.2 Dynamic mean field theory results compared with experimental data. (a) Surface spin echo measurement with dynamic mean field model result (black dashed line). (b) Surface spin $T_{1\rho}$ measurement with dynamic mean field model result (black line). . . 47

5.1 (a) RF drives of a Hartmann-Hahn spin polarization pulse sequence. A green laser pulse is applied at the beginning of the sequence to initialize the NV center spin state. (b) Flip-flop interactions between the NV spin and a surface spin in the doubly rotated frame where Ω_y^{NV} and Ω_y^S are the drive Rabi strengths applied to the NV center and surface spins, respectively. The splitting between the eigenstates is given by the strength of the drive in the doubly rotating frame. 50

5.2 (a) Hartmann-Hahn polarization sequence, where final state of the NV center is read out by measuring fluorescence after the polarization transfer. During this sequence, the RF power delivered to the surface spins is swept. (b) Probability of an NV spin flip, where a value of 0.5 would correspond to maximal polarization transfer between the NV center and the central surface spin. 50

5.3 (a) Hartmann-Hahn spin polarization and readout pulse sequence, where the surface spin drive power Ω_y^S is swept. (b) Central surface spin polarization as a function of detuning from NV Rabi frequency, normalized between 0 (unpolarized) and 1. A value of 1 corresponds to the maximum polarization expected from the maximal NV depolarization calibrated above. 51

5.4 (a) Hartmann-Hahn spin polarization and readout pulse sequence where the drive duration is swept. (b) The time to maximum polarization transfer (1 μs) is consistent with the interaction strength between the strongest coupled surface spin and the NV center. (c) Hartmann-Hahn spin polarization and readout pulse sequence with variable time between readout pulses. (d) Time between readout pulses corresponding to maximal polarization transfer consistent with the interaction strength between strongest coupled surface spin and the NV center. 52

5.5 Surface spin detuned Ramsey measurement with the NV center in m_s = 0 or m_s = -1. The oscillations are due to detuned surface spin pulses, and we observe a difference in oscillation frequency between the red and blue curves consistent with the dipolar interaction between the NV center and the central surface spin. Inset: pulse sequence with Hartmann-Hahn polarization transfer followed by a surface spin Ramsey sequence and then NV center state readout pulses. 53

5.6 Surface spin T_z measurement after polarization with the NV center in either m_s = 0 or m_s = -1. Measurement results indicate no difference in relaxation rate between the two cases, to within measurement uncertainty. Inset: pulse sequence with Hartmann-Hahn spin polarization following by a swept delay time before NV pulses read out the final surface spin state. 54

5.7 Surviving polarization of the central surface spin after green laser light illumination. (a) HH polarization transfer sequence and readout of final NV center state contingent on polarization of central surface spin while green NV repolarization laser pulse duration is swept. (b) Measurement result, normalized by the contrast of the S_z autocorrelation measurement of equivalent initial time delay. 55

C.1 Simulation results for finite pulses versus infinitely fast pulses. For infinitely fast pulses, the x-axis is given by the total free precession time and for finite pulses, the x-axis corresponds to the free precession time between pulses plus the finite duration of the pulses. 79

D.1 Numeric verification of expected Ramsey decay. (a) Expected decay from $V_1(\omega)$ with t = 8 μs. Inset: Ramsey pulse sequence. (b) Expected decay from $V_2(\omega)$ 85

D.2 Numeric verification of expected Hahn echo decay. (a) Expected decay from $V_1(\omega)$ with t = 8 μs. Inset: Hahn echo pulse sequence. (b) Expected decay from $V_2(\omega)$. 87

D.3 Numeric verification of expected XY-4 decay. (a) Expected decay from $V_1(\omega)$ with t = 8 μs. (b) Expected decay from $V_2(\omega)$. Inset: XY-4 pulse sequence. 89

D.4 Numeric verification of expected XY-8 decay. (a) Expected decay from $V_1(\omega)$ with t = 8 μs. (b) Expected decay from $V_2(\omega)$. Inset: XY-8 pulse sequence. 91

D.5 MREV-8 pulse sequence, applied during the free precession intervals of a spin echo sequence. 91

D.6 Numeric verification of expected MREV-8 decay. (a) Expected decay from $V_1(\omega)$ with t = 8 μs. (b) Expected decay from $V_2(\omega)$. 93

Acknowledgments

Graduate school has been an influential part of my life, and I owe it in part to the amazing people I had the pleasure of working with and who have supported me from afar. I first want to acknowledge and thank my advisor Alex Sushkov for supporting me every step of the way through my PhD and for teaching me what it means to be a good scientist. I appreciate all of the time you have devoted to helping me reach my goals, and your passion and commitment to doing great science is inspiring. I also want to thank Misha Lukin for his advice and encouragement over the past many years. Misha continuously amazes me with his invaluable scientific insight. I also want to thank Hongkun Park for his continual support and advice over the course of my graduate school career. Starting a new lab from scratch presents its own unique set of challenges and rewards, and I am so thankful to have had the opportunity to be one of the first students in a group along my friend and colleague Deniz Aybas.

Over the course of my PhD, I had the opportunity to work with many talented and inspirational people. First, I want to thank all of the current and former members of the Sushkov group including Deniz Aybas, Eric Boyers, Jack Stropko, Sasha Gramolin, Janos Adam, Alexander Wilzewski, Andrew Winter, Glenn Randall, Annalies Kleyheeg, Hannah Mekbib, and Adam Pearson. I also

want to thank all current and former members of the Lukin group. Elana Urbach, Emma Rosenfeld, Soonwon Choi, Bo Dwyer, Tamara Sumarac, and Harry Zhou in particular have advised me through various stages of my work. I have also had the pleasure of working with faculty outside of Harvard including Gotz Uhrig and Soonwon Choi as well as Timo Graesser, a graduate student at TU Dortmund.

My time at Harvard would not have been the same without the friends I made along the way. I first want to thank my roommates and friends Laurel Anderson, Sasha Brownsberger, Cole Meisenhelder, and Trisha Madhavan. I will miss our Dungeons and Dragons campaign and cats Holly and Campbell as we all move on to the next stage of our lives. I also want to thank my friends Monica Kang, Taylor Patti, Sona Najafi, David Levonian, Nicholas Mondrik, and Aditya Venkatramani for all of the great times we had. I also want to thank my Somerville bike friends as well as my childhood friends for your continued support. Lastly, I'd like to thank my parents, Karen and Farhad, and my sister Alex for always being there for me.

To my friends, family, and Holly and Campbell

1

Introduction

1.1 Motivation

Understanding and controlling dynamics of many-body quantum systems isolated from their environment enables the development of novel materials and technologies for quantum devices for sensing, computation, communication, and modeling[40,32]. Such systems have been realized in a variety of platforms: ultracold atoms[6], trapped ions[5], superconducting devices[29,4], and solid-state

qubits [15,49,52,2,63]. Access to single-qubit dynamics is especially important in heterogeneous systems [50,58], where the local environment plays a vital role, and ensemble averaging can conceal features of dynamical evolution. The interplay between the local qubit environment, interactions, and system dimensionality has been the subject of extensive theoretical and experimental investigations [21,9,64]. These systems have served as a basis for experimental observations of nonequilibrium quantum dynamics in strongly interacting systems such as the propagation of quantum correlations [25,44,42], nonequilibrium phases of matter [65,10,28,45,17], and relaxation or localization effects [2,63,54,11,30,51,27].

Quantum thermalization connects statistical physics with unitary quantum mechanics. Recent technological developments in quantum information science have revealed a variety of novel phenomena such as the role of entanglement in thermalization [27,35,45], the localization in the absence of strong disorder [37], non-equilibrium phases [65,10,28,45,17,31], and quantum many-body scarring [62,7,26]. Despite this progress, one of the open questions in this field is the nature of microscopic relaxation dynamics in presence of dynamical disorder and long-range interactions. The majority of existing studies focus on ensemble measurements in systems dominated by static disorder [2,63,54,11,30,51]. However, ensemble averaging can conceal important features of microscopic dynamical evolution [19,14], and in many noisy real-world quantum systems disorder is dynamic, exhibiting non-trivial time-dependence. Another important factor is system dimensionality and its interplay with the distance scaling of interactions. The long-range $1/r^3$ dipolar spin interaction implies that a two-dimensional system should be localized according to the single-particle Anderson model [3], but delocalized according to the many-body interacting treatment [9,64,20,41,21]. In addition to fundamental interest, understanding the dynamics of two-dimensional systems may lead to quantum sensing applications, since they can be positioned in close proximity to a sensing target [57,12].

1.2 Overview of Thesis

In this thesis, we focus on the experimental platform consisting of a single shallow nitrogen-vacancy (NV) center qubit coupled to a system of paramagnetic spins on the diamond surface. In the remainder of this chapter, we review the necessary background on NV centers in diamond before discussing the system of electron spins on the diamond surface. We discuss the technique of correlation spectroscopy where the NV center is used to probe the autocorrelation of the central surface spin state, which is the main experimental technique we use in chapters 2 and 3.

In chapter 2, we use the framework of the correlation spectroscopy pulse sequence to probe the local magnetic noise environment of the central surface spin. We characterize its strongest dipolar interaction with nearby surface spins as well as measure the correlation time τ and width W of the local nuclear spin bath noise.

In chapter 3, we measure the longitudinal relaxation of the central surface spin and provide a dynamic resonance counting theory to account for our experimental observations. We also drive the system and show that at weak drives, the resulting relaxation is primarily due to the nuclear spin noise. However, at strong drive, the surface spins are decoupled from extrinsic nuclear spin disorder and instead exhibit slower dynamics than expected given the strongest dipolar interaction strength, which we attest to the intrinsic disorder from the random positions of nearby surface spins.

In chapter 4, we explore the use of dynamic mean field methods to predict single spin longitudinal and transverse autocorrelation relaxations. By using dynamic mean field models plus a few nearby spins, we are able to model the slow timescale of the strong drive spin-lock driving measurements.

In chapter 5, we discuss our ability to prepare the initial state of the strongest coupled surface spin by polarizing it using the NV center. We can then observe how resulting central surface spin dynamics are dependent on the state of the NV center and conclude by demonstrating the stability

of the central spin under green laser illumination.

We conclude our work in chapter 6 and discuss outlooks for future research directions. The Appendices contain additional information and simulation results.

1.3 The Nitrogen-Vacancy Center in Diamond

We begin with a description of the nitrogen-vacancy center, a point defect in the diamond lattice that consists of a substitutional nitrogen atom and an adjacent vacancy, fig. 1.1 (left, inset). There are 4 possible orientations of this defect along the four crystallographic directions of the lattice. While the NV center defect is naturally occurring in diamond, for the samples that we consider, NV center formation is done by nitrogen ion implantation followed by higher temperature annealing.

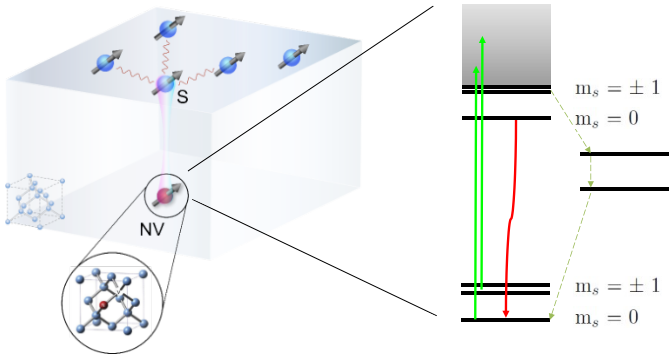


Figure 1.1: The nitrogen vacancy center in diamond. Left: a single nitrogen vacancy center in diamond with an inset showing the defect in the diamond lattice. Right: the simplified NV center electronic level structure

While the NV center can exist in several charge states, we consider the negatively charged defect and show its electronic level structure in fig. 1.1 (right). The ground state is a spin triplet with a zero-field splitting of approximately 2.87 GHz between the $m_s = 0$ and $m_s = \pm 1$ magnetic sublevels. When an external magnetic field is applied, it splits the level degeneracy of the $m_s = \pm 1$ magnetic sublevels such that transitions between $m_s = 0$ and the $m_s = \pm 1$ states can be independently addressed.

The NV center can be optically pumped in order to initialize it into the $m_s = 0$ ground state. From the $m_s = \pm 1$ excited state, there is a chance the excited electronic configuration can decay through a set of metastable singlet states into the $m_s = 0$ ground state. Thus, after a duration of optical pumping, the NV center begins in the $m_s = 0$ ground state. Also, the state of the NV center can be optically detected since population in the $m_s = 0$ excited state will decay back to the $m_s = 0$ emitting a red photon whereas population in the $m_s = \pm 1$ has a chance of decaying into the singlet states with no visible photon emission.

In order to extract the depth of the NV centers used in this study, we placed the diamond in protonated glycerol and performed XY radio frequency (RF) pulse sequences on the NV center to correlate the strength of the measured proton signal to the depth of the NV center. Following the treatment in [43], when performing an XY-64 pulse sequence on one NV center, an NV center depth of $d_{NV} = (2.92 \pm 0.24)$ nm was extracted. Depth measurements on other NV centers used in this study yielded similar results.

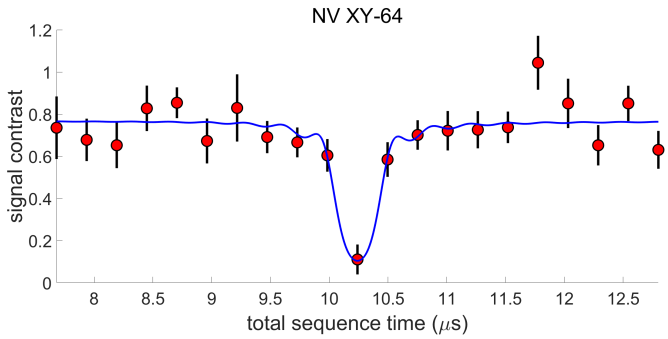


Figure 1.2: NV XY-64 measurement, with total sequence time centered around expected proton peak, performed in an external magnetic field of 735 G. Fit (blue curve) to Eq. 1 in [43], extracting a proton B_{rms} corresponding to an NV center depth of $d_{NV} = (2.92 \pm 0.24)$ nm.

1.4 Surface Spins in Diamond

1.4.1 Introduction

Our experimental platform is the ensemble of paramagnetic two-level systems on the surface of a diamond crystal, fig. 1.3 (a)[24,23,61]. These surface spins are associated with electron spin $S = 1/2$ impurities that are not optically active. Their exact nature is subject to ongoing investigation, but they are likely localized defect surface states [48,55]. Due to faster decoherence of shallow NV centers[47,46,39,38,8], these surface spins have been considered to be deleterious and significant effort has gone into treating and engineering diamond surfaces to minimize their density[18]. However, with proper quantum control, they can be turned into a useful resource. The surface spins can be coherently manipulated and measured, and can be used as the so-called quantum reporters that probe and report the local magnetic environment. For example, by addressing a single surface spin, it is possible to detect and localize proximal single proton nuclear spins on the diamond surface under ambient conditions[57]. Recent experimental studies have shown that after certain surface treatments, some of the surface spins may be mobile, likely changing their positions under green laser light illumination[16]. We have verified that in our experiments the central surface spin remains intact when subjected to green laser light illumination of up to 50 μs. In fact, the central spin position is stable for the experiments carried over the timescale of months. This is likely due to the combination of small photo-ionization cross-section and steric protection by chemical surface groups[16].

The dynamics of individual surface spins are measured by a single near-surface NV center, acting as a nanoscale sensor of magnetic fields created by the surface spins. NV centers are addressed using a confocal microscopy setup, combined with radio frequency (RF) spin drive fields that are delivered via a transmission line fabricated on a glass coverslip. The surface spin transitions can be addressed with RF pulses delivered in the same manner. The 2.87 GHz zero-field splitting of the NV center enables independent addressing of the NV spin and the surface spin transitions by using different

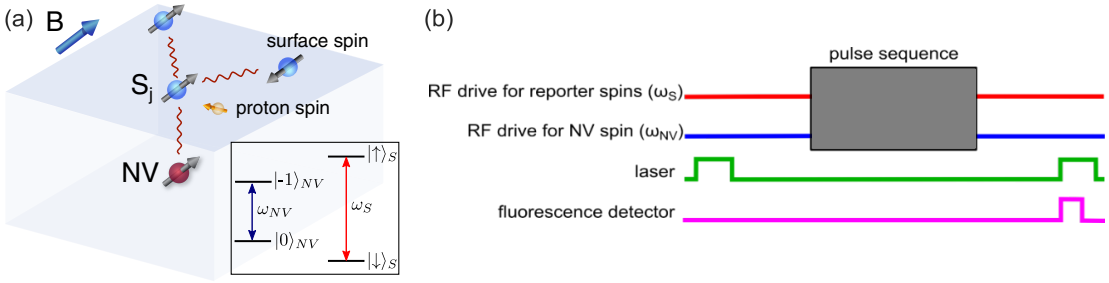


Figure 1.3: Introduction to the NV center - surface spin system. (a) The experimental platform consists of a single, shallow NV center strongly coupled to one surface electron spin S_j. Other electron spins and proton nuclear spins reside on the surface of the diamond. An external magnet splits the electron and nuclear spin states and allows independent manipulation of NV center and surface spins at their corresponding magnetic resonance frequencies. Inset: NV center and surface spin level structure. NV center transition is addressed at angular frequency ω_{NV} while surface spin transition is addressed at ω_S. (b) Experimental approach to using the NV center to probe the surface spin system.

resonant RF tones at a given bias magnetic field, aligned with the NV axis (z-axis), fig. 1.3(a), inset.

Our experiments take place at room temperature, with the bias magnetic field on the order of 1000 G. Therefore, the surface spin ensemble is effectively at infinite spin temperature. Our generalized experimental approach is shown in fig. 1.3(b). First, a green laser is applied to the NV center, initializing it into the $|m_s = 0\rangle$ state. Next, radio frequency spin drive fields are applied to independently drive the NV center and surface spin transitions. The final state of the NV center is read by applying green laser and measuring the fluorescence at the end of the measurement.

1.4.2 The Double Electron-Electron Resonance (DEER) Sequence

The magnetic dipole coupling between the NV center and the surface spin ensemble is characterized using a double electron-electron resonance (DEER) sequence, fig. 1.4. The NV center spin-echo decays on the time scale $T_2^{(nv)}$, but when a π-pulse flips the surface spins simultaneously with the NV spin, the NV spin echo collapses on a time scale that depends on the strength of the dipolar field created by the surface spins near the NV center. Because the magnetic dipole interaction is long-range, the NV center is, in general, coupled to multiple surface spins, with coupling strengths

dependent on locations of surface spins on the diamond surface. The oscillations present in the data at short time (fig. 1.4 red points) indicate that there is one "central" surface spin, whose dipolar coupling strength to the NV center k_{max} dominates over other surface spins.

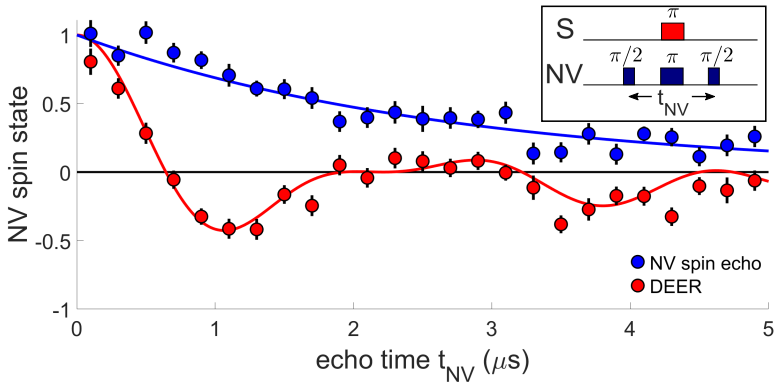


Figure 1.4: NV center Hahn echo (blue) and double electron-electron resonance (DEER) (red) measurements. The oscillations present in the DEER data indicate that the magnetic dipole interactions of this NV center with the surface spin ensemble are dominated by a central surface spin with the coupling strength k_{max} = (4.90 $\pm$ 0.57) μs^{-1} (red line fit). Inset: the DEER pulse sequence.

We can understand the results of the DEER sequence by beginning with the dipolar interaction Hamiltonian between the NV center $\mathbf{J}$ and surface spins $\mathbf{S_i}$, which is written as

$$H_{NV-ss} = \sum_i \frac{\hbar^2\gamma_e^2}{r_s^3}[\mathbf{J}\cdot\mathbf{S}_i - 3\frac{(\mathbf{J}\cdot\mathbf{r}_s)(\mathbf{S}_i\cdot\mathbf{r}_s)}{r_s^2}], \tag{1.1}$$

where $\mathbf{r}_s$ is the vector from the NV center to surface spin i. When we align the external magnetic field along the NV center axis, we can make a secular approximation and only consider terms that commute with S_i^z and J^z:

$$H_{NV-ss} = \sum_i \frac{\hbar^2\gamma_e^2}{r_s^3}(1-3\cos^2\theta_i)S_i^z J^z = \sum_i \hbar k_i S_i^z J^z \tag{1.2}$$

where θ_i is the angle the vector $\mathbf{r_s}$ makes with the external magnetic field, and the coupling strength is

$$k_i = \frac{\hbar\gamma_e^2}{r_s^3}(1 - 3\cos^2\theta_i). \tag{1.3}$$

The NV center $|m_s = 0\rangle$ state after performing the DEER sequence with total sequence time t_{NV} is

$$S_{DEER} = \frac{1}{2}[1 + \cos(\sum_i k_i S_i^x t_{NV})]. \tag{1.4}$$

After performing many averages with different initial surface spin projections, the final expected signal[57] is

$$S_{DEER} = \frac{1}{2}[1 + \prod_i \cos(k_i t_{NV}/2)]. \tag{1.5}$$

For systems of strong coupling between the NV center and one surface electron spin, oscillations at the largest coupling strength are present at short time. For the data presented in fig. 1.4, the NV spin-echo decays on a time scale $T_2^{NV} = (2.67 \pm 0.13)\,\mu$s and has a coupling strength of $k_{max} = (4.90 \pm 0.57)\,\mu\text{s}^{-1}$ to the strongest coupled surface spin.

The double electron-electron resonance (DEER) pulse sequence measures the strength of the dipolar interaction between the NV center and the surface spins, and this interaction strength is dependent on both the distance between the NV center and the surface spins as well as the angle between the longitudinal quantization axis of the NV center and the surface spins. For small external magnetic field strengths, by rotating the angle of the external magnetic field, we are able to extract probable positions for the closest surface spins to the NV center. The dipole-dipole interaction Hamiltonian between the NV center spin $\mathbf{J}$ and the surface electron spin $\mathbf{S}_i$ is:

$$H_{NV-ss} = \frac{\hbar^2\gamma_e^2}{r_s^3}[\mathbf{J}\cdot\mathbf{S}_i - 3\frac{(\mathbf{J}\cdot\mathbf{r}_s)(\mathbf{S}_i\cdot\mathbf{r}_s)}{r_s^2}] \tag{1.6}$$

where $\mathbf{r}_s$ is the vector from the NV center to the surface spin. The full Hamiltonian for the system of one NV center coupled to many surface spins is given by:

$$H = \hbar\Delta J_{z'}^2 + \hbar\gamma_e \mathbf{B}\cdot\mathbf{J} + \sum_i (\hbar\gamma_e \mathbf{B}\cdot\mathbf{S}_i + \frac{\hbar^2\gamma_e^2}{r_s^3}[\mathbf{J}\cdot\mathbf{S}_i - 3\frac{(\mathbf{J}\cdot\mathbf{r}_s)(\mathbf{S}_i\cdot\mathbf{r}_s)}{r_s^2}]) + \sum_{i\neq j}\frac{\hbar^2\gamma_e^2}{r_{ss}^3}[\mathbf{S}_i\cdot\mathbf{S}_j - 3\frac{(\mathbf{S}_i\cdot\mathbf{r}_{ss})(\mathbf{S}_j\cdot\mathbf{r}_{ss})}{r_{ss}^2}] \tag{1.7}$$

where $\mathbf{r}_s$ is the distance between the NV center and surface spin i and $\mathbf{r}_{ss}$ is the distance between surface spins i and j. The NV zero-field splitting is the largest energy in the system, so we can make the secular approximation and retain only terms that commute with $J_{z'}$. The next largest term is the surface spin Zeeman energy, so we can again make a secular approximation and retain only terms that commute with $S_{z''}$, where z'' points along the direction of the external magnetic field. After making these secular approximations, we are left with the following Hamiltonian:

$$H = \sum_i \frac{\hbar^2\gamma_e^2}{r_s^3}(1-3\cos^2\theta_s)S^{z'}J^{z''} + \sum_{i\neq j}\frac{\hbar^2\gamma_e^2}{r_{ss}^3}(1-3\cos^2\theta_{ss})(J_i^{z''}J_j^{z''} - \frac{1}{2}J_i^{x''}J_j^{x''} - \frac{1}{2}J_i^{y''}J_j^{y''}) \tag{1.8}$$

where θ_s is the angle the vector $\mathbf{r}_s$ makes with the magnetic field, and θ_{ss} is the angle the vector $\mathbf{r}_{ss}$ makes with the magnetic field. In order to map the positions of the surface spins, we perform DEER measurements at different magnetic field orientations, which modulates the $\cos^2\theta_s$ and $\cos^2\theta_{ss}$ terms of the dipolar interaction. We also fit the surface spin T_2 measurement in conjunction with the DEER measurements in order to map the positions since the surface spin T_2 measurement depends on the locations of the proximal surface spins, fig. 1.5 (a). The surface spin T_2 measurement was weighted equally with all DEER measurements combined when performing the fit. The blue line in the fits are to the best fit 3 surface spin positions.

We can create maps of surface spin positional probability by holding the positions of 2 of the surface spins fixed and varying the position of the other spin, calculating the resulting χ^2. Fig. 1.5 (b) is a probability map of the 3 surface spins (x,y) position, with a position of (0,0) corresponding to the position of the NV center, a depth d below the surface. Each spin corresponds to a different color and the color value at each pixel corresponds to the best fit χ^2 divided by the χ^2 value for a certain surface spin at that position. The white Xs correspond to the best fit positions of the 3 surface spins.

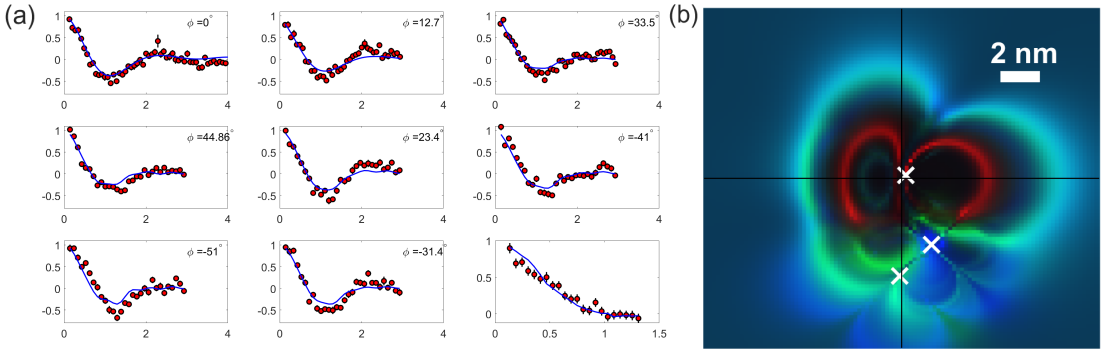


Figure 1.5: (a) DEER data taken at 8 different magnetic field angles (external magnetic field $\approx$ 45 G). Bottom right plot is T_2 data (external magnetic field $\approx$ 1343 G). Blue line corresponds to the best global fit for a system of 3 surface spins. (b) Extracted probability map of the 3 surface spins, with each color corresponding to the inverse of the reduced χ^2 value for a surface spin in that position, while the other 2 surface spins have best-fit positions.

1.4.3 The Correlation Spectroscopy Pulse Sequence

We study the dynamics of an individual central surface spin S_j, by measuring its spin autocorrelation functions. Quantum logic gates between the NV center and the central surface spin correlate the NV and the central spin evolution, via their magnetic-dipole interaction, fig. 1.6(a)[33]. Each measurement consists of a sequence of RF pulses, applied to the NV and surface spins, as well as NV optical spin polarization and readout steps. The RF pulse sequences include two probe segments (CNOT gates), in which the NV center probes the quantum state of the surface spin ensemble, separated by a time interval, in which this state can evolve with control pulses applied to the surface

spins (grey box). The interpulse spacing t_{NV} of the probe segments is tuned to the timescale of the dipolar interaction between the NV center and the central surface spin so that the final NV center state is contingent on whether the z-projection of the central surface spin changes between the gates. Applying this method, the NV center acts as a probe of central surface spin autocorrelation functions $\langle S_j^{x,y,z}(t) S_j^{x,y,z}(0) \rangle$, where the time t and the measured spin projection depend on the pulses applied during the evolution interval (grey box).

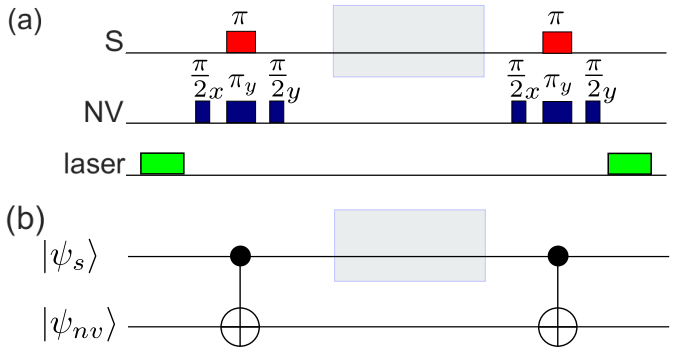


Figure 1.6: (a) The correlation spectroscopy pulse sequence. In our experiments the NV center interpulse spacing is set such that the NV center is primarily sensitive to the central surface spin S_z autocorrelation. Manipulating the surface spins during the gray shaded region allows us to measure different central surface spin correlation functions. (b) Quantum logic gate representation of the correlation spectroscopy pulse sequence. The two CNOT gates are applied, such that the final state of the NV center is contingent on whether the z-projection of the central surface spin changed during the time between the gates.

To understand this sequence, we will follow the NV center phase accumulation after each set of pulses. After the initial $\frac{\pi}{2}_x^{NV} - \pi_y^{NV} \pi^{SS} - \frac{\pi}{2}_y^{NV}$ pulses, the NV phase accumulation φ_1 due to the surface spin S_z state is projected along the NV z-axis. If the NV state is read out at this time, the NV population would be $\sim \langle \sin \varphi_1 \rangle$. By applying two sequences of $\frac{\pi}{2}_x^{NV} - \pi_y^{NV} \pi^{SS} - \frac{\pi}{2}_y^{NV}$ pulses, the initial and final surface spin S_z projections are converted to population along the NV z-axis, with an amplitude related to $\langle \sin \varphi_1 \sin \varphi_2 \rangle$ where φ_2 is the phase the NV spin acquires during the final $\frac{\pi}{2}_x^{NV} - \pi_y^{NV} \pi^{SS} - \frac{\pi}{2}_y^{NV}$ pulses.

For all correlation spectroscopy sequences that we perform, we normalize the result by the corre-

lation spectroscopy contrast. We define the contrast as the NV spin population difference between when we run the correlation spectroscopy pulse sequence (fig. 1.6(a)) without any pulses applied during the grey shaded region and when we run the sequence with a pi pulse applied to the surface spins during this time. We normalize the final signal between +1 and -1, plotting $4\langle S_z(t_0+t)S_z(t_0)\rangle$.

2

Characterization of the Local Magnetic Environment of the Surface Spins

Using the correlation spectroscopy pulse sequence, the NV center acts as a probe of central surface spin autocorrelation functions $\langle S_j^{x,y,z}(t) S_j^{x,y,z}(0) \rangle$, where the time t and the measured spin projection depend on the pulses applied during the evolution interval. We characterize the central surface spin environment for a number of systems, and in this chapter, we present the results and analysis

for one representative system.

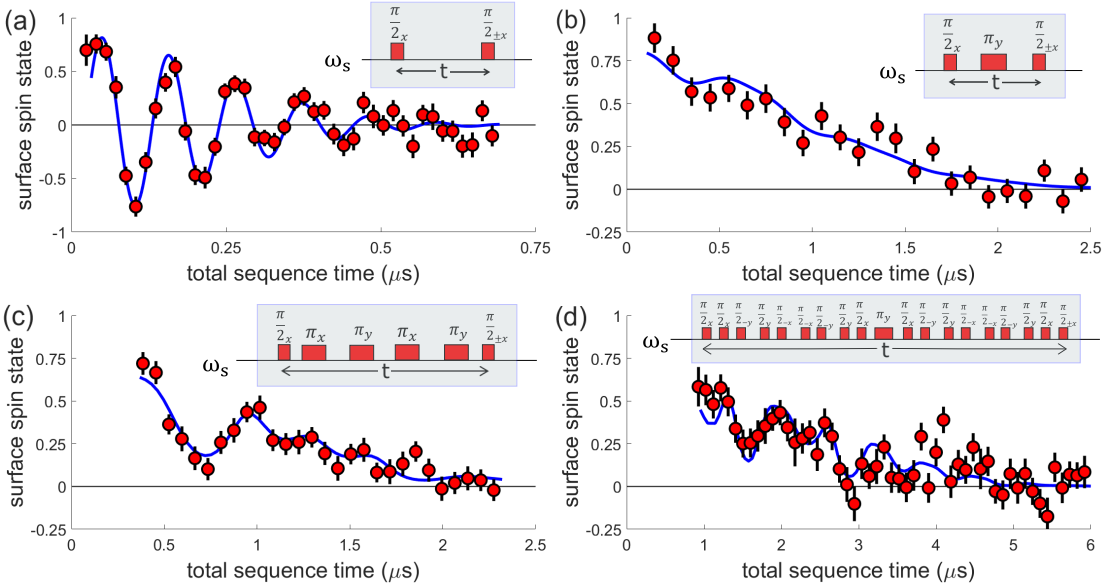


Figure 2.1: Characterization of the local magnetic environment of a central surface spin. Solid lines are fits using the model in eqs. (3.1,3.2). (a) Surface spin detuned Ramsey measurement of $\langle S_j^x(t) S_j^x(0) \rangle$ transverse central spin autocorrelation. The Ramsey decay time is T_2^* = (0.32 $\pm$ 0.02) μs. Solid lines are fits using the model in eqs. (2.1,2.2). The oscillations in the Ramsey data are due to the 9.2 MHz detuning from the surface spin Larmor frequency. (b) Surface spin Hahn echo measurements of $\langle S_j^x(t) S_j^x(0) \rangle$ transverse central spin autocorrelation. The Hahn echo decay time is T_2 = (1.41 $\pm$ 0.11) μs. (c) Surface spin XY-4 measurement, with oscillations due to proton nuclear spin precession. (d) Surface spin MREV-8 measurement performed within a spin echo with oscillations due to proton nuclear spin precession.

The four main pulse sequences we apply to probe the local environment of the central surface spin are the Ramsey, Hahn echo, XY-4, and MREV-8 sequences. The Ramsey measurement probes fluctuations of the local magnetic field at the central surface spin site (fig. 2.1 (a)). The Hahn echo sequence decouples the central surface spin from low-frequency fluctuations, which extends the coherence time to T_2 (fig. 2.1 (b)). Further decoupling can be achieved with higher-order dynamical decoupling experiments, such as XY-4 (fig. 2.1 (c)). However we observe that this does not further increase the coherence time, indicating the presence of a separate decoherence mechanism. The presence of dipolar interactions with other surface spins motivates the MREV-8 experiment, which

decouples dipolar interactions. Indeed, we observe that the coherence time in an MREV-8 experiment is extended, compared to the Hahn echo and XY-4 (fig. 2.1 (d)), showing that the dynamics of surface spins are strongly affected by dipolar interactions between them.

In order to understand our observations quantitatively, we consider the effective Hamiltonian in the rotating frame of a single surface spin S_j:

$$H_j = \hbar\gamma_e B_j^z(t) S_j^z + \sum_i \frac{\hbar^2\gamma_e^2}{r_{ij}^3}(1 - 3\cos^2\theta_{ij})[S_i^z S_j^z - \frac{1}{4}(S_i^+ S_j^- + S_i^- S_j^+)], \tag{2.1}$$

where $\hbar$ is the reduced Planck constant, $\gamma_e = 2\pi \times 2.80$ MHz/G is the electron gyromagnetic ratio, $B_j^z(t)$ is the fluctuating magnetic field at the site of the surface spin, r_{ij} is the distance between the central surface spin j and a different surface spin i, and θ_{ij} is the angle between the direction of the applied external magnetic field and the vector r_{ij}. In Eq. (2.1) we do not include the dipolar interaction between the NV center and the central surface spin. By running experiments that vary the NV center spin state during the surface spin evolution period, we find that this interaction does not affect central surface spin evolution within our experimental uncertainty.

Let us consider the origin of the fluctuating local magnetic field B_j^z. All measurements were preformed with the diamond surface submerged in deuterated glycerol. This reduced the density of proton nuclear spins near the surface. However, as observed in several other studies of near-surface NV centers, an intrinsic ~ 1 nm thick layer of surface water and hydrocarbons contains a high density of proton nuclear spins [5,6,34,13]. The periodic features that appear at odd multiples of proton Larmor period in the spin echo, XY-4, and MREV-8 data indicate that these protons are the dominant source of the local field B_j^z. We model the dynamics of B_j^z by parametrizing its power spectrum as a combination of two peaks:

$$V(\omega) = \int_{-\infty}^{\infty} \langle B^z(t)B^z(0)\rangle e^{-i\omega t}\,dt = 2\frac{W^2}{\gamma_e^2}\left(\frac{\tau}{\omega^2\tau^2+1} + \frac{5}{9}\frac{\tau}{(\omega-\omega_L)^2\tau^2+1}\right). \tag{2.2}$$

The first term, centered at zero frequency, quantifies slow fluctuations with strength W and correlation time τ, due to proton spin projections along the bias magnetic field. The second term quantifies fluctuations near the proton Larmor frequency, due to transverse proton spin projections (fig. 2.2).

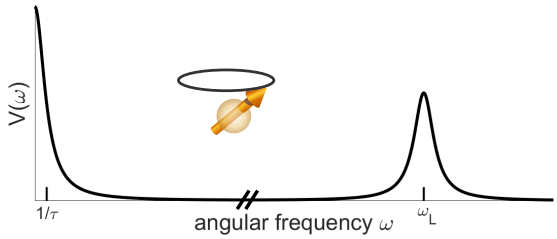


Figure 2.2: Nuclear spin bath noise power spectrum V(ω), with peaks at zero frequency and proton Larmor frequency ω_L.

2.1 Decoherence due to the Nuclear Spin Bath

For the pulse sequences applied to the surface spins, we calculate the expected signal from the nuclear spin bath with noise spectrum given by eq. (2.2). For a given sequence, the expected signal can be written as

$$S(t) = e^{-\chi(t)} \tag{2.3}$$

where

$$\chi(t) = \gamma_e^2 \int \frac{d\omega}{2\pi} \frac{V(\omega)}{\omega^2} F(\omega t) \tag{2.4}$$

where $F(\omega t)$ is the filter function of the pulse sequence and t is the total sequence time. In order to simplify calculations, we treat the peak at proton Larmor frequency ω_L as a delta function

$$V_2(\omega) = 2\pi\frac{5}{9}\frac{W^2}{\gamma_e^2}\delta(\omega - \omega_L). \tag{2.5}$$

We select a delta function with a factor of 2π in front so that the integral of the Lorentzian is matched by the integral of this delta function, and we numerically verify that for our given pulse sequences, the response due to a narrow Lorentzian is consistent with the response due to a delta function. For the Ramsey pulse sequence with filter function $F_{Ramsey}(\omega t) = 2\sin^2(\omega t/2)$, the expected decay due to the nuclear spin bath is

$$S_{Ramsey}(t) = e^{-(Wt/\sqrt{2})^2} e^{W^2t^3/(6\tau)} e^{-2\frac{5W^2}{9\omega_L^2}\sin^2(\omega_L t/2)}. \tag{2.6}$$

The filter function for the spin echo sequence is $F_{echo}(\omega t) = 8\sin^4(\omega t/4)$, and the expected signal decay due to the nuclear spin bath is

$$S_{echo}(t) = e^{-\frac{W^2t^3}{12\tau}} e^{-\frac{40W^2}{9\omega_L^2}\sin^4(\omega_L t/4)}. \tag{2.7}$$

The XY-4 pulse sequence has the filter function $F_{XY-4}(\omega t) = 128\sin^6(\omega t/16)(\cos(3\omega t/16) + \cos(5\omega t/16))^2$ and the decay due to the nuclear spin bath is given by

$$S_{XY-4}(t) = e^{-\frac{13W^2t^3}{4500\tau}} e^{-128\frac{5W^2}{9\omega_L^2}\sin^6(\omega_L t/16)(\cos(3\omega_L t/16)+\cos(5\omega_L t/16))^2}. \tag{2.8}$$

The MREV-8 sequence in an echo has a filter function given by

$$\begin{aligned} F_{MREV}(\omega t) = 16(1 + 2\cos(\omega t/12))^2(\sin(\omega t/12) - \sin(\omega t/6)^4(3 - 4\cos(\omega t/24)+ \\ 3\cos(\omega t/12) - 2\cos(\omega t/8) + \cos(\omega t/6)) \end{aligned} \tag{2.9}$$

with a resulting signal of

$$-\log(S_{MREV}(t)) = \frac{49W^2t^3}{2592\tau} + 16\frac{5W^2}{9\omega_L^2}(1+2\cos(\omega_L t/12))^2(\sin(\omega_L t/12)-\sin(\omega_L t/6)^4\times$$
$$(3-4\cos(\omega_L t/24)+3\cos(\omega_L t/12)-2\cos(\omega_L t/8)+\cos(\omega_L t/6)). \tag{2.10}$$

For each of the pulse sequences, the resulting signal has two components: a decay envelope due to the noise spectrum peak at zero frequency and a modulation due to the oscillating signal at proton Larmor frequency.

2.1.1 Decay due to Dipolar Interactions

While the central surface spin Ramsey, echo, and XY measurements will be affected by the nuclear spin bath, the dipolar interations between the central surface spin and nearby surface spins will also cause decoherence. If there were one other surface spin in the system interacting with the central surface spin with dipolar interaction strength $J_{max} = \frac{\hbar\gamma_e^2}{r^3}(1-3\cos^2\theta)$, the resulting signal for the Ramsey, echo, and XY sequences would be

$$S_{Ramsey,XY-4,Echo}(t) = \frac{1}{2}[\cos(3J_{max}t/4)+\cos(J_{max}t/4)]. \tag{2.11}$$

On short time scales, the central surface spin is mostly sensitive to nearest neighbor dipolar interactions, so we approximate the decay profile as a stretched exponential with a power of 2, $S(t) = e^{-(t/T_2)^2}$, with decay time $T_2 \approx 1/J_1$. If we assume that the decoherence due to dipolar interactions and the nuclear spin bath are independent processes, then we can express the overall Ramsey, echo, and XY-4 decoherence as the product of the stretched exponential decay due to dipolar interactions with the decay and modulation due to the nuclear spin bath. Therefore, as an example, the fit function for the XY-4 measurement becomes

$$S_{XY-4}(t) = \exp(-(t/T_2)^2)\exp(-\frac{13W^2t^3}{4500\tau})\exp(-128\frac{5W^2}{9\omega_L^2}\sin^6(\omega_L t/16)\times [\cos(3\omega_L t/16)+\cos(5\omega_L t/16)]^2) \tag{2.12}$$

where ω_L is the proton Larmor frequency.

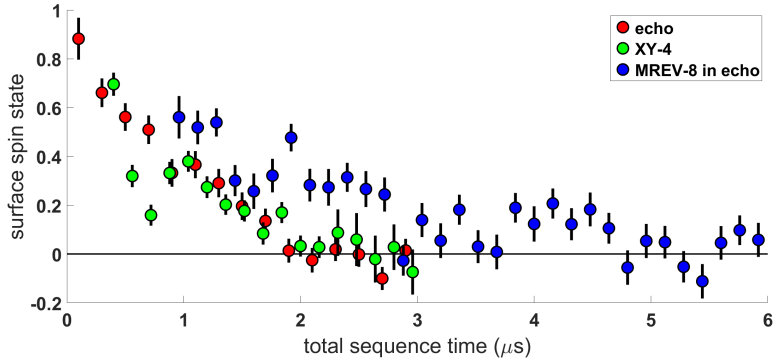


Figure 2.3: Comparison of surface spin echo, XY-4, and MREV-8 measurements, showing the extension of coherence time with MREV-8 and the decoupling of the central spin from homonuclear dipolar interactions with other surface spins.

We can show that the dominant source of decoherence in the echo and XY-4 sequences comes from dipolar interactions between surface spins by comparing the decay rate of the echo, XY-4, and MREV-8 measurements, fig. 2.3. If the nuclear spin bath were the primary source of decoherence for the echo or XY-4 sequences, there would be an extension of the coherence time between the echo and XY-4 measurement results. However, the echo and XY-4 measurements decay over the same timescale. Moreover, after applying an MREV-8 sequence, which decouples surface spins from homonuclear dipolar interactions, the coherence time increases, suggesting that dipolar interactions between surface spins are the primary contributor to decoherence in echo and XY-4 measurements.

Since we have shown that the surface spin echo and XY-4 measurements decay primarily due to dipolar interactions with other surface spins, the question remains of how the decay timescale

T_2 relates to the magnitude of these interactions. To address this question, we perform numeric simulations of surface spin echo with a system of 7 surface spins, one central spin plus 6 bath spins. The position of the central spin is fixed, but we vary the the positions of the bath spins for a range of average separations between 4 and 12 nm between surface spins. We can then fit each resulting decay curve to a stretched exponential, and we find that a stretched exponential with a power of 2 best fits the initial decay of the simulation results. For each set of bath spin positions, we extract the decay rate $(1/T_2)$ and find that it best correlates with the maximum dipolar interaction strength between the central spin and a neighbor, fig. 2.4. We find that $(1/T_2) = bJ_{max}$ where $b = (0.501 \pm 0.003)$ and J_{max} is the maximum dipolar interaction strength $\frac{\hbar\gamma_e^2}{r^3}(1 - 3\cos^2\theta)$ of the central surface spin with another surface spin.

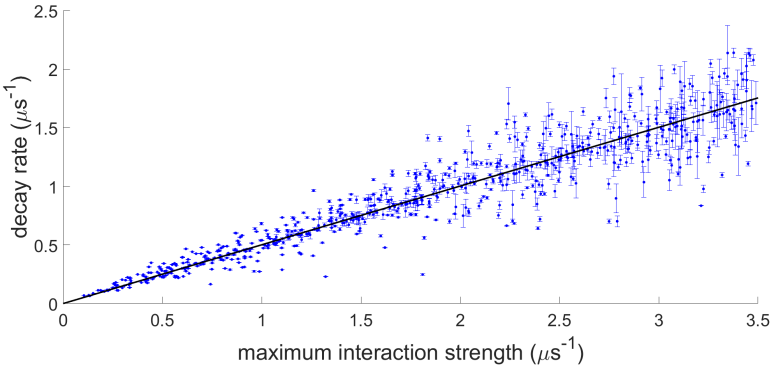


Figure 2.4: Spin echo decay results for 1 central spin plus 6 bath spins, measuring the central spin autocorrelation for different bath spin positions. The extracted decay rates versus maximum interaction strength was linearly fit to find $(1/T_2) = bJ_{max}$ where $b = (0.501 \pm 0.003)$. The y error bars correspond to the uncertainty in the fit to each simulation result.

In the next chapters, we discuss the role of intrinsic disorder due the Ising component of the dipolar Hamiltonian and define a parameter J_1, quantifying the strength of this intrinsic disorder. We approximate the intrinsic disorder as primarily coming from the strongest interacting neighboring spin to the central spin, and we can relate the magnitude of the intrinsic disorder to the maximum interaction strength as $J_1 = \frac{1}{2}J_{max}$. When we fit the Ramsey, echo, and XY-4 sequences to

the contribution coming from the dipolar interactions with other surface spins, we fit the results to $S(t) = e^{-(t/T_2)^2} = e^{-(Jt)^2}$.

2.2 Extraction of Surface Spin On-site Disorder Strength W

In the previous sections, we calculated the expected signals given dipolar interactions and the nuclear spin bath. For the experimentally relevant regime where the nuclear spin correlation time τ is much longer than the sequence duration, a detuned Ramsey sequence decay is given by

$$S_{Ramsey}(t) = \cos(\Delta t) e^{-(t/T_2)^2} e^{-(Wt/\sqrt{2})^2} e^{-2\frac{5W^2}{9\omega_L^2}\sin^2(\omega_L t/2)} \tag{2.13}$$

where Δ is the detuning between the surface spin splitting ω_S and the microwave drive frequency. By fitting the echo and XY-4 measurements, T_2 can be extracted, so W is the only free parameter in a Ramsey fit. For the data presented in fig. 2.1 (a), $W = (4.40 \pm 0.38)\,\mu s^{-1}$ is extracted.

2.3 Extraction of Proton Nuclear Spin Signal Correlation Time τ

In a previous section, we found the MREV-8 decay to be given by

$$\begin{aligned} -\log(S_{MREV}(t)) = \frac{49W^2t^3}{2592\tau} + 16\frac{5W^2}{9\omega_L^2}(1+2\cos(\omega_L t/12))^2(\sin(\omega_L t/12) - \sin(\omega_L t/6)^4 \\ \times(3 - 4\cos(\omega_L t/24) + 3\cos(\omega_L t/12) - 2\cos(\omega_L t/8) + \cos(\omega_L t/6)). \end{aligned} \tag{2.14}$$

Since MREV-8 decouples surface spins from dipolar interactions with other surface spins, the decay envelope is determined by the disorder width W and the nuclear spin correlation time τ. We extracted the disorder width from the Ramsey decay so by fitting the MREV-8 decay, we can extract

the nuclear spin correlation time $\tau = (14.6 \pm 4.2)\,\mu$s. For all central surface spin systems, we do simultaneously fit the Ramsey, spin echo, XY-4, and MREV-8 experimental data with J_1, W, and τ as fit parameters.

2.4 Extracting the Surface Spin Density

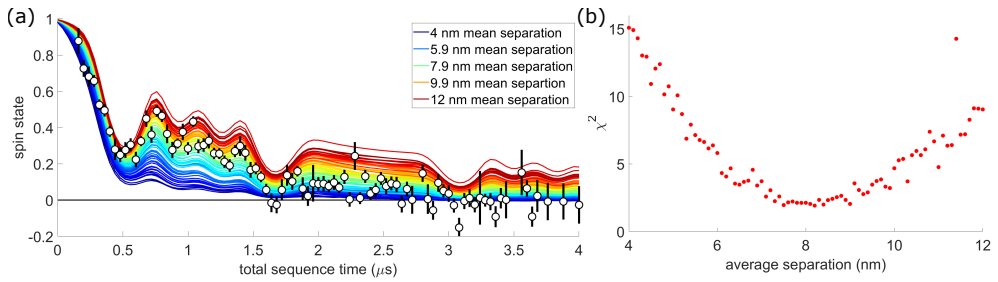


Figure 2.5: (a) Simulation results with averaged experimental data (white dots). (b) χ^2 vs average separation, where an average separation between surface spins of 8.4 ± 1.3 nm is extracted.

We extract the average surface spin density by comparing the results of numeric simulations to averaged experimental data, fig. 2.5. We begin by averaging all XY-4 data taken at an external magnetic field of 730 G and we fit the periodic features in the data, extracting a value of W of $(4.13 \pm 0.24)\,\mu s^{-1}$. Next we perform numeric simulations with a central surface spin and five neighboring surface spins. We perform simulations for different values of average separation between spins and average together the results for 500 averages with random spin positions for each value of average separation. We extract an average surface spin separation of (8.4 ± 1.3) nm. This corresponds to an average interaction strength $J = J_0 n^{3/2} = (0.57 \pm 0.25)\,\mu s^{-1}$.

3

Surface Spin Relaxation

In the previous chapter, the local environment of the central surface spin was characterized. The effective Hamiltonian in the rotating frame of a single surface spin S_j can be written as

$$H_j = \hbar\gamma_e B_j^z(t) S_j^z + \sum_i \frac{\hbar^2\gamma_e^2}{r_{ij}^3}(1 - 3\cos^2\theta_{ij})[S_i^z S_j^z - \frac{1}{4}(S_i^+ S_j^- + S_i^- S_j^+)], \tag{3.1}$$

where $\hbar$ is the reduced Planck constant, $\gamma_e = 2\pi \times 2.80$ MHz/G is the electron gyromagnetic ratio, $B_j^z(t)$ is the fluctuating magnetic field at the site of the surface spin, r_{ij} is the distance between the central surface spin j and a different surface spin i, and θ_{ij} is the angle between the direction of the applied external magnetic field and the vector r_{ij}. The nearest neighbor dipolar interaction strength J_1, the average dipolar interaction strength J, and the width W and correlation time τ of $B_j^z(t)$ can all be extracted by applying different pulse sequences and measuring the decay times as demonstrated in the previous chapter.

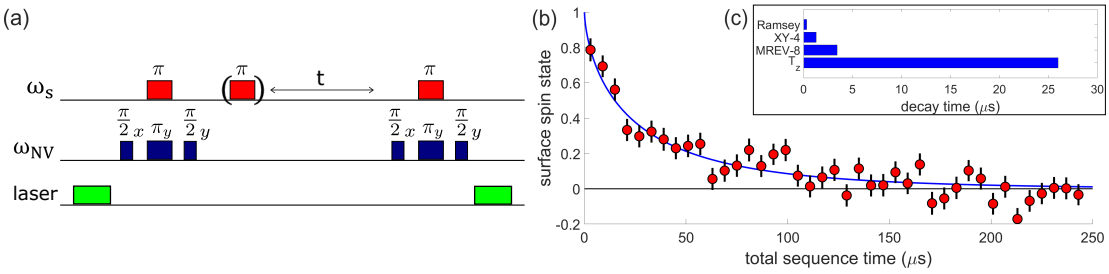


Figure 3.1: Measurement of central surface spin $\langle S_j^z(t) S_j^z(0) \rangle$ autocorrelation. (a) S^z autocorrelation measurement pulse sequence where the time between the initial and final pulse blocks is swept. A π pulse is applied to the surface spins during the free precession interval half of the time. The time between NV pulses is tuned to the dipolar interaction timescale between the NV center and the central surface spin, as calibrated using DEER and a correlation spectroscopy NV tau sweep. (b) S^z autocorrelation measurement for the central surface spin system characterized in chapter 2, with J_1 = (0.71 $\pm$ 0.05) μs^{-1}, W = (4.40 $\pm$ 0.38) μs^{-1}, and τ = (14.6 $\pm$ 4.2) μs. Blue line fit to $\exp\left(-(t/T_z)^{2/3}\right)$ (c) The full characterization of relaxation timescales for one of the central surface spin systems, including the Ramsey, XY-4, MREV-8, and S^z autocorrelation measurements.

Having characterized the local environment of the central surface spin, we study the spin flip-flop transport dynamics in this system by measuring the autocorrelation of the spin component along the applied magnetic field: $\langle S_j^z(t) S_j^z(0) \rangle$, fig. 3.1(a). The presence of the S^+S^- flip-flop terms in the dipolar interaction in Eq. (3.1) motivates an expectation that this single-spin autocorrelation would decay over the time scale T_z, which is on the order of $1/J_1 = T_2$. In contrast, we observe remarkably slow decay of the longitudinal correlation (fig. 3.1(b)), which persists over a time scale T_z, in this instance $\sim$ 30$\times$ slower than the dipolar interaction time scale T_2, fig. 3.1(c). We emphasize that

these observations are especially unexpected for individual spin measurements, in contrast with experiments probing a macroscopic spin ensemble (such as a bulk magnetic resonance measurement), where the total spin z-projection is unaffected by flip-flops within the ensemble.

3.1 Resonance Counting Theory

We attribute such anomalously slow relaxation dynamics to the presence of strong disorder. To quantify its effect, we consider a theory model based on an effective single-particle resonance counting with the Hamiltonian shown in Eq. (3.1). We follow the treatment presented in [30], which also treats the case of quasi-static on-site fields.

3.1.1 Dynamic Disorder Model

In this model, each spin S_j experiences a time-dependent energy shift owing to the combination of two effective sources of disorder: i) the extrinsic on-site disordered magnetic field $B_j^z(t)$ of typical strength $\sim W$ and ii) the intrinsic local field of strength $\sim J_1$ arising from the Ising component of the dipolar interactions among surface spins. These two components have distinct correlation times and strengths. We estimate the survival probability of a central spin based on simple resonance counting arguments. The probability of a given spin being on resonance with the central spin is given by $\frac{\beta J_0/r^3}{W}$, where $J_0 = \hbar\gamma_e^2, J_0/r^3$ is the interaction strength of the central spin with a bath spin a distance r away, W is the disorder width, and β is a dimensionless parameter that characterizes the resonance probability, of order unity. We consider the case of time-dependent disorder, where the value of on-site detuning δ_j changes over time by uncorrelated jumps at a rate $\gamma = 1/\tau$. We consider the case where $W \geq nJ_0 > 1/\tau$. As presented in [30], two spins j and i are "resonant" at time t if (1) $|\delta_j(t) - \delta_i(t)| < \beta J_0/r^3$ at any time less than t, fig. 3.2, and (2) the interaction occurs on a time-scale $t > \frac{1}{\beta J_0/r^3}$. Otherwise, energy conservation blocks flip-flops.

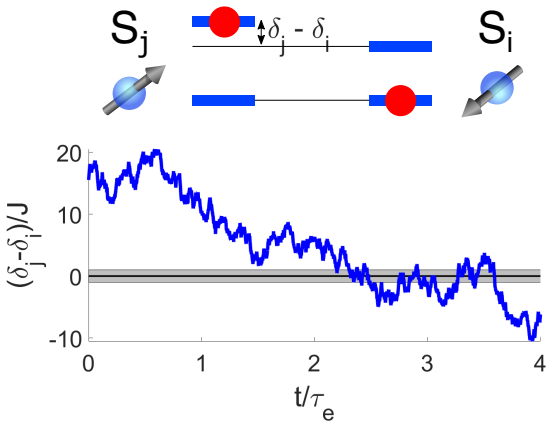


Figure 3.2: A schematic of the spin hopping process in our model, showing a central surface spin S_j and another surface spin S_i. Each spin state is shifted by time-dependent on-site detuning ∂ (blue line), due to the local dynamical disorder created by nuclear spin bath noise and Ising dipolar interaction terms. The spins can flip-flop if their detunings differ by less than the strength J of the dipolar interaction between them (grey band).

The probability of having a resonant pair is given by

$$P_{res}(t) = 1 - e^{-\frac{\beta J_0/r^3}{W}\frac{t}{\tau}}(1 - \frac{\beta J_0/r^3}{W}). \tag{3.2}$$

For a 2D spin system with density n, we can calculate the probability of a central spin having no resonance as

$$P(t) = \exp(-\int_{r_0}^{R(t)} 2\pi n r P_{res}(t) dr). \tag{3.3}$$

Note that $R(t) = (J_0 t)^{1/3}$. When $\frac{\beta J_0/r^3}{W}$ is small (at large times), $(1 - \frac{\beta J_0/r^3}{W})$ can be rewritten as $\exp(-\frac{\beta J_0/r^3}{W})$ and

$$P_{res}(t) = 1 - e^{-\frac{\beta J_0/r^3}{W}(\frac{t}{\tau}+1)}. \tag{3.4}$$

We can write the probability that the central spin has no resonance as

$$P(t) = \exp(-\int_{r_0}^{R(t)} 2\pi nr(1 - e^{-\frac{\beta J_0/r^3}{W}(\frac{t}{\tau}+1)})dr). \tag{3.5}$$

To simplify the expression, we can take the $-log$ of each side:

$$-\log(P(t)) = \int_{r_0}^{R(t)} 2\pi nr(1 - e^{-\frac{\beta J_0/r^3}{W}(\frac{t}{\tau}+1)}dr). \tag{3.6}$$

We can next perform a change of variables to evaluate the integral. We define

$$z = \frac{\beta J_0/r^3}{W}(\frac{t}{\tau} + 1). \tag{3.7}$$

We can rewrite this in terms of r as

$$r = (\frac{\beta J_0/z}{W}(\frac{t}{\tau} + 1))^{1/3}. \tag{3.8}$$

Using the fact that $2rdr = d(r^2)$, we can rewrite the expression for $P(t)$ in terms of z:

$$-\log(P(t)) = \int_{r(z,t)}^{R(z,t)} n\pi(1 - e^{-z})d(\frac{\beta J_0/z}{W}(\frac{t}{\tau} + 1))^{2/3} \tag{3.9}$$

which becomes

$$-\log(P(t)) = \int_{z_0(r_0,t)}^{z(r,t)} n\pi(1 - e^{-z})(-2/3)z^{-5/3}dz(\frac{\beta J_0}{W}(\frac{t}{\tau} + 1))^{2/3}. \tag{3.10}$$

We can then rewrite $-\log(P(t))$ as the product of two terms:

$$-\log(P(t)) = P_1(t)P_2(t) \tag{3.11}$$

$$P_1(t) = \int_{z_0(r_0,t)}^{z(r,t)} \pi(1-e^{-z})(-2/3)z^{-5/3}dz \tag{3.12}$$

$$P_2(t) = (n^{3/2}\frac{\beta J_0}{W}(\frac{t}{\tau}+1))^{2/3} \tag{3.13}$$

In the limit $t \gg \tau$, $P_2(t)$ simplifies to

$$P_2(t) = (\frac{n^{3/2}\beta J_0}{W}\frac{t}{\tau})^{2/3}. \tag{3.14}$$

We want to understand the time dependence in $P_1(t)$ so we define

$$z_0(r_0,t) = \frac{\beta J_0/r_0^3}{W}(t/\tau+1) \tag{3.15}$$

$$z(R,t) = \frac{\beta J_0/R(t)^3}{W}(t/\tau+1) \tag{3.16}$$

Since $R(t) = (J_0 t)^{1/3}$, in the limit $t \gg \tau$, z has weak dependence on time. We can numerically integrate $P_1(t)$ in order to understand the time dependence, and we plot $P_1(t)$ and $P_2(t)$ for comparison, fig. 3.3.

For times $t > \tau$, there is some dependence on time in $P_1(t)$, but it is not as strong as the time dependence in $P_2(t)$. Therefore, we can write the probability of having a resonant pair as

$$P(t) = \exp(-\alpha(\frac{n^{3/2}\beta J_0}{W\tau}(t+\tau))^{2/3}) \tag{3.17}$$

where α is the average value of P_1 at times t> τ. For our parameter range, we set $\alpha = 5$, and we have numerically verified that $P(t)$ in Eq. 3.17 is consistent with Eq. 3.5 numerically integrated

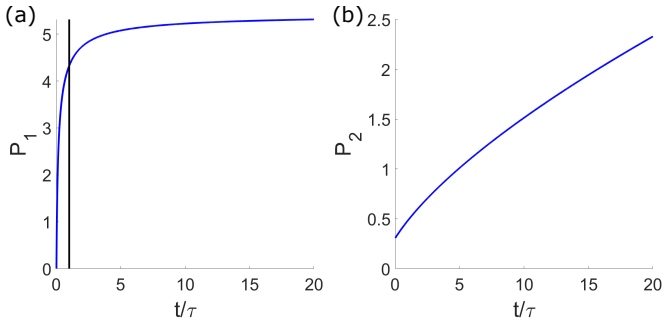


Figure 3.3: Plots of (a) $P_1(t)$ and (b) $P_2(t)$ with r_0 = 2 nm, β = 1, τ = 15 μs, W = 3.77 μs^{-1}, and J_0 = 326.7 nm$^3/\mu$s. $P_2(t)$ has a stronger dependence on time than $P_1(t)$ for times t$> \tau$.

for relevant parameters and this value of α. From this expression, we can see that changing W or τ simply amounts to changing the timescale of the decay. For times longer than τ, this model predicts that for a 2D dipolar spin system, the central spin autocorrelation $\langle S_j^z(t) S_j^z(0)\rangle$ decays with an approximate functional form $\exp\left(-(t/T_z)^{2/3}\right)$, where $T_z = \kappa \tau_e W_e/J$. The numerical constant κ is of order unity, and J is the average dipolar interaction strength over the spin ensemble.

3.1.2 Two Sources of Dynamic Disorder

We must consider the combined effects of i) the extrinsic on-site disorder from the external magnetic field $B_j^z(t)$, of typical strength W and correlation time τ, and ii) the intrinsic local field of strength $\sim J_1$ from the Ising component of the dipolar interaction among surface spins, of approximate timescale T_z. To quantify the combined dynamical disorder, we introduce the effective disorder strength W_e, defined as

$$W_e = \sqrt{W^2 + J_1^2} \tag{3.18}$$

and the effective correlation time τ_e, defined via

$$\sqrt{1/\tau_e} = \frac{W\sqrt{1/\tau} + J_1\sqrt{1/T_z}}{W_e}. \tag{3.19}$$

We compare the predicted central spin autocorrelation $\langle S_j^z(t)S_j^z(0)\rangle$ decay functional form $\exp\left(-(t/T_z)^{2/3}\right)$ with our experimental data by scaling the time axis of the autocorrelation data by independently estimated $\tau_e W_e$, and observe that the data sets for the 7 different NV-central spin systems collapse towards a universal curve, fig. 3.4(b).

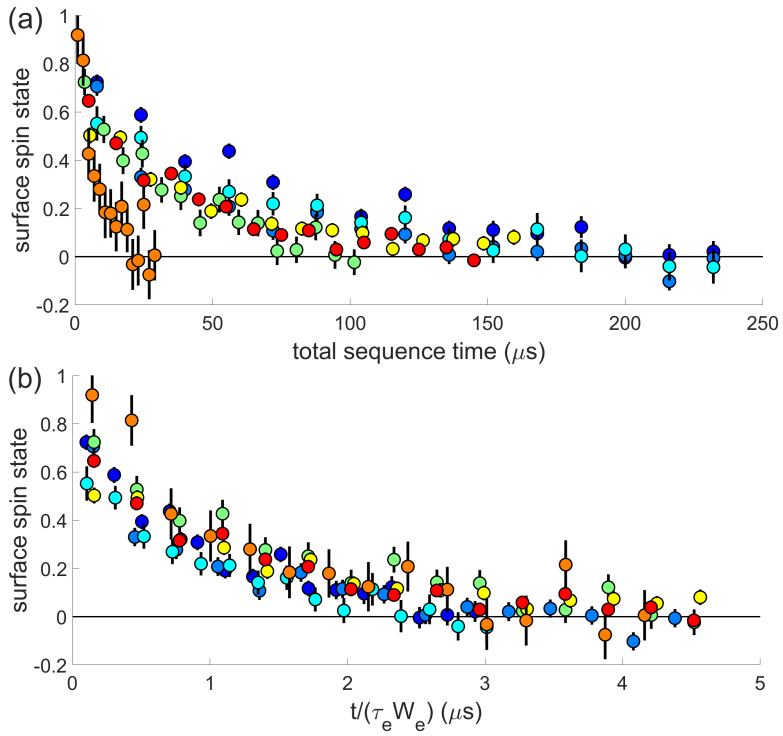


Figure 3.4: Measurements of central surface spin $\langle S_j^z(t)S_j^z(0)\rangle$ autocorrelation. Each color represents a different central surface spin system. (a) S^z autocorrelation measurements for 7 different central surface spin systems. Each measurement is fit by a stretched exponential, from which we extract the relaxation time T_z. (b) S_z autocorrelation measurements with the decay time re-scaled by the product $\tau_e W_e$ of the effective disorder correlation time and disorder width, independently measured for each surface spin system. We observe a collapse of the 7 data sets to a universal stretched-exponential decay curve, in agreement with our dynamical disorder model.

3.2 S_z Autocorrelation Scaling

Plotting the individual relaxation times T_z versus the product $\tau_e W_e$ reveals the linear relationship predicted by our resonance counting, with the best-fit value of $\kappa = (0.31 \pm 0.14)$ extracted using a value of $J = (0.57 \pm 0.25)\,\mu s^{-1}$ from our density estimates, fig. 3.5(a). We can also study the relationship between T_z and W (fig. 3.5(b)), T_z and τ (fig. 3.5(c)), and T_z and T_2 (fig. 3.5(d)).

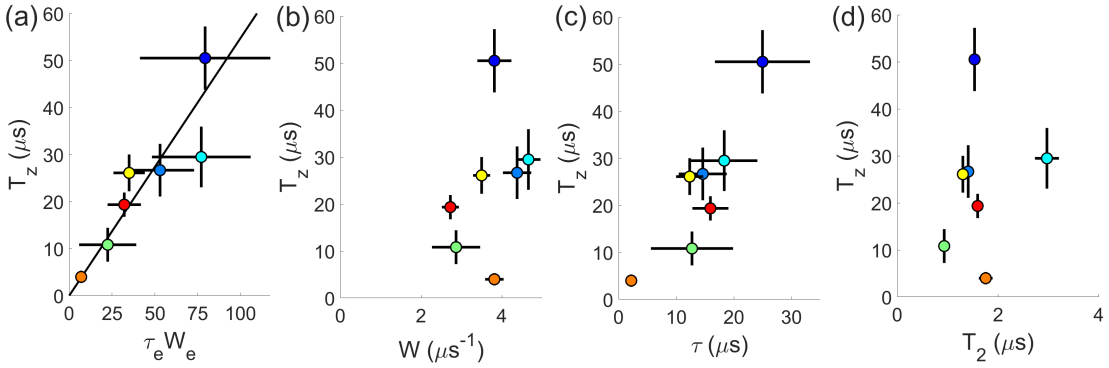


Figure 3.5: S_z autocorrelation decay time plotted as a function of different system parameters including (a) $\tau_e W_e$, (b) W, (c) τ, and (d) T_2. The colors correspond to the data sets represented in fig. 3.4. The black line in (a) is a linear fit.

3.3 Spin-lock Driving Measurements ($T_{1\rho}$)

To further investigate the role of disorder, we control the magnitude of the effective disorder by spin-lock driving, on resonance with the surface spin Larmor frequency. The resonant drive along the y-axis of the rotating frame adds to the Hamilonian (3.1) the additional term $H_d = \hbar\Omega S^y$, where Ω is the drive Rabi frequency:

$$H'_j = \hbar\gamma_e B_j^z(t) S_j^z + \Omega S_j^y + \sum_i \frac{\hbar^2\gamma_e^2}{r_{ij}^3}(1 - 3\cos^2\theta_{ij})[S_i^z S_j^z - \frac{1}{4}(S_i^+ S_j^- + S_i^- S_j^+)] \qquad (3.20)$$

We measure the dynamics of the central surface spin projection S_j^y along the driving field, fig. 3.6. This is equivalent to $T_{1\rho}$ measurement in NMR [1,53].

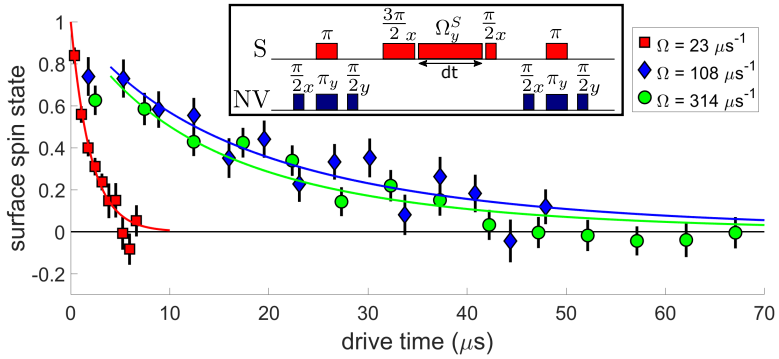


Figure 3.6: Evolution of central surface spin under spin-lock driving. Measurements of $\langle S_j^y(t)S_j^y(0)\rangle$ autocorrelation under spin-lock driving for different drive strengths. Stronger driving results in better decoupling from the nuclear spin bath magnetic noise and longer $T_{1\rho}$ relaxation time. For drive strength $\Omega \gtrsim 50\,\mu\text{s}^{-1}$, relaxation rate is independent of Ω. Lines show stretched exponential decay fits. Inset: radio frequency NV and surface spin pulses; green laser polarization and readout pulses applied before and after this sequence of RF pulses.

We consider the case of a two level system where spin operators are given by $S^\alpha = \frac{1}{2}\sigma^\alpha$. In order to further understand our observations, we move into a second interaction picture with respect to $H_d = \Omega S^y = \frac{1}{2}\Omega\sigma^y$. Our spin operators are then transformed by replacing S^α with $U^\dagger(t)S^\alpha U(t)$, where $U(t) = \exp(-i\Omega t\sigma^y/2)$. Our initial spin operators are transformed as follows:

$$S^x(t) \to \cos(\Omega t)S^{x\prime} + \sin(\Omega t)S^{z\prime} \tag{3.21}$$

$$S^y(t) \to S^{y\prime} \tag{3.22}$$

$$S^z(t) \to \cos(\Omega t)S^{z\prime} - \sin(\Omega t)S^{x\prime} \tag{3.23}$$

where $S^{\alpha\prime}$ is the spin operator in the doubly rotated frame. The resulting dipolar Hamiltonian has half the interaction strength as in the singly rotating frame:

$$H_j^{dd} = \sum_{ij} \frac{\hbar^2 \gamma_e^2}{r_{ij}^3}(1 - 3\cos^2\theta_{ij})[\frac{1}{4}S_i^{z\prime}S_j^{z\prime} + \frac{1}{4}S_i^{w\prime}S_j^{w\prime} - \frac{1}{2}S_i^{y\prime}S_j^{y\prime}]. \tag{3.24}$$

In the doubly rotating frame with respect to the drive, the Hamiltonian due to the on-site fields from the nuclear spin bath becomes

$$H_j^{nuc} = \hbar\gamma_e B_j^z(t)[\cos(\Omega t)S_j^{z\prime} - \sin(\Omega t)S_j^{w\prime}]. \tag{3.25}$$

In this new basis, the energy eigenstates are split by the effective Rabi frequency of the drive $\Omega_{eff} = \sqrt{\Omega^2 + \delta^2}$ where δ is the on-site detuning value, characterized by the power spectral density $V(\omega)$. Following the treatment in [30], the effective extrinsic disorder width at strong driving strength scales as $W_{eff} = \frac{W^2}{\sqrt{2}\Omega}$. We can numerically calculate δ values from the power spectral density $V(\omega)$ and calculate Ω_{eff} for different values of drive strength Ω, verifying that at large drive strengths, the effective on-site disorder width scales as $W_{eff} = \frac{W^2}{\sqrt{2}\Omega}$.

The relaxation at small Ω is dominated by the local magnetic field noise $B_j^z(t)$, which can flip S_j^y. We can treat the nuclear spin bath noise spectrum $V(\omega)$ as a perturbation and directly calculate the transition probability and relaxation rate given $V(\omega)$. First, let's assume that the nuclear spin bath noise is monochromatic at frequency ω:

$$H' = \hbar\gamma_e B_0 S^z \cos(\omega t). \tag{3.26}$$

The matrix element Q_{ab} is given by

$$Q_{ab} = -\frac{1}{2}\hbar\gamma_e B_0. \tag{3.27}$$

We can then calculate the transition probability as

$$P_{ab}(t) = \frac{|Q_{ab}|^2}{\hbar^2} \frac{\sin^2[(\Omega - \omega)t/2]}{(\Omega - \omega)^2} \tag{3.28}$$

$$P_{ab}(t) = \frac{\hbar^2 \gamma_e^2 B_0^2/4}{\hbar^2} \frac{\sin^2[(\Omega - \omega)t/2]}{(\Omega - \omega)^2}. \tag{3.29}$$

The above expressions are all for monochromatic perturbations. In our system, $B(t)$ is described by a power spectrum $V(\omega)$, so we need to take this into account. The energy density in CGS units of an electromagnetic wave is $U = \frac{B_0^2}{8\pi}$. We can then rewrite the transition probability as

$$P_{ab}(t) = 2\pi U \gamma_e^2 \frac{\sin^2[(\Omega - \omega)t/2]}{(\Omega - \omega)^2}. \tag{3.30}$$

Since the central surface spin is exposed to magnetic noise at a range of frequencies, we rewrite U as $\rho(\omega)d\omega$ where $\rho(\omega)d\omega$ is the energy density in the frequency range $d\omega$, and we can rewrite the transition probability as

$$P_{ab} = 2\pi\gamma_e^2 \int_0^\infty \rho(\omega) \frac{\sin^2[(\Omega - \omega)t/2]}{(\Omega - \omega)^2} d\omega. \tag{3.31}$$

Since $\frac{\sin^2[(\Omega-\omega)t/2]}{(\Omega-\omega)^2}$ is sharply peaked around Ω, we can replace $\rho(\omega)$ by $\rho(\Omega)$ and take it outside of the integral:

$$P_{ab} = 2\pi\gamma_e^2 \rho(\Omega) \int_0^\infty \frac{\sin^2[(\Omega - \omega)t/2]}{(\Omega - \omega)^2} d\omega. \tag{3.32}$$

We can solve the integral by noting that

$$\int_{-\infty}^{\infty} \frac{\sin^2 x}{x^2} dx = \pi. \tag{3.33}$$

We find that

$$P_{ab} = 2\pi\gamma_e^2\rho(\Omega)t\pi/2. \tag{3.34}$$

We find that the transition rate ($R = dP/dt$) is

$$R_{ab} = \pi^2\gamma_e^2\rho(\Omega) \tag{3.35}$$

where $\rho(\Omega)$ is the energy in the field at Ω and directly corresponds to the value of the power spectral density $V(\omega)$ at that frequency.

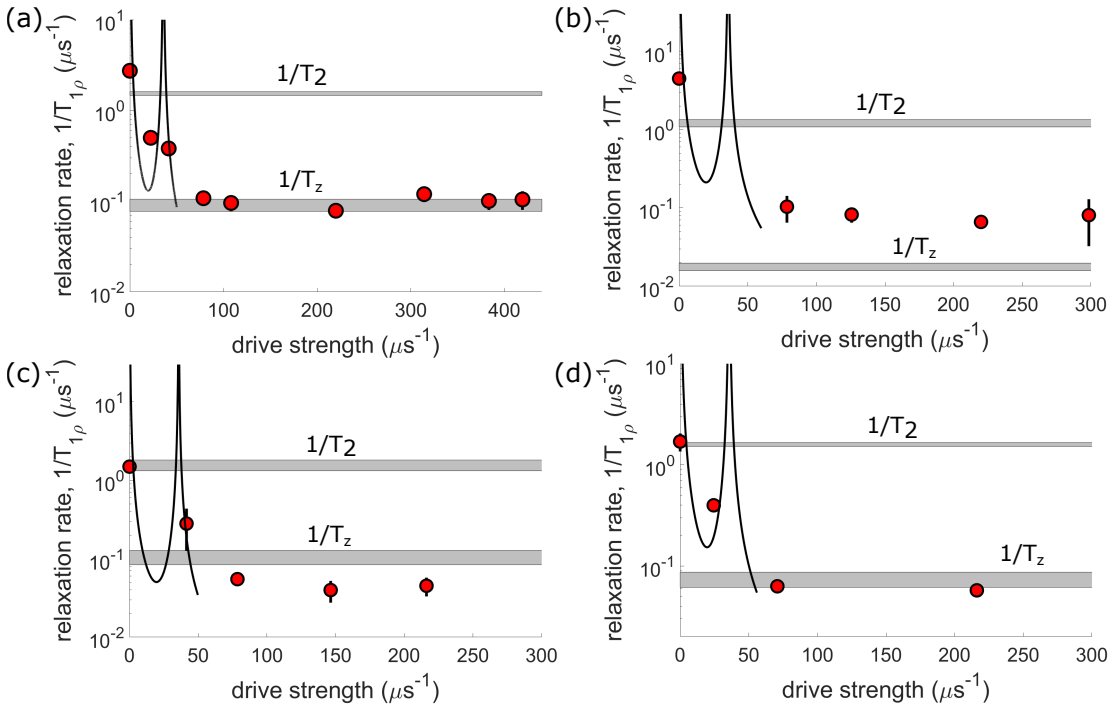


Figure 3.7: Spin-lock driving relaxation rate as a function of drive strength for 4 different surface spin systems, along with the corresponding decay rates for Hahn echo ($1/T_2$) and S^z autocorrelation ($1/T_z$) experiments, shown by the gray bands. The point at $\Omega = 0$ corresponds to the decay of the Ramsey coherence ($1/T_2$*). The measurements performed with drive strength below 50 μs^{-1} are consistent with direct relaxation due to the nuclear spin bath noise with spectrum V(ω) (black line). Relaxation rates for drive strengths $\Omega \gtrsim 50\,\mu s^{-1}$ are independent of Ω and consistently much slower than the dipolar interaction scale $1/T_2$.

We have performed $T_{1\rho}$ measurements for 4 different central surface spins systems at a variety of

drive strengths Ω, along with characterizing the central surface spin system by extracting J_1, W, and τ. For small Ω, the relaxation rate calculated using the noise model $V(\omega)$ and Eq. 3.35 is consistent with our measurements (fig. 3.7, black line). At large drive strength Ω, spin flips due to $B_j^z(t)$ are suppressed, such that the strength of the effective extrinsic disorder scales as $W^2/(\sqrt{2}\Omega)$. Consequently, the disorder experienced by individual spins is dominated by the Ising component of dipolar interactions along the dressed quantization axis S_j^y. The strength of the latter is reduced to the half of the original Ising interaction along S_j^z in the undriven case[30].

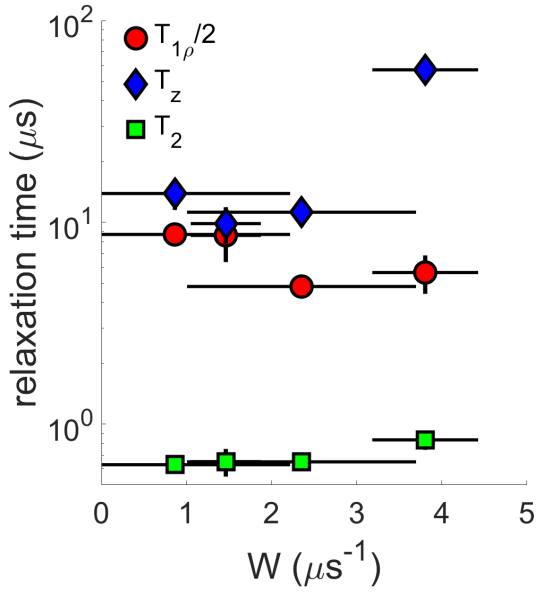


Figure 3.8: Comparison between different autocorrelation decay timescales for 4 different surface spin systems. Red circles, labeled $T_{1\rho}/2$, show the decay time under spin-lock at strong driving. As the dynamical on-site disorder strength W increases, the T_z autocorrelation decay time increases compared with the autocorrelation decay at strong driving with suppressed disorder ($T_{1\rho}/2$). Both of these decays are much slower (by a factor of $\approx$ 30) than the dipolar interaction scale, given by T_2.

Thus, systematic comparisons of $T_{1\rho}/2$ and T_z enable us to understand the interplay between the extrinsic and intrinsic disorder fields. Shown in fig. 3.8, we find that the relaxation time between $T_{1\rho}$ and T_z becomes relatively faster by suppressing the extrinsic disorder when W is sufficiently large. However, for samples with small or intermediate W, the difference in $T_{1\rho}$ and T_z is not substantial,

suggesting that the Ising interaction constitutes the dominant source of disorder in this regime. Interestingly, even in this regime, the relaxation rate is approximately a factor of 20 slower than the dipolar interaction scale J_1. This implies that, even in the absence of extrinsic on-site disorder, the intrinsic disorder associated with random positioning of spins is sufficient to strongly suppress spin transport in a 2D spin ensemble.

A full many-body theoretical treatment of a random dipolar-interacting two-dimensional spin ensemble may be needed to quantitatively predict the relaxation time scale in the absence of extrinsic disorder. A mean-field approach may also provide an approximate solution [22]. It is natural to inquire if a many-body localized phase could be observed for this system. While we do not observe localization directly within the accessible parameter range, we note that theoretical analyses of localization physics typically consider quasi-static disorder models, where the value of on-site field strength does not change on the timescale of a single measurement. Quasi-static disorder generally slows down relaxation as shown in our experiments, but our model demonstrates that time-dependent disorder may speed it up, for a subset of values of W and τ, by allowing previously off-resonant spins to become resonant. Achieving finer control over disorder parameters may allow a detailed single-spin-resolution study of various aspects of localization physics in the present system.

4

Dynamic Mean Field Models

In the previous chapter, we measured the single-spin longitudinal autocorrelation when 1) the system dynamics are governed by both dipolar interactions between surface spins and on-site local disorder from fluctuating magnetic fields and 2) the case where central spin dynamics are only determined by dipolar interactions within the surface spin system. We introduced a dynamic resonance counting model which was consistent with the relaxation timescales T_z and $T_{1\rho}$ extracted from experiment, though the model was not predictive of the $T_{1\rho}$ relaxation timescale.

4.1 Dynamic Mean Field Models in the Singly Rotating Frame

In this chapter, we present a dynamic mean-field theory for spin ensembles at infinite temperature [22] and we show that we can reproduce the extension of lifetime observed during spin-lock driving beyond that given by the dipolar interaction timescale. Let us begin by considering a system of spins S=1/2 in a large external magnetic field. The Hamiltonian for a system of dipolar interacting spins in the rotating frame is given by

$$\frac{H}{\hbar} = \frac{1}{2}\sum_{i\neq j}\frac{\hbar\gamma^2}{4R_{ij}^3}(1-3\cos^2\theta_{ij})[4\hat{S}_i^z\hat{S}_j^z - 2\hat{S}_i^x\hat{S}_j^x - 2\hat{S}_i^y\hat{S}_j^y] \tag{4.1}$$

where R_{ij} is the distance between spins i and j and θ_{ij} is the angle between R_{ij} and the direction of the externally applied magnetic field. It is assumed that on average, each spin has the same environment, so on average the spin dynamics $S^\alpha(t) = \langle S^\alpha(t)S^\alpha(0)\rangle$ are the same for each spin. Any one spin 0 interacting with a large number of spins has dynamics governed by

$$\frac{H_0}{\hbar} = 4\hat{V}^z\hat{S}_0^z - 2\hat{V}^x\hat{S}^x - 2\hat{V}^y\hat{S}^y \tag{4.2}$$

where

$$\hat{V}^z = \sum_{i\neq 0}\frac{J_0}{4R_{i0}^3}(1-3\cos^2\theta_{i0})\hat{S}_i^z \tag{4.3}$$

$$\hat{V}^x = \sum_{i\neq 0}\frac{J_0}{4R_{i0}^3}(1-3\cos^2\theta_{i0})\hat{S}_i^x \tag{4.4}$$

$$\hat{V}^y = \sum_{i\neq 0}\frac{J_0}{4R_{i0}^3}(1-3\cos^2\theta_{i0})\hat{S}_i^y \tag{4.5}$$

The $\hat{V}$-operators are sums of a large number of spin operators, and this treatment is only justi-

fiable at large distances d away from the central spin o. Since we are working on an initially unpolarized spin system at infinite temperature, the expectations values of those spin operators and their higher moments are uncorrelated at the beginning of any dynamics. The central limit theorem tells us that the $\hat{V}$-operators are Gaussian distributed and can be treated as classical stochastic variables of which the distribution is determined by the first and second moments

$$\overline{\vec{V}} = 0 \tag{4.6}$$

$$\overline{V^z(t)V^z(0)} = J_Q^2 S^z(t) \tag{4.7}$$

$$\overline{V^x(t)V^x(0)} = J_Q^2 S^x(t) \tag{4.8}$$

$$\overline{V^y(t)V^y(0)} = J_Q^2 S^y(t) \tag{4.9}$$

where J_Q is a dipolar coupling constant defined as

$$J_Q^2 = \sum_{i\neq 0} (\frac{J_0}{4R_{i0}^3})^2 (1 - 3\cos^2\theta_{i0})^2. \tag{4.10}$$

We assume an average homogeneous distribution of spins on the two-dimensional diamond surface with density n_0 in order to convert the sum in eq. 4.10 into a two-dimensional integral. We parameterize the plane of the surface by the polar coordinates (R,φ) and the external magnetic field makes an angle of α with the normal of the surface plane. We then have

$$\cos\theta = \sin\alpha\cos\varphi. \tag{4.11}$$

We can then compute the integral for J_Q^2 as

$$J_Q^2 = I(\alpha) \int_{d_{min}}^{\infty} (\frac{J_0}{4R^3})^2 n_0 dR \tag{4.12}$$

$$I(\alpha) = \int_0^{2\pi} [1 - 6\sin^2\alpha\cos^2\varphi + 9\sin^4\alpha\cos^4\varphi] d\varphi \tag{4.13}$$

and we find

$$I(\alpha) = 2\pi[1 - 3\sin^2\alpha + \frac{27}{8}\sin^4\alpha]. \tag{4.14}$$

In our measurements, the external magnetic field makes an angle of 54.7 degrees with the surface normal, so $I(\alpha) = \pi$. We can calculate J_Q as

$$J_Q = \sqrt{I(\alpha) n_0} \frac{J_0}{2d_{min}^2}. \tag{4.15}$$

We are now in a position to implement a numerical procedure by which the mean-field moments are determined by the self-consistent equations to be evaluated[22]. We begin with some initial mean-field moments and compute the autocorrelations for a single spin via the path integral and subsequently the mean-field moments via the self-consistent equations. These are then compared and the initial mean-field moments are adjusted to converge iteratively to a self-consistent solution. When applying these methods, we find that the transverse autocorrelation decays a factor of 2 faster than the longitudinal autocorrelation.

4.1.1 Extension to Inhomogeneous Magnetic Field

Now consider the case of an inhomogeneous external magnetic field where local disorder fields can act on the spins individually. The Hamiltonian in the rotated frame with on site disorder h_i for two spins is given by

$$\frac{H}{\hbar} = \frac{\hbar\gamma^2}{4R_{12}^3}(1 - 3\cos^2\theta_{12})[4\hat{S}_1^z\hat{S}_2^z - 2\hat{S}_1^x\hat{S}_2^x - 2\hat{S}_1^y\hat{S}_2^y] + h_1\hat{S}_1^z + h_2\hat{S}_2^z \tag{4.16}$$

If we pick one spin 0, its dynamics are given by

$$\frac{H_0}{\hbar} = 4\hat{V}^z\hat{S}_0^z - 2\hat{V}^x\hat{S}_0^x - 2\hat{V}^y\hat{S}_0^y \tag{4.17}$$

where

$$\hat{V}^z = \sum_{i\neq 0}\frac{J_0}{4R_{i0}^3}(1 - 3\cos^2\theta_{i0})\hat{S}_i^z + \frac{1}{4}h_0 \tag{4.18}$$

$$\hat{V}^x = \sum_{i\neq 0}\frac{J_0}{4R_{i0}^3}(1 - 3\cos^2\theta_{i0})\hat{S}_i^x \tag{4.19}$$

$$\hat{V}^y = \sum_{i\neq 0}\frac{J_0}{4R_{i0}^3}(1 - 3\cos^2\theta_{i0})\hat{S}_i^y \tag{4.20}$$

Note that in going from the two spin (or many spin) case to this mean field case, we lost information about the disorder on the sites of other spins, which may affect the accuracy of this method if there are large site-to-site variations in on-site disorder width. The on-site disorder field is Gaussian distributed with mean zero and standard deviation W. We are now in a position to once again calculate the first and second moments of the $\hat{V}$-operators:

$$\overrightarrow{\overrightarrow{V}} = 0 \tag{4.21}$$

$$\overline{V^z(t)V^z(0)} = J_Q^2 S_z(t) + \frac{1}{16}W^2 \tag{4.22}$$

$$\overline{V^x(t)V^x(0)} = J_Q^2 S_x(t) \tag{4.23}$$

$$\overline{V^y(t)V^y(0)} = J_Q^2 S_y(t) \tag{4.24}$$

The same iterative approach can be applied to calculate mean-field moments, and we find that for nonzero disorder width W, the lifetime of the longitudinal autocorrelation is greatly extended beyond that of the transverse autocorrelation.

When applying the dynamic mean field approach to fit the transverse autocorrelation (Ramsey) and longitudinal autocorrelation (T_z) measurements consistently with fitting parameter J_Q, which is related to the bath cutoff distance, we were able to achieve reasonable agreement between the model and the experimental results. However, we discovered that the longitudinal autocorrelation T_z decay timescale is largely impacted by the timescale of the dynamic disorder and when we implemented disorder with correlation time τ in the mean field model, we did not find any difference in final longitudinal relaxation timescale for a wide range of noise correlation times.

In the end, we did not use this model to fit the Ramsey and longitudinal autocorrelation T_z data since the scaling observed in experiment did not agree with simulation results. We partially attribute this discrepancy to the fact that by applying a mean field treatment, we are assuming that on average each spin in the system has the same environment. In contrast, we observe T_z timescales which can vary by an order of magnitude due to the large variation in correlation times of the extrinsic disorder.

In contrast, our measured $T_{1\rho}$ decay timescales at strong drive vary by at most a factor of 2, so we are in a better position to attempt mean field models to describe the relaxation timescale observed in

$T_{1\rho}$ than we are in T_z.

4.2 Doubly Rotated Mean Field Dipolar Hamiltonian

In our model of describing a 2 dimensional ensemble of spin-1/2 on the surface of diamond, we applied a dynamic mean field approach to describe the effects of dipolar interactions with a large number of surface spins. In a singly rotated frame about the bare Larmor splitting, the Hamiltonian for any one spin 0 interacting with a large number of spins has dynamics governed by ($\hbar = 1$):

$$H = 4V^z S_0^z - 2V^x S_0^x - 2V^y S_0^y \tag{4.25}$$

We may make another transformation and move into a doubly rotating frame about the drive ΩS^y. In doing so, we must transform both our spin operators as well as our V-operators. As a reminder, the V-operators are defined as:

$$V^\alpha = \sum_{i \neq 0} J(R_{i0})(1 - 3\cos^2\theta_{i0}) S_i^\alpha \tag{4.26}$$

Performing the necessary operations, we find that the V-operators transform as

$$V^x \to \cos(\Omega t) V^x + \sin(\Omega t) V^z \tag{4.27}$$

$$V^y \to V^y \tag{4.28}$$

$$V^z \to \cos(\Omega t) V^z - \sin(\Omega t) V^x \tag{4.29}$$

Plugging the transformed spin operators and V-operators into eq. 4.25 and performing a temporal average, we find that the Hamiltonian governing the mean-field description of the interaction of

a single spin with a large number of spins becomes

$$H' = V^z S_0^z + V^x S_0^x - 2V^y S_0^y \tag{4.30}$$

This retains a similar form to the doubly rotated dipolar interaction Hamiltonian as its effective interaction strength is halved. When we perform the self-consistent evaluation for a fixed J_Q, we find that the longitudinal autocorrelation $\langle S^y(t)S^y(0)\rangle$ lives for twice as long as the transverse autocorrelation $\langle S^z(t)S^z(0)\rangle$. Note that since we have moved into a second rotating frame about a drive along y, the longitudinal autocorrealtion is now $\langle S^y(t)S^y(0)\rangle$.

However, this still does not account for the extension in timescale we observe when comparing the $T_{1\rho}$ decay to the dipolar interaction timescale extracted from surface spin echo or XY-4, T_2. This is due to the fact that the intrinsic disorder due to the random positions of surface spins is not accounted for as of yet in the dynamic mean field model. In order to take into account intrinsic disorder, we introduce 3 spins in addition to a central spin S_0 that we directly simulate, thus pushing the cutoff distance to the bath back. We define the parameter J_{max} to be the maximum dipolar interaction strength between the central spin and one of the three bath spins, and we compute $S^y(t)$ and $S^z(t)$ using the iterative approach with J_Q as the fit parameters.

We can fit the transverse correlation $S^z(t)$ to a stretched exponential with a power of 2 and extract the decay timescale T_2, which is plotted in fig. 4.1 (a). We see that J_{max} is linearly related to T_2, consistent with our experimental observations from Chapter 2. We also fit the longitudinal correlation $S^y(t)$ to a stretched exponential with a floating power as well as a fixed power of 2/3 and extract the relaxation timescale $T_{1\rho}$, fig. 4.1 (b). For small values of J_{max}, we find a linear relationship between J_{max} and $T_{1\rho}$, consistent with the predictions of the dynamic disorder model.

For one surface spin system where we have measured the transverse spin autocorrelation from the surface spin echo, the longitudinal spin autocorrelation from the surface spin $T_{1\rho}$ at strong drive,

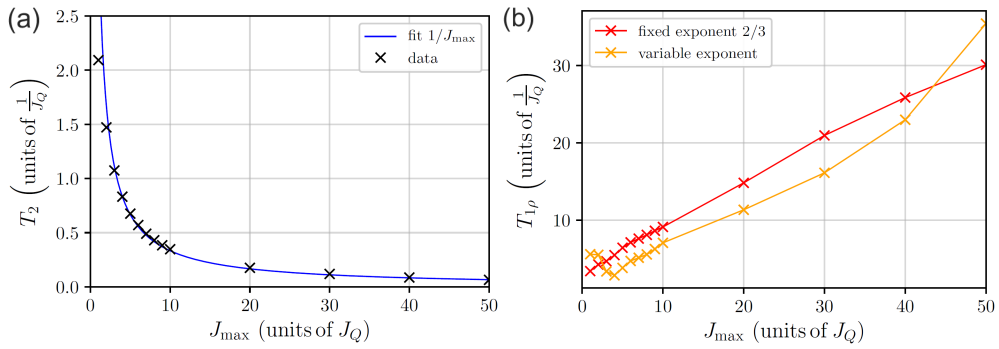


Figure 4.1: Dynamic mean field results in the doubly rotating frame with 4 directly simulated spins. (a) Plot of relaxation timescale T_2 of transverse spin autocorrelation versus the maximum dipolar interaction strength of the central spin with another spin J_{max}. A linear relationship between J_{max} and $1/T_2$ is extracted. (b) Plot of longitudinal relaxation timescale $T_{1\rho}$ versus maximum dipolar interaction strength J_{max} when decay is fit to a stretched exponential with a floating power as well as a power of 2/3, as predicted from the resonance counting model.

and the positions of the nearby surface spins, we fit the echo and $T_{1\rho}$ data with J_Q as a fit parameter using a central spin plus 3 bath spins and the mean fields from the surface spin bath. The fit to the spin echo data is given in fig. 4.2 (a) and the fit to the spin-lock driving measurement at strong drive is given in fig. 4.2 (b).

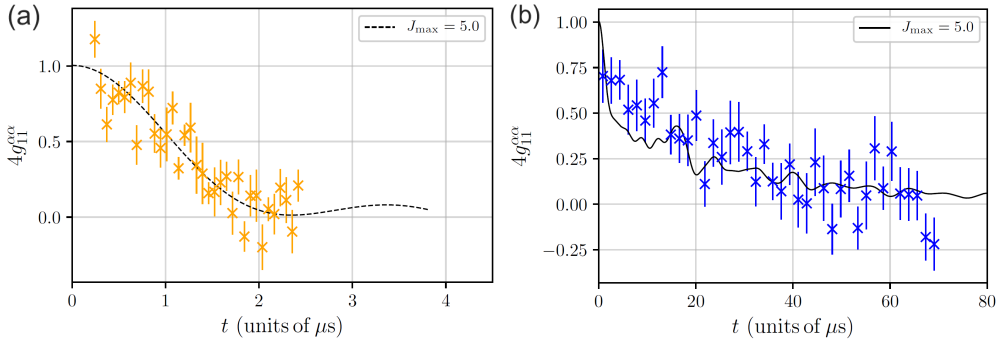


Figure 4.2: Dynamic mean field theory results compared with experimental data. (a) Surface spin echo measurement with dynamic mean field model result (black dashed line). (b) Surface spin $T_{1\rho}$ measurement with dynamic mean field model result (black line).

To summarize, we have shown that dynamic mean field methods can be used in conjunction with direct simulation of a few spins to account for the slow-down in relaxation observed in spin-lock

driving measurements at strong drive. The addition of a few bath spins allows us to include intrinsic system disorder into the simulation.

5

Surface Spin Polarization

In this chapter, we discuss the initial state preparation of the central surface spin by transferring polarization from the NV center to the central surface spin. The basic pulse sequence and idea are shown in fig. 5.1. The NV spin state is first initialized into the $m_s = 0$ state by a green laser pulse (not shown) and then rotated into the transverse plane by applying a $3\pi/2$ pulse. The NV spin and the surface spins are driven at their respective Larmor frequencies by microwave drives of the same Rabi frequency. In the doubly rotating frame with respect to the drive, flip-flop interactions can

occur between the NV spin and the surface spins when they are driven at matching drive strengths. The drive time is determined by the interaction strength between the NV center and the strongest coupled surface spin.

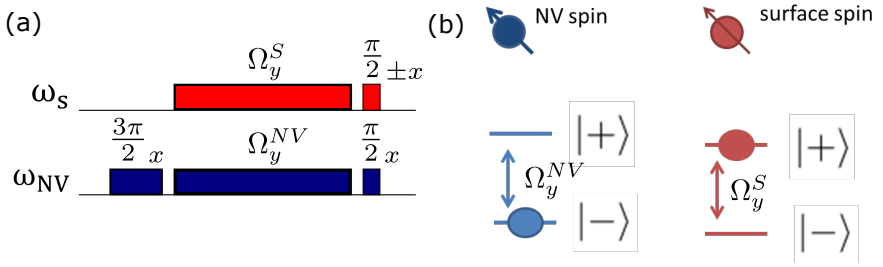


Figure 5.1: (a) RF drives of a Hartmann-Hahn spin polarization pulse sequence. A green laser pulse is applied at the beginning of the sequence to initialize the NV center spin state. (b) Flip-flop interactions between the NV spin and a surface spin in the doubly rotated frame where Ω_y^{NV} and Ω_y^S are the drive Rabi strengths applied to the NV center and surface spins, respectively. The splitting between the eigenstates is given by the strength of the drive in the doubly rotating frame.

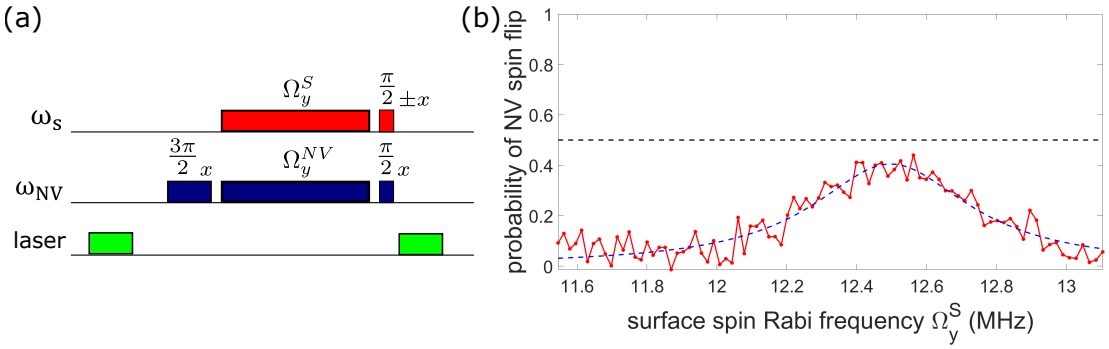


Figure 5.2: (a) Hartmann-Hahn polarization sequence, where final state of the NV center is read out by measuring fluorescence after the polarization transfer. During this sequence, the RF power delivered to the surface spins is swept. (b) Probability of an NV spin flip, where a value of 0.5 would correspond to maximal polarization transfer between the NV center and the central surface spin.

When performing this polarization transfer, it is useful to first measure the NV center depolarization as a function of surface spin drive Rabi Ω^S to ensure proper calibration. Fig. 5.2 shows the calibration of surface spin drive power when the NV drive Rabi frequency is 12.5 MHz. Fig. 5.2 (b) shows the measured probability of an NV spin flip when the surface spin drive power Ω_y^S is swept.

Since the surface spins are initially unpolarized, a probability of 0.5 that the NV spin flips corresponds to maximal polarization transfer from the NV center to the central surface spin.

We can determine if the central surface spin is polarized by directly measuring its state using the NV center after the Hartmann-Hahn polarization transfer. Fig. 5.3 (a) shows a typical pulse sequence where the final state readout of the surface spins by the NV center is done in a way similar to a DEER sequence except either the first or last NV $\pi/2$ pulse is rotated in phase by 90 degrees from the other pulses. For an unpolarized surface spin, the NV center will have an average signal of zero, but for a polarized central surface spin with dipolar coupling k_s to the NV center, the NV center will acquire an average signal proportional to $\sin(k_s t/2)$ where t is the total time duration of the readout and is selected to maximize the signal from the central surface spin.

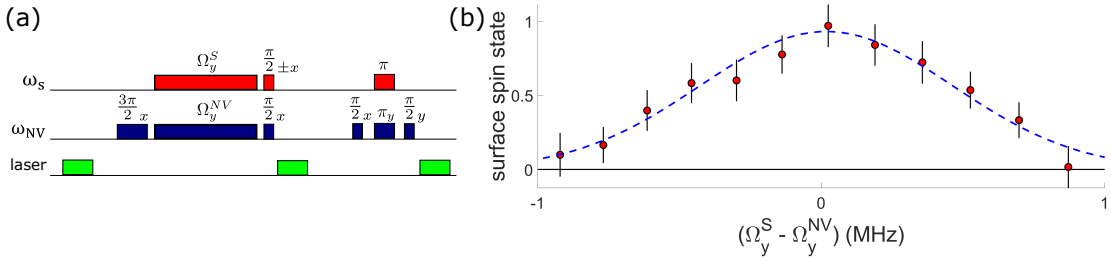


Figure 5.3: (a) Hartmann-Hahn spin polarization and readout pulse sequence, where the surface spin drive power Ω_y^S is swept. (b) Central surface spin polarization as a function of detuning from NV Rabi frequency, normalized between 0 (unpolarized) and 1. A value of 1 corresponds to the maximum polarization expected from the maximal NV depolarization calibrated above.

We confirm that the NV center is measuring a polarized surface spin by controlling the final surface spin state after the Hartmann-Hahn polarization transfer. After the polarization transfer, the surface spin has some polarization along the y-axis. If we do not apply any $\pi/2$ pulse to transfer this polarization to along the longitudinal quantization axis, that polarization will be lost in a time given by the surface spin T_2^*, which is much shorter than the delay before the NV readout pulses. We experimentally verify that when we do not apply a final $\pi/2$ pulse to the surface spins after polarization but instead apply either a π pulse or no pulse, taking the difference, the NV center reads

out no net signal. Fig. 5.3(b) shows the differential signal where the data correspond to the difference in measured signal when a $\pi/2$ or -$\pi/2$ pulse is applied after the Hartmann-Hahn polarization drive to the surface spins. The final surface spin signal is normalized by the correlation spectroscopy contrast.

We can further observe the polarization transfer between the NV center and the strongest coupled surface spin by varying the drive duration and space between readout pulses, fig. 5.4. The maximal polarization transfer occurs at a drive duration and readout spacing consistent with the coupling between the NV center and the strongest coupled surface spin.

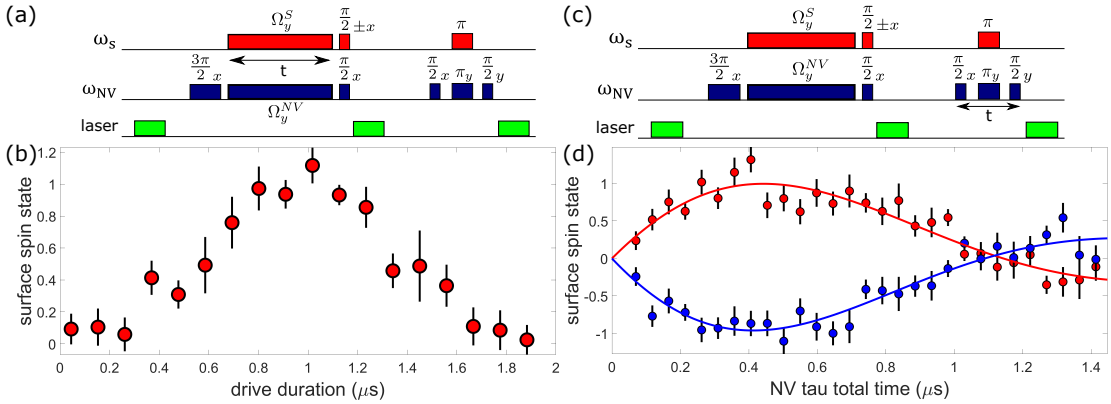


Figure 5.4: (a) Hartmann-Hahn spin polarization and readout pulse sequence where the drive duration is swept. (b) The time to maximum polarization transfer (1 μs) is consistent with the interaction strength between the strongest coupled surface spin and the NV center. (c) Hartmann-Hahn spin polarization and readout pulse sequence with variable time between readout pulses. (d) Time between readout pulses corresponding to maximal polarization transfer consistent with the interaction strength between strongest coupled surface spin and the NV center.

5.1 Dynamics of a Polarized Central Surface Spin

With the ability to transfer polarization from the NV center to one surface spin, we can understand the effect the NV center spin state has on surface spin dynamics. We can achieve this by first polarizing one surface spin and then preparing the NV center in a particular spin state. If the NV center is in the m_s = 0 state, it will have no effect on the surface spins through the dipolar interaction.

However, if the NV center is in either the m_s = 1 or the m_s = -1 state, it will affect the surface spins through the dipolar interaction. We perform a surface spin Ramsey experiment after polarizing one surface spin with the NV in either m_s = 0 or m_s = -1 to observe the effect of the dipolar interaction, fig. 5.5. Note that the drive pulses to the surface spins are detuned, which produce the oscillations.

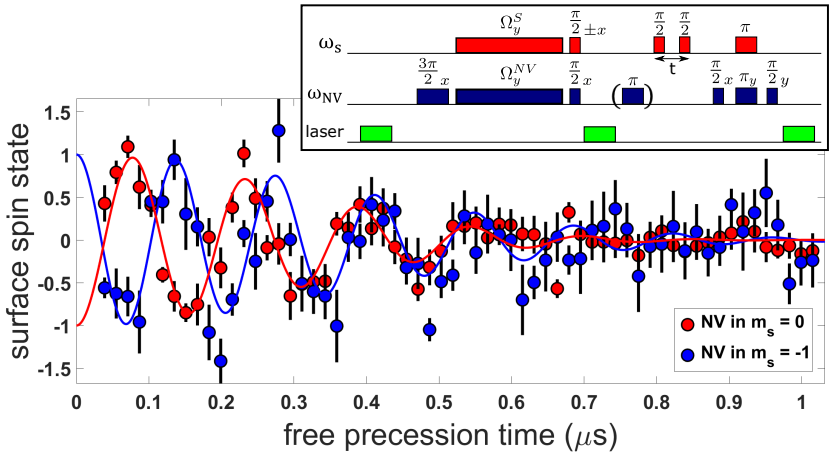


Figure 5.5: Surface spin detuned Ramsey measurement with the NV center in m_s = 0 or m_s = -1. The oscillations are due to detuned surface spin pulses, and we observe a difference in oscillation frequency between the red and blue curves consistent with the dipolar interaction between the NV center and the central surface spin. Inset: pulse sequence with Hartmann-Hahn polarization transfer followed by a surface spin Ramsey sequence and then NV center state readout pulses.

The difference in oscillation frequency is given by the dipolar interaction strength between the NV center and the central surface spin and acts to further detune the surface spins when the NV is in m_s = -1. We can further seek to understand the effect of the NV center spin state on surface spin dynamics by measuring the surface spin T_z of the strongest coupled surface spin after polarization with the NV in either m_s = 0 or m_s = -1, fig. 5.6. The NV center spin state does not affect the surface spin relaxation rate within the experimental uncertainty.

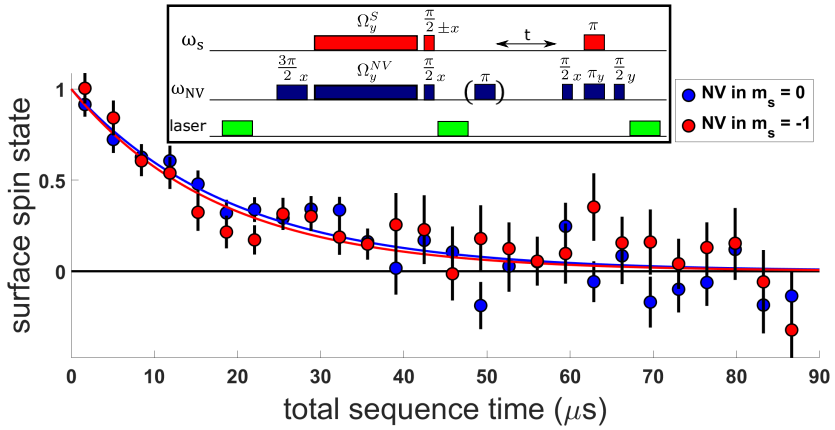


Figure 5.6: Surface spin T_z measurement after polarization with the NV center in either m_s = 0 or m_s = -1. Measurement results indicate no difference in relaxation rate between the two cases, to within measurement uncertainty. Inset: pulse sequence with Hartmann-Hahn spin polarization following by a swept delay time before NV pulses read out the final surface spin state.

5.2 Surface Spin Stability

Recent work has indicated that surface electron spins may not have stable positions but may be mobile on the diamond surface, potentially during the application of green laser light [16]. We directly probe the stability of the strongest coupled surface spin by measuring its state under the application of green laser light. First, we polarize the central surface spin by driving both the surface spins and the NV center at the same drive strength for a time set by the dipolar interaction between the NV center and the central surface spin. We further calibrate the Hartmann-Hahn polarization transfer by observing maximal polarization transfer when the drive strength of the surface spins matches the drive strength of the NV center.

To study the stability of the strongest coupled surface spin, we sweep the duration of the green laser pulse after the polarization transfer, fig. 5.7(a). Note that this central surface spin has a longitudinal correlation time T_z of $\sim 50\,\mu$s. The strongest coupled surface spin is stable under green laser light illumination for at least $50\,\mu$s, fig. 5.7(b).

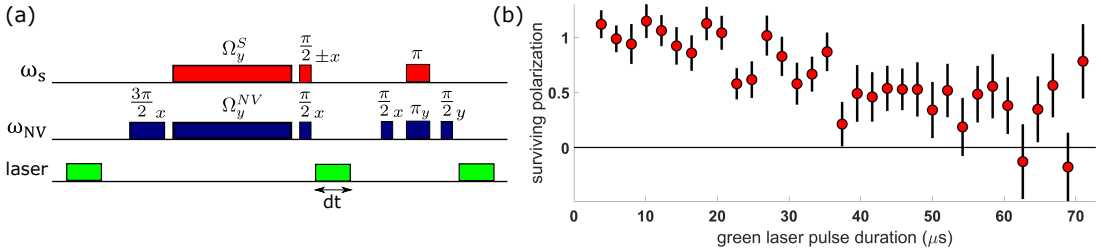


Figure 5.7: Surviving polarization of the central surface spin after green laser light illumination. (a) HH polarization transfer sequence and readout of final NV center state contingent on polarization of central surface spin while green NV repolarization laser pulse duration is swept. (b) Measurement result, normalized by the contrast of the S_z autocorrelation measurement of equivalent initial time delay.

6

Conclusion and Outlook

In chapter 1, we introduced the experimental platform of a single, shallow NV center coupled to a system of electronic spins on the surface of diamond. We measured the dipolar interaction strength between the NV center and the surface spins using the double electron-electron resonance (DEER) sequence and we presented the results of the DEER sequence of one system of strong coupling between the NV center and one central surface spin. We later introduced the correlation spectroscopy pulse sequence where the NV center final state is contingent on the correlated phase accumulation

due to the surface spins. In the limit of a central spin, the sequence reduces to two CNOT gates where the final state of the NV center is contingent on whether the z-projection of the central surface spin state changed between the initial and final pulses.

Using the tools we introduced in chapter 1, we can propose several avenues of exploration. While we measure spin correlations for the strongest coupled surface spin, it may be interesting to attempt to measure spin correlations for the second or third strongest coupled surface spin by adjusting the time between the NV center readout pulses. Also, instead of measuring $\langle S_z(t_0 + t)S_z(t_0)\rangle$, we could apply another CNOT gate and measure other correlation functions such as $\langle S_z(t_0 + t_1 + t_2)S_z(t_0 + t_1)S_z(t_0)\rangle$.

In chapter 2, we employed the tools of correlation spectroscopy to probe the local magnetic environment of the central surface spin. We measured the dipolar interaction strength of the central surface spin with a neighboring surface spin and characterized the magnetic noise power spectrum from nearby proton nuclear spins. For the systems we studied, a surface spin depth of 6Å and an average proton spin separation of 3Å are consistent with our observations. Having quantified the magnitude and sources of decoherence in the system, a next step would be to better engineer pulse sequences to extend the coherence time of the surface spins by properly accounting for the decoherence due to both dipolar interactions as well as the nuclear spin bath noise.

In chapter 3, we studied the relaxation of central spin projection along the direction of the applied magnetic field and modeled the slow relaxation using a dynamic disorder resonance counting model. We found that the rate of relaxation is strongly dependent on the fluctuation timescale of the local disorder. We can suppress this disorder by spin-lock driving and found that at weak drives, the relaxation rate is dependent on the nuclear spin bath noise whereas at strong drive, the relaxation rate is constant for each system considered. The timescale of the relaxation for the spin-lock driving measurements is still an order of magnitude slower than the dipolar interaction timescale, indicating that the intrinsic disorder in the system from the random positions of surface spins plays a major

role in slowing down system dynamics. While the dynamic disorder resonance counting model is consistent with the spin-lock driving data at strong drives, it is not predictive of the relaxation timescale.

In chapter 4, we presented a dynamic mean field theory treatment which is predictive of the relaxation timescales of the transverse and longitudinal spin correlations of a central spin. We were able to extend the model to consider the spin-lock driving measurements taken at strong drive, and we found good agreement between this model plus 3 bath spins and the experimental data.

Finally, in chapter 5, we discussed our ability to polarize the central surface spin using the NV center and Hartmann-Hahn technique. With the central surface spin polarized, we are able to measure effect of the NV center spin state on the central surface spin through the surface spin Ramsey detuning. We also observed that the state of the NV center does not affect the surface spin longitudinal relaxation timescale, possibly due to the fact that the nuclear spin disorder dominates system dynamics in this regime. One further avenue of exploration and technical development would be the polarization of multiple surface spins. This may be useful for explorations of system dynamics of a cooled spin system. The polarization of multiple surface spins may also have applications in the sensing of targets near the diamond surface and could be used to improve the sensitivity.

A

Materials and Setup

A.1 Diamond Sample

Nitrogen implantation was done on a ^{12}C enriched {001} diamond surface at an implantation energy of 3 keV. After annealing, the diamond was cleaned in a 3-acid mixture (equal volumes of concentrated H_2SO_4, HNO_3, and $HClO_4$) for 3 hours. All measurements except NV center depth measurements were performed with the diamond placed in deuterated glycerol (CDN Isotopes D-

0302) and under ambient conditions. NV center depth measurements were performed with the diamond in protonated (undeuterated) glycerol (Sigma-Aldrich G9012).

A.2 Optical Setup

A home built scanning confocal microscope optically addresses and reads out single NV centers. The diamond was placed NV side down on a RF transmission line, and an inverted Nikon CFI Apo TIRF objective (NA = 1.49) was positioned under the stripline. A piezoelectric scanner (Physik Instrumente P-721 PIFOC) was used to control the height of the objective, and a closed-loop scanning galvanometer (Thorlabs GVS012) was used to direct the lateral position of the laser beam focus. Optical excitation was provided by a 532 nm laser (Opto Engine MLL-FN-532-200mW) gated by an acousto-optic modulator (Isomet 1250C) in a double pass configuration. NV center fluorescence passes through a 842 nm short pass filter (Semrock FF01-842/SP-25), a 594 nm long pass filter (Semrock BLP01-594R-25), and a 532 nm notch filter (Semrock NF03-532E-25) before collection by a single-photon counter (Excelitas Technologies SPCM-AQRH-14-FC). The single-photon counter and acousto-optic modulator were gated using TTL pulses produced by a 500 MHz PulseBlasterESR-PRO pulse generator from Spincore Technologies. A typical photon counting rate of 20 kHz was observed, and a photon counter acquisition window of 900 ns was used.

A.3 Radiofrequency Setup

Two Stanford Research SG384 signal generators were used to deliver RF tones to address the NV center and surface spin transitions. IQ modulation was used to control the x and y quadrature amplitude of the signal generator driving the NV center. The output of the signal generator driving the surface spins is fed into a 90 degree phase shifter (RF-Lambda RFHB01G04GVT). The

two outputs of the 90 degree phase shifter were each fed into 180 degree phase shifters (Pulsar Microwave JSO-10-47/3S). Microwave switches (MiniCircuits ZASWA-2-50DR+), controlled by TTL pulses produced by the pulse generator, gated the RF drives. The zero, 90 degree, 180 degree, and 270 degree phase shifted RF pulses that drive the surface spins were combined using a SigaTek SP51400 combiner. The RF signals were power boosted by MiniCircuits amplifiers ZHL-5W-422+, ZHL-30W-252-S+, and ZHL-16W-43-S+, combined using MCLI PS2-134, and fed into a 50Ω-terminated RF transmission line with the diamond sample on top.

B

Nuclear Spin Bath Noise Spectrum

The presence of a 2D layer of proton nuclear spins on the diamond surface will produce a fluctuating magnetic field at the site of the surface spins $B^z(t)$ characterized by a magnetic power spectral density $V(\omega)$ where

$$B^z(t) = B^z_\perp(t) + B^z_\parallel(t). \tag{B.1}$$

We define the z-axis as along the direction of the externally applied magnetic field, which we align along the NV axis. We calculate the projection of the magnetic field due to sum of nuclear spin magnetic moments along the direction of the applied external magnetic field. $B^z_\perp(t)$ is this projection due to components of the nuclear spin magnetic moment perpendicular to the direction of the external magnetic field, which rotate at the nuclear Larmor frequency, and $B^z_\parallel(t)$ is the sum of the contributions from the nuclear spin magnetic moments parallel to the direction of the external magnetic field. From the expression for $B^z(t)$, the noise spectrum $V(\omega)$ will have a low-frequency term due to slow time dependence in $B^z_\parallel(t)$ as well as higher frequency components due to the precession of the transverse magnetic moment, captured by $B^z_\perp(t)$.

We can characterize the low frequency term in $V(\omega)$ following the treatment in [59]. We model the flip-flop relaxation process of the proton nuclear spins as an exponentially correlated Gaussian fluctuating field $B^z_\parallel(t)$ having correlation function $\langle B^z_\parallel(t_0+t)B^z_\parallel(t_0)\rangle = \langle B^2_{\parallel,rms}\rangle \exp(-t/\tau)$ where τ is the longitudinal correlation time of the nuclear spins and $B_{\parallel,rms}$ is the rms value of the magnetic field's longitudinal component projected along the z-axis.

B.1 Wiener-Khinchin Theorem

Using the correlation of the magnetic noise from the fluctuating nuclear spins, we construct the power spectrum for this noise using the Wiener-Khinchin Theorem. The Wiener-Khinchin theorem states that given a random process $x(t)$ with autocorrelation function

$$C(t) = \langle x(t_0+t)x(t_0)\rangle, \tag{B.2}$$

the spectral power density is the Fourier transform of the autocorrelation function

$$V(\omega) = \int_{-\infty}^{\infty} C(t)e^{-i\omega t}dt. \tag{B.3}$$

For our calculations, we use the following definitions of Fourier transform and inverse Fourier transform:

$$X(\omega) = \int_{-\infty}^{\infty} x(t) e^{-i\omega t} dt \tag{B.4}$$

$$x(t) = \frac{1}{2\pi} \int_{-\infty}^{\infty} X(\omega) e^{i\omega t} d\omega \tag{B.5}$$

Using the Wiener-Khinchin theorem with the above definition of Fourier transform, we calculate the spectral power density for the low frequency noise associated with relaxation processes for proton nuclear spins as

$$V_1(\omega) = \int_{-\infty}^{\infty} \langle B_{\parallel,rms}^2 \rangle e^{-|t|/\tau} e^{-i\omega t} dt = 2\langle B_{\parallel,rms}^2 \rangle \frac{\tau}{\omega^2\tau^2 + 1}. \tag{B.6}$$

We apply the same procedure to determine the noise spectrum $V_2(\omega)$ due to proton nuclear spins precessing at their Larmor frequency ω_L. We begin by writing the correlation of the magnetic field noise:

$$\langle B_\perp(t_0 + t) B_\perp(t_0) \rangle = \langle B_{\perp,rms}^2 \rangle e^{j\omega_L t - t/\tau}. \tag{B.7}$$

We then apply the Wiener-Khinchin formula and take the Fourier transform of $\langle B_\perp(t_0+t)B_\perp(t_0)\rangle$ in order to arrive at the power spectral density

$$V_2(\omega) = \int_{-\infty}^{\infty} \langle B_{\perp,rms}^2 \rangle e^{i\omega_L|t| - |t|/\tau} e^{-i\omega t} dt = 2\langle B_{\perp,rms}^2 \rangle \frac{\tau}{(\omega - \omega_L)^2\tau^2 + 1}. \tag{B.8}$$

We combine the contribution of the nuclear spin bath's component at zero frequency and at Larmor frequency to write the final nuclear spin noise power spectrum as

$$V(\omega) = 2\langle B^2_{\parallel,rms}\rangle \frac{\tau}{\omega^2\tau^2+1} + 2\langle B^2_{\perp,rms}\rangle \frac{\tau}{(\omega-\omega_L)^2\tau^2+1}. \tag{B.9}$$

$\langle B^2_{\parallel,rms}\rangle$ and $\langle B^2_{\perp,rms}\rangle$ are geometrically related and we will next derive their relationship. For all following calculations, we use CGS units.

B.2 Calculate $\langle B^2_{\parallel,rms}\rangle$ from Longitudinal Component of the Nuclear Magnetic Moment

We now calculate the magnetic field at the site of surface spins from nuclear spins in the system and follow the treatment presented in [36]. An external field along the NV symmetry axis sets the longitudinal quantization axis $\hat{\mathbf{q}}$. The system is comprised of shallow electronic spins near the surface of diamond with proton nuclear spins on the diamond surface. All nuclear spins are unpolarized and produce a fluctuating magnetic field at the site of each surface spin, and we are interested in calculating the RMS amplitude of the component of this magnetic field along the quantization axis $\hat{\mathbf{q}}$ of the surface spins. We begin by considering the longitudinal component of the magnetic moment of nuclear spins. The component of magnetic field along $\hat{\mathbf{q}}$ from a single nuclear spin parallel or anti-parallel to $\hat{\mathbf{q}}$ is

$$B_q(\mathbf{r}) = \hat{\mathbf{q}}\cdot\mathbf{B} = \hat{\mathbf{q}}\cdot\frac{3\hat{\mathbf{r}}(\vec{m}_n\cdot\hat{\mathbf{r}})-\vec{m}_n}{r^3} = m_n[\frac{3(\hat{\mathbf{r}}\cdot\hat{\mathbf{q}})^2-1}{r^3}] \tag{B.10}$$

where $\mathbf{r}$ is the vector from the nuclear spin to the surface electron spin and m_n is the magnetic moment of the nuclear spin. The mean square field from a collection of spins is

$$B^2_{\parallel,rms} = \langle[\sum_i B_q(\mathbf{r}_i)]^2\rangle. \tag{B.11}$$

By expanding the sum, we get

$$B^2_{\parallel,rms} = \langle \sum_{i \neq j} B_q(\mathbf{r}_i) B_q(\mathbf{r}_j) + \sum_i B^2_q(\mathbf{r}_i) \rangle. \tag{B.12}$$

Since the nuclear spins are random and uncorrelated, this reduces to

$$B^2_{\parallel,rms} = \sum_i B^2_q(\mathbf{r}_i). \tag{B.13}$$

We can convert the sum to an integral by including the nuclear spin density ρ_n:

$$B^2_{\parallel,rms} = \rho_n \int_V [B_q(\mathbf{r})]^2 dV. \tag{B.14}$$

We can define $\hat{\mathbf{q}}$ as the unit vector along the $[1,1,1]$ axis and define $\hat{\mathbf{r}}$ in terms of its spherical coordinates:

$$\hat{\mathbf{q}} = [1,1,1]/\sqrt{3} \tag{B.15}$$

$$\hat{\mathbf{r}} = [\sin(\theta)\cos(\varphi), \sin(\theta)\sin(\varphi), \cos(\theta)] \tag{B.16}$$

where θ is the polar angle measured from the normal of the diamond surface, and φ is the azimuthal angle.

When the diamond is immersed in deutarated glycerol, the simplest assumption to make is that the proton nuclear spins from the diamond lattice termination form a 2D layer at the diamond surface [56,34,13]. Thus, for the case of surface spins which reside a depth d below the 2D layer of proton nuclear spins, we can relate the distance from the surface spins to a nuclear spin plane through the depth d and polar angle θ

$$\cos\theta = \frac{d}{r} \tag{B.17}$$

$$\sin\theta = \sqrt{1 - \frac{d^2}{r^2}} \tag{B.18}$$

The rms magnetic field can be calculated using

$$B^2_{\parallel,rms} = m_n^2 \rho_n \int_0^{2\pi} \int_d^{\infty} [\frac{(\sqrt{1 - \frac{d^2}{r^2}} \cos\varphi + \sqrt{1 - \frac{d^2}{r^2}} \sin\varphi + d/r)^2 - 1}{r^3}]^2 r dr d\varphi \tag{B.19}$$

$$B^2_{\parallel,rms} = m_n^2 \rho_n \frac{3\pi}{8d^4} \tag{B.20}$$

However, one must be careful when calculating the magnetic moment. The magnetic moment is defined as

$$\vec{m} = g\mu_N \vec{S} \tag{B.21}$$

where g is the effective g-factor and μ_N is the nuclear magneton. We can define

$$\langle m \rangle = g\mu_N \langle S \rangle \tag{B.22}$$

$$m = g\mu_N \sqrt{S(S+1)} = \gamma_N \hbar \sqrt{S(S+1)} \tag{B.23}$$

where γ_N is the nuclear spin gyromagnetic ratio.

For proton nuclear spins in the 2D plane of the diamod surface, the rms magnetic field on the surface spin z-axis from the longitudinal component of the magnetic field is given by

$$B^2_{\parallel,rms} = \frac{3\pi}{8d^4}\rho_n(\gamma_N\hbar\sqrt{S(S+1)})^2 \tag{B.24}$$

for surface spins with depth d below the proton layer.

When we perform depth measurements, we place the diamond in undeuterated glycerol. For proton nuclear spins in the half space above the diamond surface, we can calculate the RMS magnetic field from the component of the magnetic moment paralel or antiparallel to $\hat{\mathbf{q}}$:

$$B^2_{rms} = m_n^2\rho_n\int_0^{\pi/2}\int_{d/\cos\theta}^{\infty}\int_0^{2\pi}[\frac{(\sin\theta\cos\varphi+\sin\theta\sin\varphi+\cos\theta)^2-1}{r^3}]^2 r^2 sin\theta d\varphi dr d\theta \tag{B.25}$$

where d is the depth of the surface spin. Solving this integral yields

$$B^2_{rms} = \frac{\pi m_n^2\rho_n}{8d^3} \tag{B.26}$$

Using the expression for magnetic moment, this becomes

$$B^2_{rms} = \frac{\pi\rho_n}{8d^3}(\gamma_N\hbar\sqrt{S(S+1)})^2 \tag{B.27}$$

B.3 Calculate $\langle B^2_{\perp,rms}\rangle$ from Transverse Component of the Nuclear Magnetic Moment

The magnetic field due to the transverse component of the magnetic moment $m_\perp$ is given by

$$\vec{B} = \frac{3\hat{\mathbf{r}}(\vec{m}_\perp\cdot\hat{\mathbf{r}}-\vec{m}_\perp)}{r^3}. \tag{B.28}$$

The external magnetic field is applied along the (1,1,1) direction of the crystal. We can rewrite the classical magnetic moment as $m(m_x, m_y, m_z)$. We can then write $\vec{m}_\perp$ as

$$\vec{m}_\perp = \vec{m} - \frac{\vec{m} \cdot (1,1,1)}{3}(1,1,1) \tag{B.29}$$

$$= \vec{m} - \frac{m_x + m_y + m_z}{3}(1,1,1) \tag{B.30}$$

$$= m(m_x - \frac{m'}{3}, m_y - \frac{m'}{3}, m_z - \frac{m'}{3}) \tag{B.31}$$

where

$$m' = m_x + m_y + m_z. \tag{B.32}$$

We can define

$$\hat{r} = \frac{(x,y,z)}{r} \tag{B.33}$$

Then,

$$\vec{m_\perp} \cdot \hat{r} = \frac{m}{r}[(m_x - \frac{m'}{3}) \cdot x + (m_y - \frac{m'}{3}) \cdot y + (m_z - \frac{m'}{3}) \cdot z] = \frac{mm''}{r} \tag{B.34}$$

where

$$m'' = [(m_x - \frac{m'}{3}) \cdot x + (m_y - \frac{m'}{3}) \cdot y + (m_z - \frac{m'}{3}) \cdot z] \tag{B.35}$$

$$\begin{aligned}\vec{B} &= \frac{m}{r^3}[\frac{3m''}{r^2}(x,y,z) - (m_x - \frac{m'}{3}, m_y - \frac{m'}{3}, m_z - \frac{m'}{3})] \\ &= \frac{m}{r^3}(\frac{3m''_x}{r^3} - m_x + \frac{m'}{3}, \frac{3m''_u}{r^3} - m_u + \frac{m'}{3}, \frac{3m''_z}{r^3} - m_z + \frac{m'}{3})\end{aligned} \tag{B.36}$$

Now compute the external magnetic field along the direction of the NV quantization axis:

$$\begin{aligned}\vec{B} \cdot \frac{(1,1,1)}{\sqrt{3}} &= \frac{m}{\sqrt{3}r^3}[\frac{3m''(x+y+z)}{r^2} - (m_x + m_y + m_z) + m'] \\ &= \frac{\sqrt{3}m}{r^5}m''(x+y+z)\end{aligned} \tag{B.37}$$

We can calculate the rms magnetic field as the following:

$$(B^{tot})^2 = \sum_{spins} B_0^2 = \int \frac{dV}{V_p} \cdot \langle B_0^2 \rangle_m \tag{B.38}$$

where

$$B_0^2 = \frac{3m^2}{r^{10}}(m'')^2(x+y+z)^2 \tag{B.39}$$

Then,

$$\langle B_0^2 \rangle_m = \frac{3m^2}{r^{10}}(x+y+z)^2 \langle (m'')^2 \rangle_m \tag{B.40}$$

$$\begin{aligned}m'' &= \frac{1}{3}[(2m_x - m_y - m_z)_x + (2m_y - m_x - m_z)_y + (2m_z - m_x - m_y)_z] \\ &= \frac{1}{3}[(2x - y - z)m_x + (2y - x - z)m_y + (2z - x - y)m_z]\end{aligned} \tag{B.41}$$

$$\langle m''^2\rangle = \frac{1}{9}[(2x-y-z)_x^{22}\rangle + (2y-x-z)^2\langle m_y^2\rangle + (2z-x-y)\langle m_z^2\rangle] \tag{B.42}$$

since $\langle m_x m_u\rangle = 0$. Use $\langle m_x^2\rangle = \langle m_y^2\rangle = \langle m_z^2\rangle = \frac{1}{3}$. Then,

$$\langle m''^2\rangle = \frac{1}{27}[(2x-y-z)^2 + (2y-x-z)^2 + (2z-x-y)^2] \tag{B.43}$$

$$= \frac{2}{9}(x^2+y^2+z^2-xy-yz-xz) \tag{B.44}$$

Then,

$$\langle B_0^2\rangle_m = \frac{2}{3}\frac{m_n^2}{r^{10}}(x+y+z)^2(r^2-xy-yz-xz) \tag{B.45}$$

We can calculate the rms magnetic field from the transverse component of the magnetic moment of proton nuclear spins in the half space above the diamond surface:

$$B_{\perp,rms}^2 = \rho\int_{-\infty}^{\infty}dx\int_{-\infty}^{\infty}dy\int_{d}^{\infty}dz\langle B_0^2\rangle_m \tag{B.46}$$

$$= \frac{2m_n^2}{3}\rho\int_{-\infty}^{\infty}dx\int_{-\infty}^{\infty}dy\int_{d}^{\infty}dz\frac{(x+y+z)^2(r^2-xy-yz-xz)}{(x^2+y^2+z^2)^5} \tag{B.47}$$

$$B_{\perp,rms}^2 = \frac{5\pi\rho m_n^2}{72d^3} \tag{B.48}$$

Using the definition of magnetic moment defined above, we have found the rms magnetic field due to the transverse magnetic moment to be

$$B^2_{\perp,rms} = \frac{5\pi\rho}{72d^3}(g\mu_N\sqrt{S(S+1)})^2 \tag{B.49}$$

which agrees with the result in [43].

Using this technique, we can calculate the rms magnetic field from a 2D layer of proton spins on the diamond surface:

$$B^2_{\perp,rms} = \frac{2m_n^2}{3}\rho\int_{-\infty}^{\infty}dx\int_{-\infty}^{\infty}dy\frac{(x+y+d)^2(r^2-xy-ya-xa)}{(x^2+y^2+d^2)^5} \tag{B.50}$$

$$B^2_{\perp,rms} = \frac{5\pi m_n^2\rho}{24d^4} \tag{B.51}$$

Using the definition of magnetic moment defined above, the rms magnetic field from the transverse component of the magnetic moment for a 2d layer of spins is

$$B^2_{\perp,rms} = \frac{5\pi\rho}{24d^4}(g\mu_N\sqrt{S(S+1)})^2 \tag{B.52}$$

We find that the projection of the rms magnetic field from the longitudinal component of the magnetic moment on the surface spin z-axis is $3/\sqrt{5}$ times larger than the projection from the transverse component of the nuclear spin magnetic moment for both nuclear spins in the 2D plane as well as nuclear spins in the half space.

B.4 Noise Spectrum Equation

Using the relationship previously derived between the transverse and longitudinal $\langle B^2_{rms}\rangle$ for the given geometry, we can write the expression for the nuclear spin bath noise spectrum as

$$V(\omega) = 2\langle B^2_{\parallel,rms}\rangle(\frac{\tau}{\omega^2\tau^2+1} + +\frac{5}{9}\frac{\tau}{(\omega-\omega_L)^2\tau^2+1}) \tag{B.53}$$

where

$$B^2_{\parallel,rms} = \frac{3\pi}{8d^4}\rho_n(g\mu_N\sqrt{S(S+1)})^2 \tag{B.54}$$

for a system with proton nuclear spins residing on the 2D surface of the diamond and surface spins a depth d below. We can make one further step and rewrite the power spectral density replacing $\langle B^2_{\parallel,rms}\rangle$ with W^2, which are related by γ_e^2, the electron gyromagnetic ratio. We recover the expression for the nuclear spin bath noise spectrum that we use in the main text:

$$V(\omega) = 2\frac{W^2}{\gamma_e^2}(\frac{\tau}{\omega^2\tau^2+1} + +\frac{5}{9}\frac{\tau}{(\omega-\omega_L)^2\tau^2+1}). \tag{B.55}$$

C

Simulation Procedure

In this appendix, we describe the procedure for simulating the autocorrelation of the central surface spin state after the application of the various pulse sequences described in the main text with dynamical evolution due to the nuclear spin bath as well as dipolar interactions with nearby surface spins. For the steps detailed below, we consider a system of one central surface and 2 nearby surface spins.

The step-by-step simulation procedure is the following:

1. We begin by defining the initial density matrix ρ_i of the three surface spin system we are numerically simulating. For measurements performed at room temperature on unpolarized surface spins, all surface spins have an equal chance of being measured in either spin projection along z, the direction of the externally applied magnetic field. For the central surface spin most strongly coupled to the NV center, we can define two possible initial states corresponding to the two spin projections along z

$$|\psi_1^{i,1}\rangle = \begin{pmatrix} 1 \\ 0 \end{pmatrix} \tag{C.1}$$

$$|\psi_2^{i,1}\rangle = \begin{pmatrix} 0 \\ 1 \end{pmatrix} \tag{C.2}$$

We can then write the two initial density matrices for this first surface spin:

$$\rho_1^{i,1} = \begin{pmatrix} 1 & 0 \\ 0 & 0 \end{pmatrix} \tag{C.3}$$

$$\rho_2^{i,1} = \begin{pmatrix} 0 & 0 \\ 0 & 1 \end{pmatrix} \tag{C.4}$$

We can also write the initial density matrices for the other two surface spins beginning in a mixed state:

$$\rho^{i,2} = \frac{1}{2}\begin{pmatrix} 1 & 0 \\ 0 & 1 \end{pmatrix} \tag{C.5}$$

$$\rho^{i,3} = \frac{1}{2}\begin{pmatrix} 1 & 0 \\ 0 & 1 \end{pmatrix} \tag{C.6}$$

The total two initial density matrices are given by the Kronecker product of the initial density matrices for the first, second, and third surface spin:

$$\rho_1^i = \rho_1^{i,1} \otimes \rho^{i,2} \otimes \rho^{i,3} \tag{C.7}$$

$$\rho_2^i = \rho_2^{i,1} \otimes \rho^{i,2} \otimes \rho^{i,3} \tag{C.8}$$

which results in the following initial density matrices:

$$\rho_1^i = \begin{pmatrix} .25 & 0 & 0 & 0 & 0 & 0 & 0 & 0 \\ 0 & .25 & 0 & 0 & 0 & 0 & 0 & 0 \\ 0 & 0 & .25 & 0 & 0 & 0 & 0 & 0 \\ 0 & 0 & 0 & .25 & 0 & 0 & 0 & 0 \\ 0 & 0 & 0 & 0 & 0 & 0 & 0 & 0 \\ 0 & 0 & 0 & 0 & 0 & 0 & 0 & 0 \\ 0 & 0 & 0 & 0 & 0 & 0 & 0 & 0 \\ 0 & 0 & 0 & 0 & 0 & 0 & 0 & 0 \end{pmatrix} \tag{C.9}$$

$$\rho_2^i = \begin{pmatrix} 0 & 0 & 0 & 0 & 0 & 0 & 0 & 0 \\ 0 & 0 & 0 & 0 & 0 & 0 & 0 & 0 \\ 0 & 0 & 0 & 0 & 0 & 0 & 0 & 0 \\ 0 & 0 & 0 & 0 & 0 & 0 & 0 & 0 \\ 0 & 0 & 0 & 0 & .25 & 0 & 0 & 0 \\ 0 & 0 & 0 & 0 & 0 & .25 & 0 & 0 \\ 0 & 0 & 0 & 0 & 0 & 0 & .25 & 0 \\ 0 & 0 & 0 & 0 & 0 & 0 & 0 & .25 \end{pmatrix} \tag{C.10}$$

2. Next we define our spin operators J_i^α. To do so, we first define our spin operators for a spin-1/2:

$$s_x = \frac{1}{2}\begin{pmatrix} 0 & 1 \\ 1 & 0 \end{pmatrix} \tag{C.11}$$

$$s_y = \frac{1}{2i}\begin{pmatrix} 0 & 1 \\ -1 & 0 \end{pmatrix} \tag{C.12}$$

$$s_z = \frac{1}{2}\begin{pmatrix} 1 & 0 \\ 0 & -1 \end{pmatrix} \tag{C.13}$$

Then we define each individual spin operator J_i^α as the Kronecker product between the spin operator s_α and identity matrices. For example, we can define J_1^x as the following:

$$J_1^x = s_x \otimes 1 \otimes 1 \tag{C.14}$$

We can similarly define J_2^y as the following:

$$J_2^y = 1 \otimes s_y \otimes 1 \tag{C.15}$$

3. Next we encode our Hamiltonian using the spin operators defined above.

4. Next we evolve our system according to the given pulse sequence. We take into account evolution under the full Hamiltonian in between pulses as well as during pulses. When a pulse is being applied, we need to add the drive Hamiltonian to the one defined during the previous step. We define our drive Hamiltonian about the x- and y-axis to be

$$H_{drive,x} = \hbar\Omega \sum_i J_i^x \tag{C.16}$$

$$H_{drive,y} = \hbar\Omega \sum_i J_i^y \tag{C.17}$$

We perform evolution under the Hamiltonian for short (typically 2 ns) time steps, and for each time step, we calculate the unitary evolution operator

$$U(t_1) = e^{-iH(t_1)dt/\hbar} \tag{C.18}$$

Then we calculate the new density matrix at the end of each time step

$$\rho_{i+1} = U\rho_i U^\dagger \tag{C.19}$$

Since there are two initial density matrices, we perform these steps beginning with each initial density matrix until we have run through all of the time steps in our sequence.

5. Once we have evolved over all of the time steps (the sequence duration), we can read out the final spin projection along z of the strongest coupled surface spin to the NV center by taking a trace:

$$\langle I_1^z \rangle = Tr[\rho_f I_1^z] \tag{C.20}$$

We do this for both final density matrices and calculate the final surface spin state by subtracting the two final states, effectively measuring an autocorrelation of central spin state.

6. We repeat steps 3-5 if we want to average over different parameters such as bath surface spin positions or nuclear spin signal. This corresponds to calculating a new Hamiltonian and performing the unitary evolution for the new Hamiltonian and the sequence pulses for each average. The final measured spin projection will then be averaged over many different runs.

We use simulation to calculate the average density of surface spins as well as understand how the surface spin echo signal relates to the strongest dipolar interaction strength.

C.1 Effects of Finite Pulse Duration

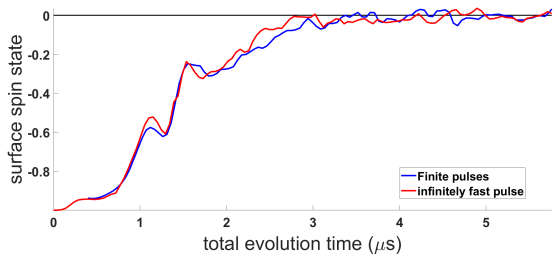


Figure C.1: Simulation results for finite pulses versus infinitely fast pulses. For infinitely fast pulses, the x-axis is given by the total free precession time and for finite pulses, the x-axis corresponds to the free precession time between pulses plus the finite duration of the pulses.

In all measurements, pulses are applied with a 12.5 MHz drive strength, corresponding to a 40 ns π pulse. The total drive duration for the Ramsey (0.04 μs), echo (0.08 μs), and XY-4 (0.2 μs) sequences are significantly shorter than the timescale of the decay, but for the MREV-8 sequence (0.4 μs), we consider the effects of the finite duration of the drive on the decay. We do this by comparing the numeric simulation results of the MREV-8 pulse sequence with a nuclear spin bath for the case of finite pulse duration and infinitely fast pulses. We plot on the x-axis the total evolution time, which includes the evolution time during the pulses for the case of finite pulse duration. We can account for the finite pulse duration by adding the time of the drive to the total free precession time.

D

Decoherence due to the Nuclear Spin Bath

In this appendix, we explore the responses of the Ramsey, echo, XY-4, and MREV-8 pulse sequences to various magnetic field noise spectra. We directly calculate the response and provide comparisons of theory to simulation. For a given pulse sequence, the resulting signal can be written as

$$S(t) = e^{-\chi(t)} \tag{D.1}$$

where

$$\chi(t) = \gamma_e^2 \int \frac{d\omega}{2\pi} \frac{V_B(\omega)}{\omega^2} F(\omega t) \tag{D.2}$$

where $V_B(\omega) = \int dt e^{i\omega t} \langle B(t)B(0)\rangle$ is the classical field spectrum, and $F(\omega t) = \frac{\omega^2}{2}|f(\omega)|^2$ is a filter function with $f(\omega) = \int dt e^{i\omega t} f(t)$.

In this note, we consider a noise spectrum from a classical bath of nuclear spins. Following the treatment in [60], we model the flip-flop relaxation processes of nuclear spins as an exponentially correlated Gaussian fluctuating field $B(t)$ having correlation function $\langle B(t)B(t')\rangle = \langle B^2\rangle \exp(-|t - t'|/\tau)$, where τ is the correlation time of the nuclear spins. We can relate the noise correlation function to a noise power spectrum $V(\omega)$ through $V(\omega) = \int dt e^{i\omega t} \langle B(t)B(0)\rangle$. For our given noise correlation function, we can calculate the resulting power spectral density

$$V_1(\omega) = 2\langle B_1^2\rangle \frac{\tau}{1 + \omega^2\tau^2}. \tag{D.3}$$

In addition to a peak with full width at half maximum $2/t$ centered at zero frequency, we expect the noise spectrum to contain a peak centered at the nuclear spin Larmor frequency ω_L. Due to challenges associated with calculating the signal decay due to a Lorentzian noise spectrum at nonzero frequency, we model this as a harmonic field spectrum with

$$V_2(\omega) = 2\pi\langle B_2^2\rangle \delta(\omega - \omega_L). \tag{D.4}$$

The overall signal of a sequence will be given by its response to $V_B(\omega) = V_1(\omega) + V_2(\omega)$.

D.1 Ramsey

The Ramsey pulse sequence is given by $\frac{\pi}{2} - t - \frac{\pi}{2}$. The filter function of the Ramsey pulse sequence is given by

$$F(\omega t) = 2\sin^2(\omega t/2). \tag{D.5}$$

D.1.1 Response to Lorentzian peak $V_1(\omega)$

The signal decay during a Ramsey sequence is given by $e^{-\chi(t)}$ where

$$\chi(t) = \gamma_e \int \frac{d\omega}{2\pi} \frac{V(\omega)}{\omega^2} F(\omega t) \tag{D.6}$$

and where $F(\omega t)$ is the filter function for the corresponding pulse sequence. We use the spectrum $V_1(\omega)$ with $F(\omega t) = 2\sin^2(\omega t/2)$ to compute the expected signal dephasing.

$$\chi(t) = \gamma_e^2 \int_{-\infty}^{\infty} \frac{d\omega}{2\pi\omega^2} \frac{2\langle B_1^2 \rangle \tau}{1 + \omega^2\tau^2} 2\sin^2(\omega t/2) \tag{D.7}$$

$$\chi(t) = \frac{4\gamma_e^2 \langle B_1^2 \rangle}{\pi\tau} \int_0^{\infty} \frac{d\omega \sin^2(\omega t/2)}{\omega^2(\frac{1}{\tau^2} + \omega^2)} \tag{D.8}$$

We can solve this integral by using the solution

$$\int_0^{\infty} \frac{\sin^2(ax)dx}{x^2(b^2 + x^2)} = \frac{\pi}{4b^2}(2a - \frac{1}{b}(1 - e^{-2ab})) \tag{D.9}$$

for $a > 0$ and $b > 0$. Comparing this integral to the above expression, we find $x = \omega, a = t/2$, and $b = 1/\tau$. We then find

$$\chi(t) = \frac{4\gamma_e^2\langle B_1^2\rangle}{\pi\tau}[\frac{\pi\tau^2}{4}(t - \tau(1 - e^{-t/\tau}))]. \tag{D.10}$$

If we make the assumption that the correlation time of the noise is much longer than the time of a single experiment, we can Taylor expand the exponent.

$$\chi(t) = \gamma_e^2\langle B_1^2\rangle\tau[t - \tau(1 - (1 - \frac{t}{\tau} + \frac{1}{2}\frac{t^2}{\tau^2} - \frac{1}{6}\frac{t^3}{\tau^3}))] \tag{D.11}$$

$$\chi(t) = \gamma_e^2\langle B_1^2\rangle\tau[t - \tau(\frac{t}{\tau} - \frac{1}{2}\frac{t^2}{\tau^2} + \frac{1}{6}\frac{t^3}{\tau^3})] \tag{D.12}$$

$$\chi(t) = \gamma_e^2\langle B_1^2\rangle\tau(\frac{1}{2}\frac{t^2}{\tau} - \frac{1}{6}\frac{t^3}{\tau^2}) \tag{D.13}$$

$$\chi(t) = \gamma^2\langle B_1^2\rangle(\frac{t^2}{2} - \frac{t^3}{6\tau}) \tag{D.14}$$

Using this expression for $\chi(t)$, we find that our Ramsey signal decay is described by

$$S(t) = e^{-(\gamma_e B_1 t/\sqrt{2})^2} e^{(\gamma_e B_1)^2 t^3/(6\tau))} \tag{D.15}$$

which is in agreement with simulation results. Note that the decay is dominated by $\exp(-(\gamma_e B_1 t/\sqrt{2})^2)$.

D.1.2 Response to Harmonic Field Spectrum $V_2(\omega)$

For the noise spectrum $V_2(\omega) = 2\pi\langle B_2^2\rangle\delta(\omega - \omega_L)$, we can calculate $\chi(t)$ as

$$\chi(t) = 2\frac{\gamma_e^2\langle B_2^2\rangle}{\omega_L^2}\sin^2(\omega_L t/2). \tag{D.16}$$

We can verify using simulation that this is correct.

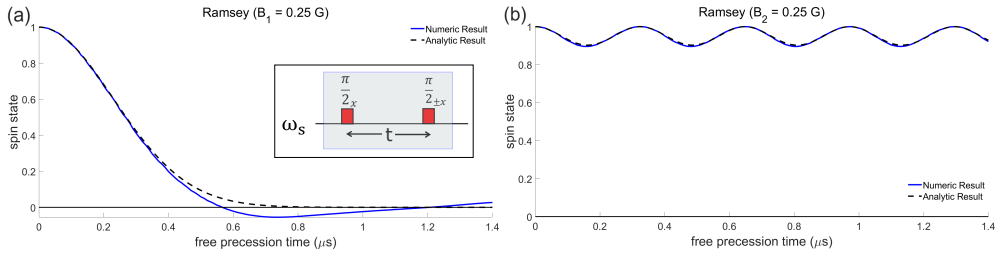


Figure D.1: Numeric verification of expected Ramsey decay. (a) Expected decay from $V_1(\omega)$ with t = 8 μs. Inset: Ramsey pulse sequence. (b) Expected decay from $V_2(\omega)$

D.2 Echo

The echo pulse sequence is given by $\frac{\pi}{2} - \frac{t}{2} - \pi - \frac{t}{2} - \frac{\pi}{2}$ for a total sequence time of t. The filter function of the echo pulse sequence is given by

$$F(\omega t) = 8\sin^4(\omega t/4) \tag{D.17}$$

D.2.1 Response to Lorentzian peak $V_1(\omega)$

The signal decay during an echo sequence is given by $e^{-\chi(t)}$ where

$$\chi(t) = \gamma_e \int \frac{d\omega}{2\pi} \frac{V(\omega)}{\omega^2} F(\omega t) \tag{D.18}$$

and where $F(\omega t)$ is the filter function for the corresponding pulse sequence. We use the spectrum $V_1(\omega)$ with $F(\omega t) = 8\sin^4(\omega t/4) = 8(\sin^2(\omega t/4) - \sin^2(\omega t/2)/4$ to compute the expected signal dephasing.

$$\chi(t) = 8\frac{2\gamma_e^2\langle B_1^2\rangle}{2\pi\tau} \int_{-\infty}^{\infty} \frac{d\omega}{\omega^2} \frac{\sin^2(\omega t/4) - \sin^2(\omega t/2)/4}{\omega^2 + 1/\tau^2} \tag{D.19}$$

We can solve this integral by using the solution

$$\int_0^\infty \frac{\sin^2(ax)dx}{x^2(b^2+x^2)} = \frac{\pi}{4b^2}(2a - \frac{1}{b}(1-e^{-2ab})) \tag{D.20}$$

for $a > 0$ and $b > 0$.

$$\chi(t) = \frac{16\gamma_e^2\langle B_1^2\rangle}{\pi\tau}[\frac{\pi\tau^2}{4}(\frac{t}{2} - \tau(1-e^{-t/(2\tau)})) - \frac{\pi\tau^2}{16}(t - \tau(1-e^{-t/\tau}))] \tag{D.21}$$

$$\chi(t) = 8\gamma_e^2\langle B_1^2\rangle[\frac{\tau}{2}(\frac{t}{2} - \tau(1-(1-\frac{t}{2\tau} + \frac{1}{2}\frac{t^2}{4\tau^2} - \frac{1}{6}\frac{t^3}{8\tau^3}))) - \tag{D.22}$$

$$\frac{\tau}{8}(t - \tau(1-(1-\frac{t}{\tau} + \frac{1}{2}\frac{t^2}{\tau^2} - \frac{1}{6}\frac{t^2}{\tau^2})))] \tag{D.23}$$

$$\chi(t) = 8\gamma_e^2\langle B_1^2\rangle[\frac{\tau}{2}(\frac{t}{2} - \frac{t}{2} + \frac{1}{2}\frac{t^2}{4\tau} - \frac{1}{6}\frac{t^3}{8\tau^2}) - \frac{\tau}{8}(t - t + \frac{1}{2}\frac{t^2}{\tau} - \frac{1}{6}\frac{t^3}{\tau^2})] \tag{D.24}$$

$$\chi(t) = 8\gamma_e^2\langle B_1^2\rangle[\frac{t^2}{16} - \frac{t^3}{96\tau} - \frac{t^2}{16} + \frac{t^3}{48\tau}] \tag{D.25}$$

$$\chi(t) = \frac{\gamma_e^2\langle B_1^2\rangle t^3}{12\tau} \tag{D.26}$$

The expected signal from the spin echo sequence is

$$S(t) = e^{-\frac{\gamma_e^2\langle B_1^2\rangle t^3}{12\tau}}. \tag{D.27}$$

D.2.2 Response to Harmonic Field Spectrum $V_2(\omega)$

For the noise spectrum $V_2(\omega) = 2\pi\langle B_2^2\rangle\delta(\omega - \omega_L)$, we can calculate $\chi(t)$ as

$$\chi(t) = 8\frac{\gamma_e^2\langle B_2^2\rangle}{\omega_L^2}\sin^4(\omega_L t/4). \tag{D.28}$$

We can verify using simulation that this is correct.

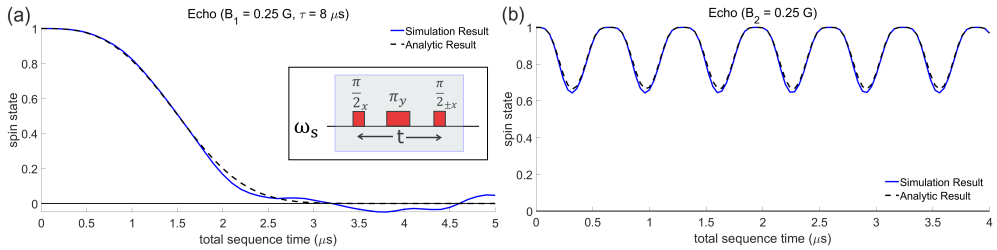


Figure D.2: Numeric verification of expected Hahn echo decay. (a) Expected decay from $V_1(\omega)$ with t = 8 μs. Inset: Hahn echo pulse sequence. (b) Expected decay from $V_2(\omega)$

D.3 XY-4

The XY-4 pulse sequence is given by $\frac{\pi_x}{2} - \frac{t}{8} - \pi_x - \frac{t}{4} - \pi_y - \frac{t}{4} - \pi_x - \frac{t}{4} - \pi_y - \frac{t}{8} - \frac{\pi_x}{2}$ for a total sequence time t. The filter function of the XY-4 pulse sequence is given by

$$F(\omega t) = 128\sin^6(\omega t/16)(\cos(3\omega t/16) + \cos(5\omega t/16))^2. \tag{D.29}$$

D.3.1 Response to Lorentzian peak $V_1(\omega)$

The signal decay during an XY-4 sequence is given by $e^{-\chi(t)}$ where

$$\chi(t) = \gamma_e \int \frac{d\omega}{2\pi} \frac{V(\omega)}{\omega^2} F(\omega t) \tag{D.30}$$

and where $F(\omega t)$ is the filter function for the corresponding pulse sequence. We use the spectrum $V_1(\omega)$ with $F(\omega t) = 128\sin^6(\omega t/16)(\cos(3\omega t/16) + \cos(5\omega t/16))^2 = 8\sin^2(\omega t/16) + 24\sin^2(\omega t/8) - 8\sin^2(3\omega t/16) - 16\sin^2(\omega t/4) + 8\sin^2(5\omega t/16) + 8\sin^2(3\omega t/8) - 8\sin^2(7\omega t/16) + 2\sin^2(\omega t/2)$ to compute the expected signal dephasing.

$$\chi(t) = \frac{2\gamma_e^2\langle B_1^2\rangle}{2\pi\tau} \int_{-\infty}^{\infty} \frac{d\omega}{\omega^2(\omega^2 + 1/\tau^2)} F(\omega t) \tag{D.31}$$

We can solve this integral by using the solution

$$\int_0^\infty \frac{\sin^2(ax)dx}{x^2(b^2+x^2)} = \frac{\pi}{4b^2}(2a - \frac{1}{b}(1-e^{-2ab})) \tag{D.32}$$

for $a > 0$ and $b > 0$.

$$\begin{aligned}\chi(t) = \frac{2\gamma_e^2\langle B_1^2\rangle}{\pi\tau}\frac{\tau^2\pi}{4}[8(\frac{t}{8} - \tau(1-e^{-t/8\tau})) + 24(\frac{t}{4} - \tau(1-e^{-t/4\tau}))\\ -8(\frac{3t}{8} - \tau(1-e^{-3t/8\tau})) - 16(\frac{t}{2} - \tau(1-e^{-t/2\tau})) + 8(\frac{5t}{8} - \tau(1-e^{-5t/8\tau}))\\ +8(\frac{3t}{4} - \tau(1-e^{-3t/4\tau})) - 8(\frac{7t}{8} - \tau(1-e^{-7t/8\tau})) + 2(t - \tau(1-e^{-t/\tau}))]\end{aligned} \tag{D.33}$$

We can further simplify by making the assumption that the correlation time τ is much longer than the sequence time and expand the exponential, retaining terms up to t^3.

$$\begin{aligned}\chi(t) = \frac{\gamma_e^2\langle B_1^2\rangle\tau}{2}[2t + 8\tau(-\frac{t}{8\tau} + \frac{1}{2}(\frac{t}{8\tau})^2 - \frac{1}{6}(\frac{t}{8\tau})^3) + 24\tau(-\frac{t}{4\tau} + \frac{1}{2}(\frac{t}{4\tau})^2 - \frac{1}{6}(\frac{t}{4\tau})^3)\\ -8\tau(-\frac{3t}{8\tau} + \frac{1}{2}(\frac{3t}{8\tau})^2 - \frac{1}{6}(\frac{3t}{8\tau})^3) - 16\tau(-\frac{t}{2\tau} + \frac{1}{2}(\frac{t}{2\tau})^2 - \frac{1}{6}(\frac{t}{2\tau})^3)\\ +8\tau(-\frac{5t}{8\tau} + \frac{1}{2}(\frac{5t}{8\tau})^2 - \frac{1}{6}(\frac{5t}{8\tau})^3) + 8\tau(-\frac{3t}{4\tau} + \frac{1}{2}(\frac{3t}{4\tau})^2 - \frac{1}{6}(\frac{3t}{4\tau})^3)\\ -8\tau(-\frac{7t}{8\tau} + \frac{1}{2}(\frac{7t}{8\tau})^2 - \frac{1}{6}(\frac{7t}{8\tau})^3) + 2\tau(-\frac{t}{\tau} + \frac{1}{2}(\frac{t}{\tau})^2 - \frac{1}{6}(\frac{t}{\tau})^3)\end{aligned} \tag{D.34}$$

Further simplifying, we get

$$\chi(t) = \frac{\gamma_e^2 \langle B_1^2 \rangle \tau}{2} [2t - 2t + \frac{13}{1250} \frac{t^3}{\tau^2}] \tag{D.35}$$

$$\chi(t) = \frac{13 \gamma_e^2 \langle B_1^2 \rangle t^3}{2500\tau} \tag{D.36}$$

D.3.2 Response to Harmonic Field Spectrum $V_2(\omega)$

For the noise spectrum $V_2(\omega) = 2\pi \langle B_2^2 \rangle \delta(\omega - \omega_L)$, we can calculate $\chi(t)$ as

$$\chi(t) = 128 \frac{\gamma_e^2 \langle B_2^2 \rangle}{\omega_L^2} \sin^6(\omega_L t/16)(\cos(3\omega_L t/16) + \cos(5\omega_L t/16))^2. \tag{D.37}$$

We can verify using simulation that this is correct.

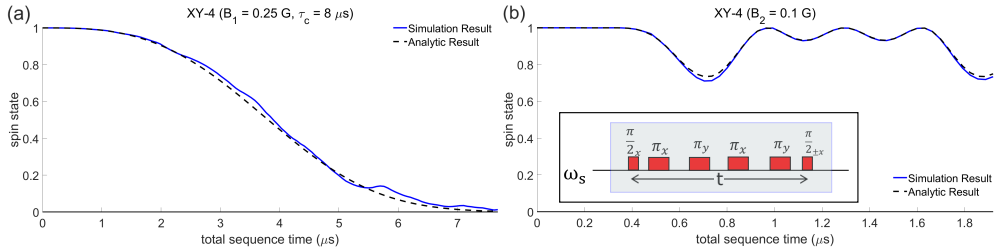


Figure D.3: Numeric verification of expected XY-4 decay. (a) Expected decay from $V_1(\omega)$ with t = 8 μs. (b) Expected decay from $V_2(\omega)$. Inset: XY-4 pulse sequence.

D.4 XY-8

The XY-8 pulse sequence is given by $\frac{\pi_x}{2} - \frac{t}{16} - \pi_x - \frac{t}{8} - \pi_y - \frac{t}{8} - \pi_x - \frac{t}{8} - \pi_y - \frac{t}{8} - \pi_y - \frac{t}{8} - \pi_x - \frac{t}{8} - \pi_y - \frac{t}{8} - \pi_x - \frac{t}{16} - \frac{\pi_x}{2}$ for a total sequence time t. The filter function of the XY-8 pulse sequence is given by

$$F(\omega t) = 128\sin^6(\omega t/32)(\cos(3\omega t/32)+\cos(5\omega t/32)+\cos(11\omega t/32)+\cos(13\omega t/32))^2. \quad \text{(D.38)}$$

D.4.1 Response to Lorentzian peak $V_1(\omega)$

The signal decay during an XY-8 sequence is given by $e^{-\chi(t)}$ where

$$\chi(t) = \gamma_e \int \frac{d\omega}{2\pi} \frac{V(\omega)}{\omega^2} F(\omega t) \quad \text{(D.39)}$$

and where $F(\omega t)$ is the filter function for the corresponding pulse sequence. We use the spectrum $V_1(\omega)$ with $F(\omega t) = 128\sin^6(\omega t/32)(\cos(3\omega t/32) + \cos(5\omega t/32) + \cos(11\omega t/32) + \cos(13\omega t/32))^2 = 8\sin^2(\omega t/32) + 56\sin^2(\omega t/16) - 8\sin^2(3\omega t/32) - 48\sin^2(\omega t/8) + 8\sin^2(5\omega t/32) + 40\sin^2(3\omega t/16) - 8\sin^2(7\omega t/32) - 32\sin^2(\omega t/4) + 8\sin^2(9\omega t/32) + 24\sin^2(5\omega t/16) - 8\sin^2(11\omega t/32) - 16\sin^2(3\omega t/8) + 8\sin^2(13\omega t/32) + 8\sin^2(7\omega t/16) - 8\sin^2(15\omega t/32) + 2\sin^2(\omega t/2)$ to compute the expected signal dephasing.

$$\chi(t) = \frac{2\gamma_e^2\langle B_1^2\rangle}{2\pi\tau} \int_{-\infty}^{\infty} \frac{d\omega}{\omega^2(\omega^2 + 1/\tau^2)} F(\omega t) \quad \text{(D.40)}$$

We can solve this integral by using the solution

$$\int_0^{\infty} \frac{\sin^2(ax)dx}{x^2(b^2+x^2)} = \frac{\pi}{4b^2}(2a - \frac{1}{b}(1 - e^{-2ab})) \quad \text{(D.41)}$$

for $a > 0$ and $b > 0$. I will spare the details of the calculation, but the final result is

$$\chi(t) = \frac{\gamma_e^2\langle B_1^2\rangle t^3}{768\tau} \quad \text{(D.42)}$$

D.4.2 Response to Harmonic Field Spectrum $V_2(\omega)$

For the noise spectrum $V_2(\omega) = 2\pi\langle B_2^2\rangle\delta(\omega - \omega_L)$, we can calculate $\chi(t)$ as

$$\chi(t) = 128\frac{\gamma_e^2\langle B_2^2\rangle}{\omega_L^2}\sin^6(\omega_L t/32)(\cos(3\omega_L t/32) + \cos(5\omega_L t/32) + \cos(11\omega_L t/32) + \cos(13\omega_L t/32))^2. \tag{D.43}$$

We can verify using simulation that this is correct.

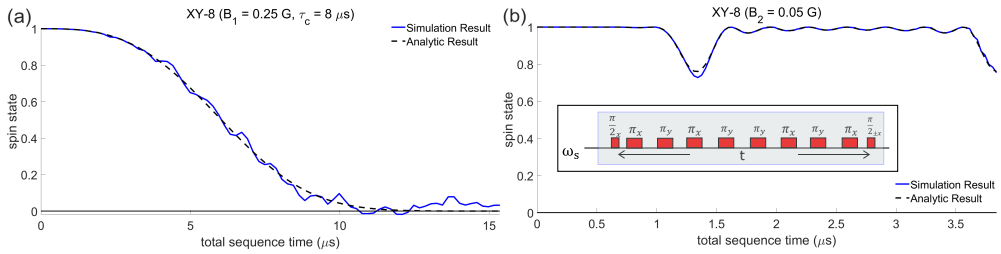


Figure D.4: Numeric verification of expected XY-8 decay. (a) Expected decay from $V_1(\omega)$ with t = 8 μs. (b) Expected decay from $V_2(\omega)$. Inset: XY-8 pulse sequence.

D.5 MREV-8

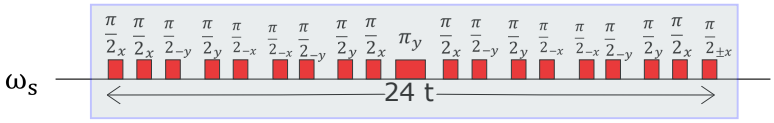


Figure D.5: MREV-8 pulse sequence, applied during the free precession intervals of a spin echo sequence.

We include a picture above of the MREV-8 in echo pulse sequence. Unlike the previous pulse sequences, the time t is now the spacing between the closest pulses (the interpulse spacing is either t

or $2t$). The total sequence time is $24t$. The filter function of the MREV-8 in echo pulse sequence is given by

$$F(\omega t) = 16(1+2\cos(2\omega t))^2(\sin(2\omega t)-\sin(4\omega t)^4(3-4\cos(\omega t)+3\cos(2\omega t)-2\cos(3\omega t)+\cos(4\omega t)) \tag{D.44}$$

D.5.1 Response to Lorentzian peak $V_1(\omega)$

The signal decay during an MREV-8 in echo sequence is given by $e^{-\chi(t)}$ where

$$\chi(t) = \gamma_e \int \frac{d\omega}{2\pi} \frac{V(\omega)}{\omega^2} F(\omega t) \tag{D.45}$$

and where $F(\omega t)$ is the filter function for the corresponding pulse sequence. We use the spectrum $V_1(\omega)$ with $F(\omega t) = 16(1 + 2\cos(2\omega t))^2(\sin(2\omega t) - \sin(4\omega t)^4(3 - 4\cos(\omega t) + 3\cos(2\omega t) - 2\cos(3\omega t) + \cos(4\omega t)) = 12\sin^2(\omega t/2) + 10\sin^2(\omega t) + 10\sin^2(2\omega t) - 12\sin^2(5\omega t/2) - 8\sin^2(3\omega t) + 12\sin^2(7\omega t/2) - 2\sin^2(4\omega t) - 2\sin^2(5\omega t) - 12\sin^2(11\omega t/2) + 24\sin^2(6\omega t) - 4\sin^2(13\omega t/2) - 6\sin^2(7\omega t) - 6\sin^2(8\omega t) + 4\sin^2(17\omega t/2) + 8\sin^2(9\omega t) - 4\sin^2(19\omega t/2) - 2\sin^2(10\omega t) - 2\sin^2(11\omega t) + 4\sin^2(23\omega t/2) - 2\sin^2(12\omega t)$ to compute the expected signal dephasing.

$$\chi(t) = \frac{2\gamma_e^2\langle B_1^2\rangle}{2\pi\tau} \int_{-\infty}^{\infty} \frac{d\omega}{\omega^2(\omega^2 + 1/\tau^2)} F(\omega t) \tag{D.46}$$

We can solve this integral by using the solution

$$\int_0^{\infty} \frac{\sin^2(ax)dx}{x^2(b^2 + x^2)} = \frac{\pi}{4b^2}(2a - \frac{1}{b}(1 - e^{-2ab})) \tag{D.47}$$

for $a > 0$ and $b > 0$. It would be tedious to write all of this out, but we followed the same procedure as before, expanding the exponential and collecting terms. The result is

$$\chi(t) = \frac{261.33\gamma_e^2\langle B_1^2\rangle t^3}{\tau} \tag{D.48}$$

D.5.2 Response to Harmonic Field Spectrum $V_2(\omega)$

For the noise spectrum $V_2(\omega) = 2\pi\langle B_2^2\rangle\delta(\omega - \omega_L)$, we can calculate $\chi(t)$ as

$$\begin{aligned}\chi(t) = 16\frac{\gamma_e^2\langle B_2^2\rangle}{\omega_L^2}(1 + 2\cos(2\omega_L t))^2(\sin(2\omega_L t) - \sin(4\omega_L t)^4(3 - 4\cos(\omega_L t) \\ +3\cos(2\omega_L t) - 2\cos(3\omega_L t) + \cos(4\omega_L t)).\end{aligned} \tag{D.49}$$

We can verify using simulation that this is correct.

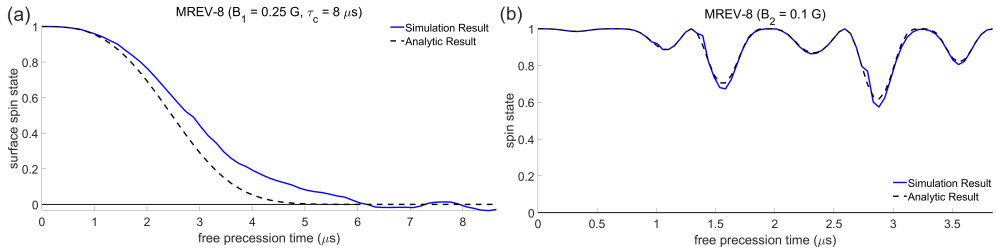


Figure D.6: Numeric verification of expected MREV-8 decay. (a) Expected decay from $V_1(\omega)$ with t = 8 μs. (b) Expected decay from $V_2(\omega)$.

D.6 Final Fit functions

In this section we will list the fit functions for the main pulse sequences that are performed in Chapter 1. t is the total sequence time. The Ramsey sequence can be fit by

$$S_{Ramsey}(t) = \cos(\delta t) e^{-(t/T_{int})^2} e^{-(\gamma_e B_1 t/\sqrt{2})^2} e^{(\gamma_e B_1)^2 t^3/(6\tau))} e^{-2\frac{\gamma_e^2 \langle B_2^2 \rangle}{\omega_L^2} \sin^2(\omega_L t/2)} \tag{D.50}$$

where δ is the frequency of the drive detuning. The spin echo sequence is fit by

$$S_{echo}(t) = e^{-(t/T_2)^2} e^{-\frac{\gamma_e^2 \langle B_1^2 \rangle t^3}{12\tau}} e^{-8\frac{\gamma_e^2 \langle B_2^2 \rangle}{\omega_L^2} \sin^4(\omega_L t/4)}. \tag{D.51}$$

The XY-4 sequence is fit with

$$S_{XY-4}(t) = e^{-(t/T_2)^2} e^{-\frac{13\gamma_e^2 \langle B_1^2 \rangle t^3}{2500\tau}} e^{-128\frac{\gamma_e^2 \langle B_2^2 \rangle}{\omega_L^2} \sin^6(\omega_L t/16)(\cos(3\omega_L t/16)+\cos(5\omega_L t/16))^2}. \tag{D.52}$$

The MREV-8 in echo sequence is fit with

$$S_{MREV-8echo}(t) = e^{-\frac{49\gamma_e^2 \langle B_1^2 \rangle t^3}{2592\tau}} \times$$
$$e^{-16\frac{\gamma_e^2 \langle B_2^2 \rangle}{\omega_L^2}(1+2\cos(\omega_L t/12))^2(\sin(\omega_L t/12)-\sin(\omega_L t/6)^4(3-4\cos(\omega_L t/24)+3\cos(\omega_L t/12)-2\cos(\omega_L t/8)+\cos(\omega_L t/6))} \tag{D.53}$$

References

[1] Abragam, A. (1961). *The principles of nuclear magnetism*.

[2] Álvarez, G. A., Suter, D., & Kaiser, R. (2015). Localization-delocalization transition in the dynamics of dipolar-coupled nuclear spins. *Science*, 349(6250).

[3] Anderson, P. W. (1958). Absence of Diffusion in Certain Random Lattices. *Physical Review*, 109(5), 1492–1505.

[4] Barends, R., Kelly, J., Megrant, A., Veitia, A., Sank, D., Jeffrey, E., White, T. C., Mutus, J., Fowler, A. G., Campbell, B., Chen, Y., Chen, Z., Chiaro, B., Dunsworth, A., Neill, C., O'Malley, P., Roushan, P., Vainsencher, A., Wenner, J., Korotkov, A. N., Cleland, A. N., & Martinis, J. M. (2014). Superconducting quantum circuits at the surface code threshold for fault tolerance. *Nature 2014 508:7497*, 508(7497), 500–503.

[5] Blatt, R. & Roos, C. F. (2012). Quantum simulations with trapped ions. *Nature Physics 2012 8:4*, 8(4), 277–284.

[6] Bloch, I., Dalibard, J., & Zwerger, W. (2008). Many-body physics with ultracold gases. *Reviews of Modern Physics*, 80(3), 885.

[7] Bluvstein, D., Omran, A., Levine, H., Keesling, A., Semeghini, G., Ebadi, S., Wang, T. T., Michailidis, A. A., Maskara, N., Ho, W. W., Choi, S., Serbyn, M., Greiner, M., Vuletić, V., & Lukin, M. D. (2021). Controlling quantum many-body dynamics in driven Rydberg atom arrays. *Science*, 371(6536), 1355–1359.

[8] Bluvstein, D., Zhang, Z., McLellan, C. A., Williams, N. R., & Jayich, A. C. (2019). Extending the Quantum Coherence of a Near-Surface Qubit by Coherently Driving the Paramagnetic Surface Environment. *Physical Review Letters*, 123(14), 146804.

[9] Burin, A. L. (2006). Energy delocalization in strongly disordered systems induced by the long-range many-body interaction.

[10] Choi, J., Choi, S., Kucsko, G., Maurer, P. C., Shields, B. J., Sumiya, H., Onoda, S., Isoya, J., Demler, E., Jelezko, F., Yao, N. Y., & Lukin, M. D. (2017). state spin ensemble (a) (b). vi, 1–11.

[11] Choi, S. (2016). Dynamics in Anderson Critical Systems. (i), 1–5.

[12] Davis, E. J., Ye, B., Machado, F., Meynell, S. A., Mittiga, T., Schenken, W., Joos, M., Kobrin, B., Lyu, Y., Bluvstein, D., Choi, S., Zu, C., Jayich, A. C. B., & Yao, N. Y. (2021). Probing many-body noise in a strongly interacting two-dimensional dipolar spin system.

[13] DeVience, S. J., Pham, L. M., Lovchinsky, I., Sushkov, A. O., Bar-Gill, N., Belthangady, C., Casola, F., Corbett, M., Zhang, H., Lukin, M., Park, H., Yacoby, A., & Walsworth, R. L. (2015). Nanoscale NMR spectroscopy and imaging of multiple nuclear species. *Nature Nanotechnology*, 10(2), 129–134.

[14] Dobrovitski, V. V., Feiguin, A. E., Awschalom, D. D., & Hanson, R. (2008). Decoherence dynamics of a single spin versus spin ensemble. *Physical Review B - Condensed Matter and Materials Physics*, 77(24), 245212.

[15] Doherty, M. W., Manson, N. B., Delaney, P., Jelezko, F., Wrachtrup, J., & Hollenberg, L. C. L. (2013). The nitrogen-vacancy colour centre in diamond. *Physics Reports*, 528(1), 1–45.

[16] Dwyer, B. L., Rodgers, L. V. H., Urbach, E. K., Bluvstein, D., Sangtawesin, S., Zhou, H., Nassab, Y., Fitzpatrick, M., Yuan, Z., De Greve, K., Peterson, E. L., Chou, J.-P., Gali, A., Dobrovitski, V. V., Lukin, M. D., & de Leon, N. P. (2021). Probing spin dynamics on diamond surfaces using a single quantum sensor.

[17] Ebadi, S., Wang, T. T., Levine, H., Keesling, A., Semeghini, G., Omran, A., Bluvstein, D., Samajdar, R., Pichler, H., Ho, W. W., Choi, S., Sachdev, S., Greiner, M., Vuletić, V., & Lukin, M. D. (2021). Quantum phases of matter on a 256-atom programmable quantum simulator. *Nature 2021 595:7866*, 595(7866), 227–232.

[18] Fávaro de Oliveira, F., Antonov, D., Wang, Y., Neumann, P., Momenzadeh, S. A., Häußermann, T., Pasquarelli, A., Denisenko, A., & Wrachtrup, J. (2017). Tailoring spin defects in diamond by lattice charging. *Nature Communications*, 8, 15409.

[19] Fel'dman, E. B. & Lacelle, S. (1996). Cite as. *J. Chem. Phys*, 104, 2000.

[20] Gong, Z.-X., Foss-Feig, M., Brandão, F. G. S. L., & Gorshkov, A. V. (2017). Entanglement Area Laws for Long-Range Interacting Systems. *Physical Review Letters*, 119(5), 50501.

[21] Gopalakrishnan, S., Agarwal, K., Demler, E. A., Huse, D. A., & Knap, M. (2016). Griffiths effects and slow dynamics in nearly many-body localized systems. *Physical Review B*, 93(13), 1–12.

[22] Gräßer, T., Bleicker, P., Hering, D.-B., Yarmohammadi, M., & Uhrig, G. S. (2021). Dynamic mean-field theory for dense spin systems at infinite temperature.

[23] Grinolds, M. S., Warner, M., De Greve, K., Dovzhenko, Y., Thiel, L., Walsworth, R. L., Hong, S., Maletinsky, P., & Yacoby, A. (2014). Subnanometre resolution in three-dimensional magnetic resonance imaging of individual dark spins. *Nature Nanotechnology*, 9(4), 279–284.

[24] Grotz, B., Beck, J., Neumann, P., Naydenov, B., Reuter, R., Reinhard, F., Jelezko, F., Wrachtrup, J., Schweinfurth, D., Sarkar, B., & Hemmer, P. (2011). Sensing external spins with nitrogen-vacancy diamond. *New Journal of Physics*, 13(5), 55004.

[25] Jurcevic, P., Lanyon, B. P., Hauke, P., Hempel, C., Zoller, P., Blatt, R., & Roos, C. F. (2014). Quasiparticle engineering and entanglement propagation in a quantum many-body system. *Nature*, 511(7508), 202–205.

[26] Kao, W., Li, K. Y., Lin, K. Y., Gopalakrishnan, S., & Lev, B. L. (2021). Topological pumping of a 1D dipolar gas into strongly correlated prethermal states. *Science*, 371(6526), 296–300.

[27] Kaufman, A. M., Tai, M. E., Lukin, A., Rispoli, M., Schittko, R., Preiss, P. M., & Greiner, M. (2016). Quantum thermalization through entanglement in an isolated many-body system. *Science*, 353(6301), 794–800.

[28] Keesling, A., Omran, A., Levine, H., Bernien, H., Pichler, H., Choi, S., Samajdar, R., Schwartz, S., Silvi, P., Sachdev, S., Zoller, P., Endres, M., Greiner, M., Vuletić, V., & Lukin, M. D. (2019). Quantum Kibble–Zurek mechanism and critical dynamics on a programmable Rydberg simulator. *Nature 2019 568:7751*, 568(7751), 207–211.

[29] Koch, J., Yu, T. M., Gambetta, J., Houck, A. A., Schuster, D. I., Majer, J., Blais, A., Devoret, M. H., Girvin, S. M., & Schoelkopf, R. J. (2007). Charge-insensitive qubit design derived from the Cooper pair box. *Physical Review A*, 76(4), 042319.

[30] Kucsko, G., Choi, S., Choi, J., Maurer, P. C., Zhou, H., Landig, R., Sumiya, H., Onoda, S., Isoya, J., Jelezko, F., Demler, E., Yao, N. Y., & Lukin, M. D. (2018). Critical Thermalization of a Disordered Dipolar Spin System in Diamond. *Physical Review Letters*, 121(2), 23601.

[31] Kyprianidis, A., Machado, F., Morong, W., Becker, P., Collins, K. S., Else, D. V., Feng, L., Hess, P. W., Nayak, C., Pagano, G., Yao, N. Y., & Monroe, C. (2021). Observation of a prethermal discrete time crystal. *Science*, 372(6547), 1192–1196.

[32] Ladd, T. D., Jelezko, F., Laflamme, R., Nakamura, Y., Monroe, C., & O'Brien, J. L. (2010). Quantum computers. *Nature*, 464(7285), 45–53.

[33] Laraoui, A., Dolde, F., Burk, C., Reinhard, F., Wrachtrup, J., & Meriles, C. A. (2013). High-resolution correlation spectroscopy of 13C spins near a nitrogen-vacancy centre in diamond. *Nature Communications*, 4(1), 1–7.

[34] Loretz, M., Rosskopf, T., Boss, J. M., Pezzagna, S., Meijer, J., & Degen, C. L. (2014). Single-proton spin detection by diamond magnetometry. *Science*, (pp. science.1259464—-).

[35] Lukin, A., Rispoli, M., Schittko, R., Tai, M. E., Kaufman, A. M., Choi, S., Khemani, V., Léonard, J., & Greiner, M. (2019). Probing entanglement in a many-body-localized system. *Science*, 364(6437), 256–260.

[36] Mamin, H. J., Kim, M., Sherwood, M. H., Rettner, C. T., Ohno, K., Awschalom, D. D., & Rugar, D. (2013). Nanoscale nuclear magnetic resonance with a nitrogen-vacancy spin sensor. *Science*, 339(6119), 557–560.

[37] Morong, W., Liu, F., Becker, P., Collins, K. S., Feng, L., Kyprianidis, A., Pagano, G., You, T., Gorshkov, A. V., & Monroe, C. (2021). Observation of Stark many-body localization without disorder. *Nature* |, 599, 393.

[38] Myers, B. A., Ariyaratne, A., & Jayich, A. B. (2017). Double-Quantum Spin-Relaxation Limits to Coherence of Near-Surface Nitrogen-Vacancy Centers. *Physical Review Letters*, 118(19), 197201.

[39] Myers, B. A., Das, A., Dartiailh, M. C., Ohno, K., Awschalom, D. D., & Bleszynski Jayich, A. C. (2014). Probing Surface Noise with Depth-Calibrated Spins in Diamond. *Physical Review Letters*, 113(2), 27602.

[40] Nielsen, M. A. & Chuang, I. L. (2010). *Quantum computation and quantum information*. Cambridge University Press.

[41] Orioli, A. P., Signoles, A., Wildhagen, H., Günter, G., Berges, J., Whitlock, S., & Weidemüller, M. (2018). Relaxation of an Isolated Dipolar-Interacting Rydberg Quantum Spin System. *Physical Review Letters*, 120(6), 063601.

[42] Parsons, M. F., Mazurenko, A., Chiu, C. S., Ji, G., Greif, D., & Greiner, M. (2016). Site-resolved measurement of the spin-correlation function in the Fermi-Hubbard model. *Science*, 353(6305), 1253–1256.

[43] Pham, L. M., DeVience, S. J., Casola, F., Lovchinsky, I., Sushkov, A. O., Bersin, E., Lee, J., Urbach, E., Cappellaro, P., Park, H., Yacoby, A., Lukin, M., & Walsworth, R. L. (2016). NMR technique for determining the depth of shallow nitrogen-vacancy centers in diamond. *Physical Review B*, 93(4), 45425.

[44] Richerme, P., Gong, Z. X., Lee, A., Senko, C., Smith, J., Foss-Feig, M., Michalakis, S., Gorshkov, A. V., & Monroe, C. (2014). Non-local propagation of correlations in quantum systems with long-range interactions. *Nature*, 511(7508), 198–201.

[45] Rispoli, M., Lukin, A., Schittko, R., Kim, S., Tai, M. E., Léonard, J., & Greiner, M. (2019). Quantum critical behaviour at the many-body localization transition. *Nature 2019 573:7774*, 573(7774), 385–389.

[46] Romach, Y., Müller, C., Unden, T., Rogers, L. J., Isoda, T., Itoh, K. M., Markham, M., Stacey, A., Meijer, J., Pezzagna, S., Naydenov, B., McGuinness, L. P., Bar-Gill, N., & Jelezko, F. (2015). Spectroscopy of Surface-Induced Noise Using Shallow Spins in Diamond. *Physical Review Letters*, 114(1), 17601.

[47] Rosskopf, T., Dussaux, A., Ohashi, K., Loretz, M., Schirhagl, R., Watanabe, H., Shikata, S., Itoh, K. M., & Degen, C. L. (2014). Investigation of Surface Magnetic Noise by Shallow Spins in Diamond. 147602(April), 1–5.

[48] Sangtawesin, S., Dwyer, B. L., Srinivasan, S., Allred, J. J., Rodgers, L. V. H., Greve, K. D., Stacey, A., Dontschuk, N., Donnell, K. M. O., Hu, D., Evans, D. A., Jaye, C., Fischer, D. A., Markham, M. L., Twitchen, D. J., Park, H., Lukin, M. D., Leon, N. P. D., & Surface, O.-t. D. (2019). Origins of Diamond Surface Noise Probed by Correlating Single-Spin Measurements with Surface Spectroscopy. 031052, 1–17.

[49] Schirhagl, R., Chang, K., Loretz, M., & Degen, C. L. (2014). Nitrogen-Vacancy Centers in Diamond: Nanoscale Sensors for Physics and Biology. *Annual Review of Physical Chemistry*, 65(1), 83–105.

[50] Schlipf, L., Oeckinghaus, T., Xu, K., Dasari, D. B. R., Zappe, A., de Oliveira, F. F., Kern, B., Azarkh, M., Drescher, M., Ternes, M., Kern, K., Wrachtrup, J., & Finkler, A. (2017). A molecular quantum spin network controlled by a single qubit. *Science Advances*, 3(8), e1701116.

[51] Schreiber, M., Hodgman, S. S., Bordia, P., Lüschen, H. P., Fischer, M. H., Vosk, R., Altman, E., Schneider, U., & Bloch, I. (2015). Observation of many-body localization of interacting fermions in a quasi-random optical lattice.

[52] Sipahigil, A., Evans, R. E., Sukachev, D. D., Burek, M. J., Borregaard, J., Bhaskar, M. K., Nguyen, C. T., Pacheco, J. L., Atikian, H. A., Meuwly, C., Camacho, R. M., Jelezko, F., Bielejec, E., Park, H., Lončar, M., & Lukin, M. D. (2016). An integrated diamond nanophotonics platform for quantum-optical networks. *Science*, 354(6314), 847–850.

[53] Slichter, C. P. (1978). *Principles of Magnetic Resonance*, volume 1 of *Springer Series in Solid-State Sciences*. Berlin, Heidelberg: Springer Berlin Heidelberg.

[54] Smith, J., Lee, A., Richerme, P., Neyenhuis, B., Hess, P. W., Hauke, P., Heyl, M., Huse, D. A., & Monroe, C. (2016). Many-body localization in a quantum simulator with programmable random disorder. *Nature Physics 2016 12:10*, 12(10), 907–911.

[55] Stacey, A., Dontschuk, N., Chou, J.-P., Broadway, D. A., Schenk, A. K., Sear, M. J., Tetienne, J.-P., Hoffman, A., Prawer, S., Pakes, C. I., Tadich, A., de Leon, N. P., Gali, A., & Hollenberg, L. C. L. (2019). Evidence for Primal sp ² Defects at the Diamond Surface: Candidates for Electron Trapping and Noise Sources. *Advanced Materials Interfaces*, 6(3), 1801449.

[56] Staudacher, T., Raatz, N., Pezzagna, S., Meijer, J., Reinhard, F., Meriles, C. A., & Wrachtrup, J. (2015). Probing molecular dynamics at the nanoscale via an individual paramagnetic centre. *Nature Communications*, 6, 8527.

[57] Sushkov, A. O., Lovchinsky, I., Chisholm, N., Walsworth, R. L., Park, H., & Lukin, M. D. (2014). Magnetic resonance detection of individual proton spins using quantum reporters. *Physical Review Letters*, 113(19), 197601.

[58] Taminiau, T. H., Cramer, J., van der Sar, T., Dobrovitski, V. V., & Hanson, R. (2014). Universal control and error correction in multi-qubit spin registers in diamond. *Nature Nanotechnology 2014 9:3*, 9(3), 171–176.

[59] Taylor, J. M., Cappellaro, P., Childress, L., Jiang, L., Budker, D., Hemmer, P. R., Yacoby, A., Walsworth, R., & Lukin, M. D. (2008a). High-sensitivity diamond magnetometer with nanoscale resolution. *Nature Physics*, 4(10), 810–816.

[60] Taylor, J. M., Cappellaro, P., Childress, L., Jiang, L., Budker, D., Hemmer, P. R., Yacoby, A., Walsworth, R., & Lukin, M. D. (2008b). High-sensitivity diamond magnetometer with nanoscale resolution. 4(October).

[61] Tetienne, J.-P., Hingant, T., Rondin, L., Cavaillès, A., Mayer, L., Dantelle, G., Gacoin, T., Wrachtrup, J., Roch, J.-F., & Jacques, V. (2013). Spin relaxometry of single nitrogen-vacancy defects in diamond nanocrystals for magnetic noise sensing. *Physical Review B*, 87(23), 235436.

[62] Turner, C. J., Michailidis, A. A., Abanin, D. A., Serbyn, M., & Papić, Z. (2018). Weak ergodicity breaking from quantum many-body scars. *Nature Physics 2018 14:7*, 14(7), 745–749.

[63] Wei, K. X., Ramanathan, C., & Cappellaro, P. (2018). Exploring Localization in Nuclear Spin Chains. *Physical Review Letters*, 120(7), 70501.

[64] Yao, N. Y., Laumann, C. R., Gopalakrishnan, S., Knap, M., Müller, M., Demler, E. A., & Lukin, M. D. (2014). Many-body localization in dipolar systems. *Physical Review Letters*, 113(24), 243002.

[65] Zhang, J., Hess, P. W., Kyprianidis, A., Becker, P., Lee, A., Smith, J., Pagano, G., Potirniche, I. D., Potter, A. C., Vishwanath, A., Yao, N. Y., & Monroe, C. (2017). Observation of a Discrete Time Crystal. *Nature*, 543(January), 217.